The Pennsylvania State University

The Graduate School

ANGULAR DISTRIBUTIONS IN RADIATIVE DECAYS OF CHARMONIUM χ_1 AND χ_2 STATES FORMED IN $p\bar{p}$ ANNIHILATIONS

A Thesis in

Physics

by

Anna M. Majewska

Submitted in Partial Fulfillment
of the Requirements
for the Degree of

Doctor of Philosophy

May 1993

Abstract

A study of the angular distributions in the reactions $p\bar{p} \to \chi_{1,2} \to J/\psi\gamma \to e^+e^-\gamma$ is presented, using a sample of 2309 χ_2 events and 360 χ_1 events. The data were collected by Fermilab experiment E-760, which is the first high-statistics experiment studying charmonium states formed directly in $p\bar{p}$ annihilations. From the analysis of the angular distributions it is found that the helicity in the formation process $p\bar{p} \to \chi_2$ is mainly ± 1, and that the radiative decays $\chi_{1,2} \to J/\psi\gamma$ are predominantly dipole transitions. The contribution of helicity zero in the χ_2 formation process is found to be $B_0^2 = 0.01 \pm^{0.11}_{0.12}$. The normalized quadrupole amplitudes in the radiative decays are $a_2(\chi_2) = -0.161 \pm^{0.056}_{0.061}$ and $a_2(\chi_1) = -0.129 \pm 0.059$, and the octupole amplitude in the χ_2 decay is $a_3(\chi_2) = -0.017 \pm^{0.042}_{0.040}$. The results, which represent a significant improvement on the experimental knowledge of the angular distribution parameters, are compared with the measurements from previous experiments, and with theoretical predictions.

Contents

List of Figures

List of Tables

Acknowledgements

First of all, I would like to express my thanks to Professor Gerald A. Smith, for the thoughtful guidance during the course of my graduate study, and especially during the work on this thesis. I am indebted to all the members of the E-760 Collaboration, for contributing to the success of this experiment, and for creating a stimulating and friendly atmosphere. In particular, I would like to thank Ray Lewis, Tom Armstrong, Flavio Marchetto and Rosanna Cester for helpful discussions, advice, and encouragement.

This work was supported in part by the U.S. National Science Foundation.

Introduction

Charmonium, a bound system of a charmed quark and antiquark, has played a key role in understanding strong interactions, similar to the role of the hydrogen atom and positronium in understanding the details of quantum electrodynamics. Charmonium is the lightest quark-antiquark system which can be described by non-relativistic potential models (in the first approximation). It is also the first such system to which QCD can be applied, at least approximately, as a perturbative theory [1, 2].

Since its discovery in 1974, the charmonium system has been extensively studied in experiments, mostly with e^+e^- colliders. A new era in charmonium spectroscopy began recently with experiments which study charmonium states formed in $p\bar{p}$ annihilations. In such experiments one can investigate charmonium states which are difficult or impossible to access in e^+e^- experiments.

Fermilab experiment E-760 is the first high-statistics experiment studying charmonium states formed in $p\bar{p}$ annihilations. In this thesis, I use a large sample of events

$$p\bar{p} \rightarrow \chi_{1,2} \rightarrow J/\psi\,\gamma \rightarrow e^+e^-\,\gamma, \tag{0.1}$$

collected during the 1990-1991 E-760 run, in order to study angular distributions in these reactions. These angular distributions are sensitive to the features of the $p\bar{p}$ annihilation process, the properties of the $c\bar{c}$ bound state, and the nature of its radiative decay. More specifically, the parameters describing the angular distributions can be interpreted in terms of helicity in the formation process, $p\bar{p} \rightarrow \chi_{1,2}$, and multipolarity of the radiative decay, $\chi_{1,2} \rightarrow J/\psi\,\gamma$ [3]. Measurement of the formation helicity can be used as a test of the helicity selection rule of massless QCD [4], and of deviations from this rule due to non-zero quark

masses and non-perturbative QCD effects. Contributions of higher multipoles in the radiative transitions can be compared with theoretical predictions, made in the framework of the potential model of charmonium with relativistic corrections [5]. Previous measurements of the angular distribution parameters suffer from large statistical errors. In addition, there is a significant discrepancy between two previous measurements of the quadrupole amplitude in the χ_2 decay, and one of the measurements implies a large negative value of the anomalous magnetic moment of the charmed quark [6, 7].

This thesis is organized as follows. Chapter 1 gives a brief overview of charmonium physics, including the theoretical description of charmonium, the experimental situation before $p\bar{p}$ charmonium experiments, and a summary of the E-760 physics program. In chapter 2 the theoretical description of angular distributions in the reactions $p\bar{p} \rightarrow \chi_{1,2} \rightarrow J/\psi\gamma \rightarrow e^+e^-\gamma$ is presented. A detailed description of the E-760 experimental setup, including the beam, target, detector, triggers and data acquisition, is given in chapter 3. Chapter 4 explains the data analysis, from kinematic fitting and event selection to the method of determining angular distribution parameters and a study of systematic errors. In chapter 5 the results of the analysis are presented and compared with the results of previous experiments and with theoretical predictions.

Chapter 1

Overview of charmonium physics

In this chapter the discovery of the charmonium system is described, and the theoretical model of charmonium is briefly outlined. The advantages of studying charmonium formed in $p\bar{p}$ annihilations are pointed out, and the results from the first high-statistics $p\bar{p}$ charmonium experiment, E-760 at Fermilab, are summarized. It should be noted that the short overview of charmonium physics presented here is not comprehensive; thorough reviews of the subject can be found in Refs. [1, 2, 8–12].

1.1 Discovery of charmonium

Before 1974, the standard set of fundamental particles consisted of four leptons, e, ν_e, μ and ν_μ, and three quarks, u, d and s. However, there were several theoretical and experimental arguments indicating the need for a fourth quark. The first argument came from the idea of quark-lepton symmetry, which required a fourth quark, given the existence of four leptons [13]. The second argument was based on the experimentally observed suppression of several weak decays, involving strangeness-changing neutral currents, such as $K^+ \to \pi^+ e^+ e^-$ and $K_L^0 \to \mu^+ \mu^-$. The suppression could not be explained within the framework of weak interactions with just three quarks. The problem could be solved by introducing a fourth quark c (*charmed*), and assuming that weak interactions involve four quarks, u, $d' = d\cos\theta_c + s\sin\theta_c$, c, and $s' = s\cos\theta_c - d\sin\theta_c$, where θ_c is the Cabibbo angle [14]. The third argument came from measurements of $R \equiv \sigma(e^+e^- \to hadrons)/\sigma(e^+e^- \to \mu^+\mu^-)$ at center of mass energies in the range from 3 to 4 GeV [15]. The predicted value of is

$R = 3\sum q_i^2$ (to the first order in α_s), where the sum runs over accessible quark flavors, and q_i denotes quark charge. For three quarks $R = 2$, and for four quarks $R = 3.3$; the latter is much closer to the experimental value.

In 1974 a narrow resonance with a mass of $\sim 3.1\,\mathrm{GeV/c^2}$ was discovered simultaneously by two experiments. The first, at SLAC [16], observed the new state as a resonance in the cross section for the reactions $e^+e^- \rightarrow hadrons$, $e^+e^- \rightarrow e^+e^-$, and $e^+e^- \rightarrow \mu^+\mu^-$. The second, at BNL [17], discovered a peak in the e^+e^- invariant mass spectrum in the reaction $p + Be \rightarrow e^+e^- + anything$. Two weeks later, a discovery of another narrow state, with a mass of $\sim 3.7\,\mathrm{GeV/c^2}$, was announced [18].

The two new resonances, called J/ψ and ψ', were quickly interpreted [19–21] as the lowest spin triplet S state and its radial excitation of the bound $c\bar{c}$ system called charmonium (in analogy to positronium), with a c quark mass of $\sim 1.5\,\mathrm{GeV/c^2}$. The narrow widths of the J/ψ and ψ' ($\Gamma_{tot}(J/\psi) = 86 \pm 6\,\mathrm{KeV}$ and $\Gamma_{tot}(\psi') = 278 \pm 32\,\mathrm{KeV}$ [22]) were qualitatively explained by the fact that their masses were too low to allow decays into charmed mesons, consisting of a c quark and a light antiquark. Thus, the only allowed strong decays proceed through diagrams with disconnected quark lines, which are suppressed by the OZI rule [23]. Examples of OZI-suppressed and favored decays are shown in Fig. 1.1.

In the few years following the 1974 discovery, several other charmonium states were found, as products of radiative decays of the ψ'. In 1975 a triplet of states with masses from ~ 3.4 to $\sim 3.55\,\mathrm{GeV/c^2}$ was discovered at SLAC and at DESY [24]. They were named χ_0, χ_1, and χ_2, and interpreted as spin triplet P states. In 1980 a state called η_c at $\sim 3.0\,\mathrm{GeV/c^2}$ was found [25], and assigned as the lowest spin singlet S state. In 1982 a candidate for its radial excitation, η_c', was observed [26]. The existence of all these states was earlier predicted within the framework of the charmonium model [19, 21]. Additional support for the interpretation of the new particles as bound $c\bar{c}$ states came from the discovery of charmed D mesons at $1.87\,\mathrm{GeV/c^2}$ in 1976 [27].

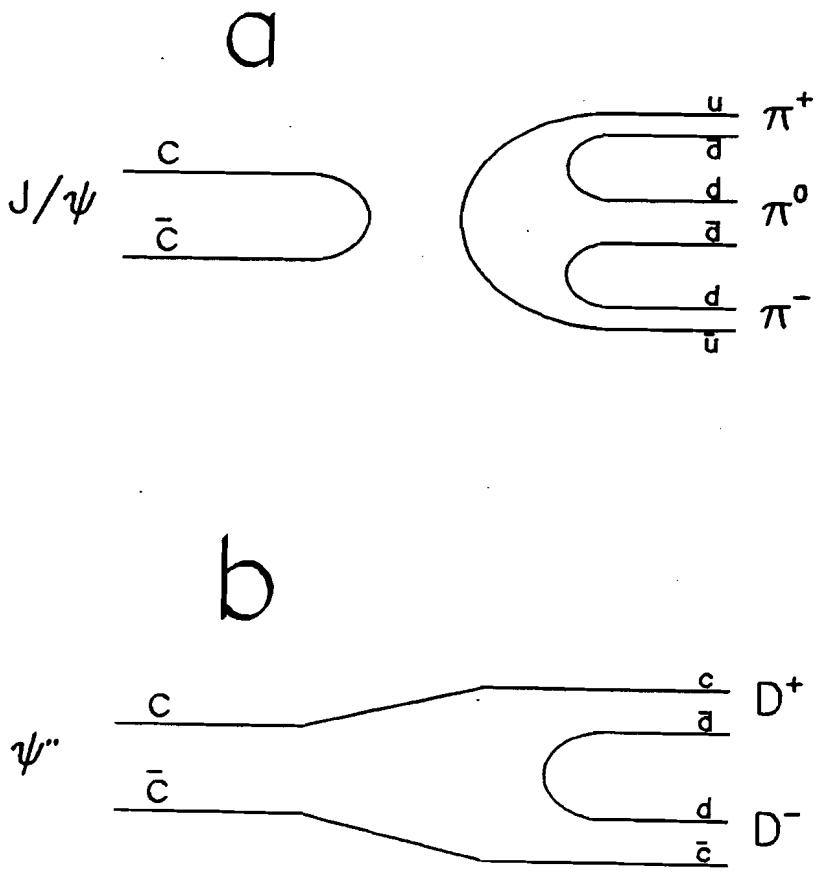

Figure 1.1: OZI suppressed and favored decays: a) OZI suppressed decay $J/\psi \to \pi^+\pi^-\pi^0$, and b) OZI favored decay $\psi'' \to D^+D^-$ (gluon lines are not shown).

In 1977, a fifth quark, b (*bottom*), was discovered at Fermilab [28]. It has a mass of ~ 5 GeV/c^2, and with its antiquark it forms a spectrum of bound states called bottomonium. Finding the partner of the b quark – the predicted *top* quark, is currently one of the major goals in experimental particle physics.

1.2 Theoretical description of charmonium

Due to the heavy mass of the c quark, in the first approximation charmonium can be treated as a non-relativistic system. The velocity of the quarks in charmonium can be roughly estimated using the virial theorem

$$2\langle T\rangle = \langle \vec{r}\cdot\vec{\nabla}V(\vec{r})\rangle, \tag{1.1}$$

where $\langle T\rangle = 2\frac{m_c\langle v^2\rangle}{2}$ is the total kinetic energy, m_c is the charmed quark mass, and $\vec{v}$ its velocity. If, motivated by the QCD idea of confine ment, we assume that the quark-antiquark potential is proportional to the distance, $V = ar$, we obtain

$$\langle v^2\rangle = \frac{E_{bin}}{3m_c}, \tag{1.2}$$

where $E_{bin} = \langle T\rangle + \langle V\rangle$ is the binding energy. Taking $E_{bin} \approx m(\psi'')c^2 - m(J/\psi)c^2 = 673\,\mathrm{MeV}$, and $m_c \approx 1.5\,\mathrm{MeV/c^2}$, we get

$$\langle v^2\rangle \approx 0.15c^2. \tag{1.3}$$

It is interesting to note that a similar calculation for light quark-antiquark systems (i.e. light mesons) yields $\langle v^2\rangle \approx 0.6c^2$, while for the bottomonium $\langle v^2\rangle \approx 0.07c^2$. Thus, charmonium is

the lightest quark-antiquark system where the non-relativistic treatment seems appropriate.

Energy levels and wave-functions for the charmonium system can thus be obtained by solving the Schrödinger equation with a phenomenological quark-antiquark potential. Well known techniques of atomic physics can be used to calculate various properties of charmonium spectroscopy, such as fine and hyperfine splitting, leptonic widths and radiative transition rates.

A charmonium state, like any fermion-antifermion system, has parity

$$P = (-1)^{L+1}, \tag{1.4}$$

and charge-conjugation parity

$$C = (-1)^{L+S}, \tag{1.5}$$

where L is the angular momentum, and S is the total spin of the system, $\vec{S} = \vec{S_1} + \vec{S_2}$, ($\vec{S_1}$ and $\vec{S_2}$ are spins of the quarks). Charmonium states are often labelled using the quantum numbers J^{PC}, where J is the total spin of the system, $\vec{J} = \vec{L} + \vec{S}$, or using the spectroscopic notation $n^{2S+1}L_J$, where n is the radial quantum number, and the angular momentum $L = 0, 1, 2$ is labelled by the letters S, P, D.

Fig. 1.2 shows the masses, names and quantum numbers of charmonium states.

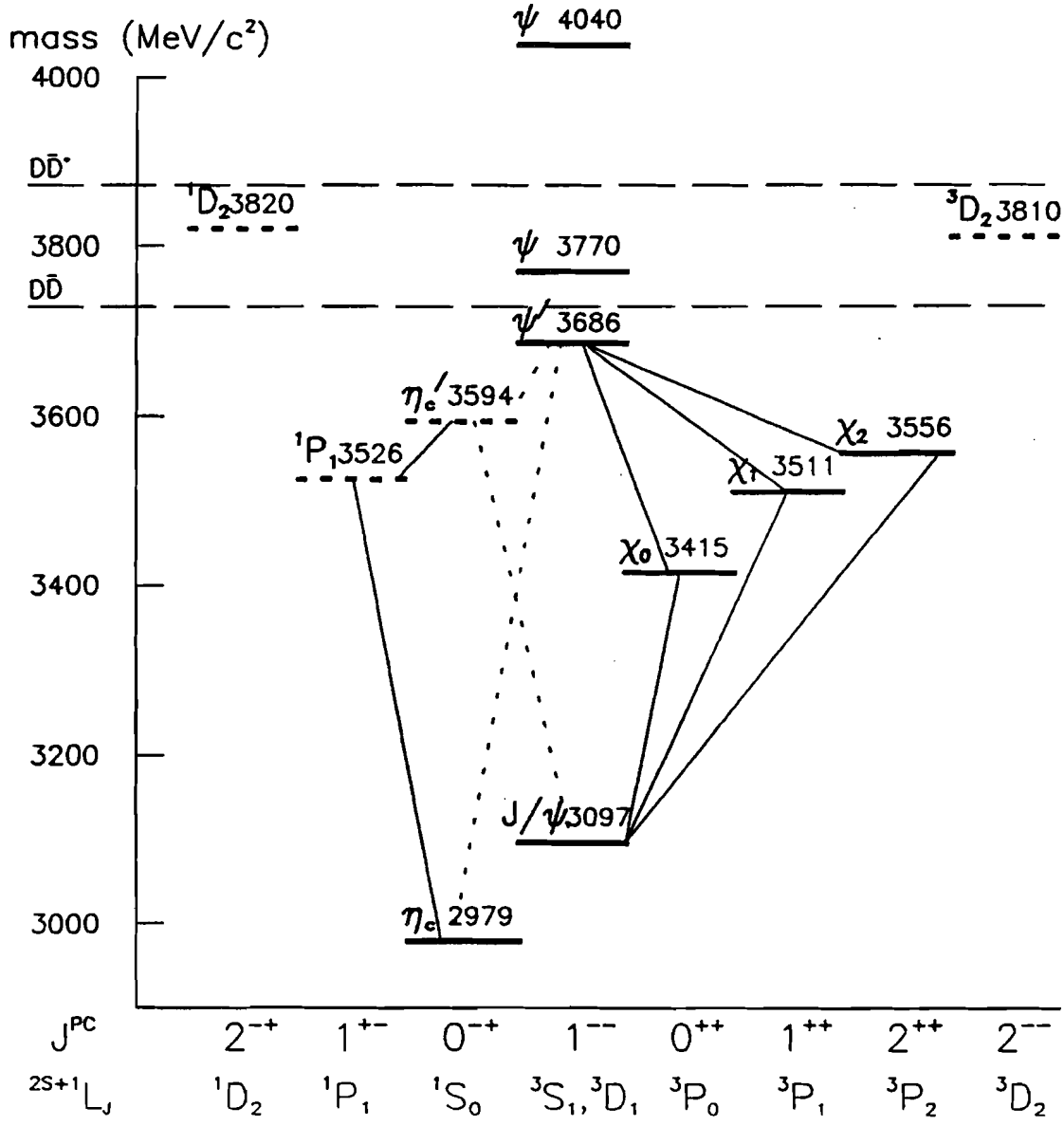

Figure 1.2: Charmonium spectrum. States indicated by solid lines are well established experimentally [22], the $^1P_1$ and η_c' states need confirmation [46,26], the $^1D_2$ and $^3D_2$ states have not been seen. Radiative transitions between known narrow states are also indicated by solid (E1) and dashed (M1) lines.

1.2.1 Potential models

The Cornell potential,

$$V(r) = -\frac{4}{3}\frac{k}{r} + ar, \tag{1.6}$$

with $k = 0.52$ and $a = 2.34\,\mathrm{GeV}^{-1}$, was the first successful potential used to describe the charmonium system [21, 29, 30]. The first Coulomb-like term of the potential was motivated by the idea that at short distances the quark-antiquark interaction should be dominated by one gluon exchange. The second term, which rises linearly with the distance, reflects the QCD concept of quark confinement.

Several other forms of the c-$\bar{c}$ potential were proposed, including the logarithmic potential $V(r) = c\,ln(r/r_0)$ [31], and the power law potential $V(r) = B + Ar^{\nu}$ [32]. The potential suggested by Richardson [33] is worth mentioning, because it incorporates the concepts of linear quark confinement and of asymptotic freedom in a universal manner. Asymptotic freedom requires that at large momentum transfers (or at small distances r), the strong coupling constant behaves as

$$\lim_{q^2 \gg \Lambda^2} \alpha_s(q^2) \propto \frac{12\pi}{33 - 2n_f}\,\frac{1}{ln(q^2/\Lambda^2)}, \tag{1.7}$$

where n_f is the number of flavors, and Λ is the QCD scale parameter. The formula for the c-$\bar{c}$ potential in the momentum space,

$$\tilde{V}(q^2) = -\frac{4}{3}\,\frac{12\pi}{33 - 2n_f}\,\frac{1}{q^2}\,\frac{1}{ln(1 + q^2/\Lambda^2)}, \tag{1.8}$$

interpolates between the one-gluon exchange potential at short distances, $\tilde{V}(q^2) = \frac{4}{3}\frac{\alpha_s(q^2)}{q^2}$, and the long distance linear confinement, $V(r) \propto r$, which corresponds to $\tilde{V}(q^2) \propto 1/(q^2)^2$.

In fact, all these potentials coincide for distances r from 0.2 to 1 fm, which correspond to

the sizes of charmonium states lying below the $D\bar{D}$ threshold [1] (see Fig. 1.3). Another very important fact is that these potentials describe the bottomonium system equally well as the charmonium system, with the same potential parameters (except for the quark mass), which proves that the potential is flavor-independent.

The phenomenological approach to the q-$\bar{q}$ potential has been very popular, because of its simplicity and good agreement with the experimental results. Alternative approaches, which attempt to derive the q-$\bar{q}$ potential from the first principles of QCD, are discussed in chapter 6 of Ref. [2].

1.2.2 Spin-dependent effects

The fine and hyperfine splitting between charmonium levels are the result of relativistic corrections to quark-antiquark interaction. The splitting can be calculated by using the Bethe-Salpeter equation [34], which describes the relativistic interaction of a bound two-fermion system, and expanding it in powers of v^2/c^2 (or, equivalently, $1/m_c$). The result depends on the Lorentz structure of the quark-antiquark potential; the spin-independent potential is assumed to be

$$V_0 = V_C + V_S + V_V, \tag{1.9}$$

where $V_C = -\frac{4}{3}\frac{k}{r}$ is the short-range Coulomb-like potential, due to single gluon exchange and thus of vector nature; the long-range potential, of unknown Lorentz structure, is assumed to be a sum of a scalar and a vector part, $V_S + V_V$. The resulting spin-dependent potential is [10]

[1] Lowest mass charmed meson pair.

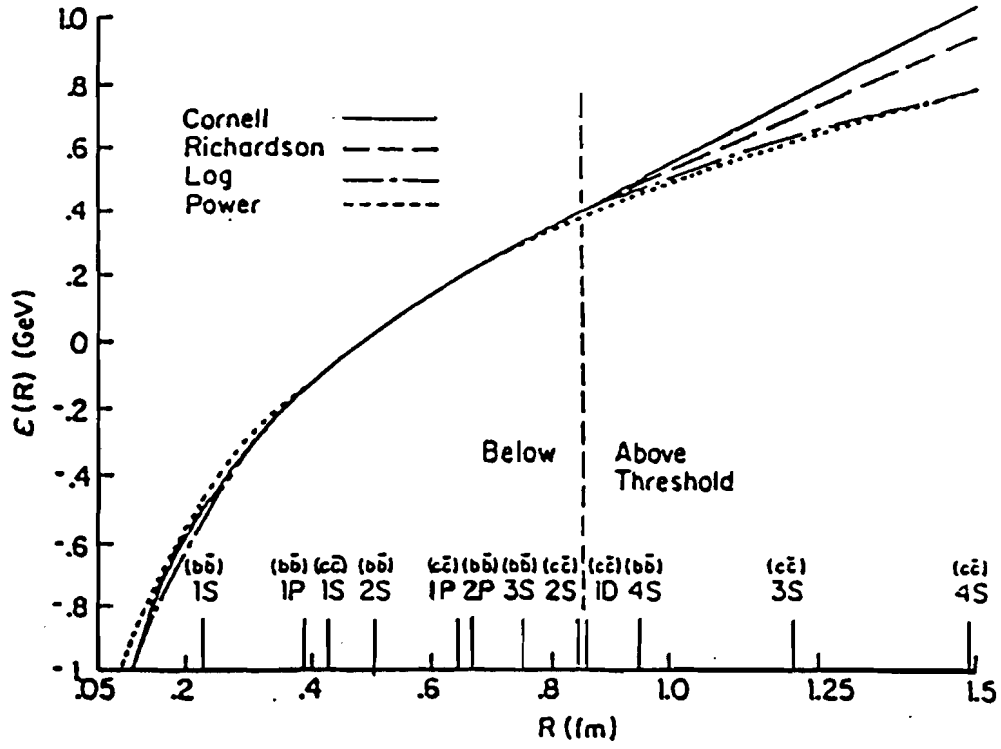

Figure 1.3: Comparison of several quark-antiquark potentials. The sizes of $c\bar{c}$ and $b\bar{b}$ bound states are indicated on the abscissa. From Ref. [11].

$$V_{spin} = \frac{1}{2m_c^2}\left[\frac{16k}{3r^3} + 4\frac{1}{r}\frac{dV_V}{dr} - \frac{1}{r}\frac{dV_0}{dr}\right]\vec{L}\cdot\vec{S} + \frac{2}{3m_c^2}\left[\frac{16}{3}\pi k\delta(\vec{r}) + \nabla^2 V_V(r)\right]\vec{S}_1\cdot\vec{S}_2 + \frac{1}{3m_c^2}\left[\frac{4k}{r^3} + \frac{1}{r}\frac{dV_V}{dr} - \frac{d^2V_V}{dr^2}\right]S_{12}, \quad (1.10)$$

where the tensor operator $S_{12} = 3\,\vec{S}_1\cdot\hat{\vec{r}}\,\vec{S}_2\cdot\hat{\vec{r}} - \vec{S}_1\cdot\vec{S}_2$. (More general approaches to the spin-dependent forces in charmonium are discussed in chapter 3 of Ref. [2].)

The spin-spin part of V_{spin} is responsible for the splitting between spin singlet and spin triplet states, such as $m(J/\psi) - m(\eta_c)$ and $m(\psi') - m(\eta_c')$, and also between $m(^1P_1)$ and the *center of gravity* of the ^3P_J states, defined as

$$m(c.o.g.) = \frac{m(^3P_0) + 3m(^3P_1) + 5m(^3P_2)}{9}. \quad (1.11)$$

It should be noted that the spin-spin splitting between the $m(^1P_1)$ and the $m(c.o.g.)$ is due only to the vector part of the confining potential, since the term proportional to $\delta(\vec{r})$ vanishes for $L \neq 0$. Thus, the value of the splitting can be used as a test of the Lorentz structure of the confining potential. The same is true for the splitting between the $^1D_2$ state and the *center of gravity* of the ^3D_J states.

The splitting between the $^3P_2$, $^3P_1$, $^3P_0$ states, and also between the $^3D_3$, $^3D_2$ and $^3D_1$ states, is due to the spin-orbit and tensor forces.

1.2.3 Charmonium decays

Total widths of charmonium states lying below the $D\bar{D}$ threshold are dominated by annihilations to two or three gluons, which show up as hadrons in the final state. Some states undergo hadronic transitions to lower mass states, emitting light mesons (e.g. $\psi' \to J/\psi\,\pi^+\pi^-$). Electromagnetic decays also play an important role, in some cases with branching ratios

Table 1.1: Allowed annihilations into gluons and photons; only the lowest allowed configurations are given, g^* and γ^* denote virtual gluons and photons.

$^{2S+1}L_J$	J^{PC}	states	annihilation to gluons	annihilation to photons
$^1S_0$	0^{-+}	η_c, η_c'	$2g$	2γ
$^3S_1$	1^{--}	J/ψ, ψ'	$3g$	$\gamma^*\rightarrow e^+e^-$ or $\mu^+\mu^-$ 3γ
$^3P_0$	0^{++}	χ_0	$2g$	2γ
$^3P_1$	1^{++}	χ_1	$gg^*\rightarrow gq\bar{q}$ $3g$	$\gamma\gamma^*\rightarrow\gamma q\bar{q}$ 4γ
$^3P_2$	2^{++}	χ_2	$2g$	2γ
$^1P_1$	1^{+-}	$^1P_1$	$3g$	3γ

comparable to strong decays. They include radiative transitions between charmonium states (e.g. $\psi'\rightarrow\chi_J\,\gamma$), and decays of the J/ψ and its radial excitations into e^+e^- or $\mu^+\mu^-$ via a virtual photon. Annihilations into two or three photons have small branching ratios, but their measurement is important for comparison with theoretical predictions. The decays of charmonium are shown schematically in Fig. 1.4. It should be noted that, because of angular momentum and parity conservation, the $^1D_2$ and $^3D_2$ states cannot decay into charmed mesons, even though their predicted masses (3790-3820 MeV/c^2 for $^1D_2$ and 3800-3810 MeV/c^2 for $^3D_2$ [1,35]) are above the $D\bar{D}$ threshold of 3729 MeV/c^2. They cannot decay into $D\bar{D}^*$ either, because their masses are lower than the threshold at 3872 MeV/c^2; thus they can only decay through OZI-suppressed channels, and are supposed to be as narrow as the lower lying charmonium states.

a) Annihilations

Table 1.1 lists the allowed annihilations into gluons and photons of the charmonium states. The allowed decays have to satisfy the following conditions:

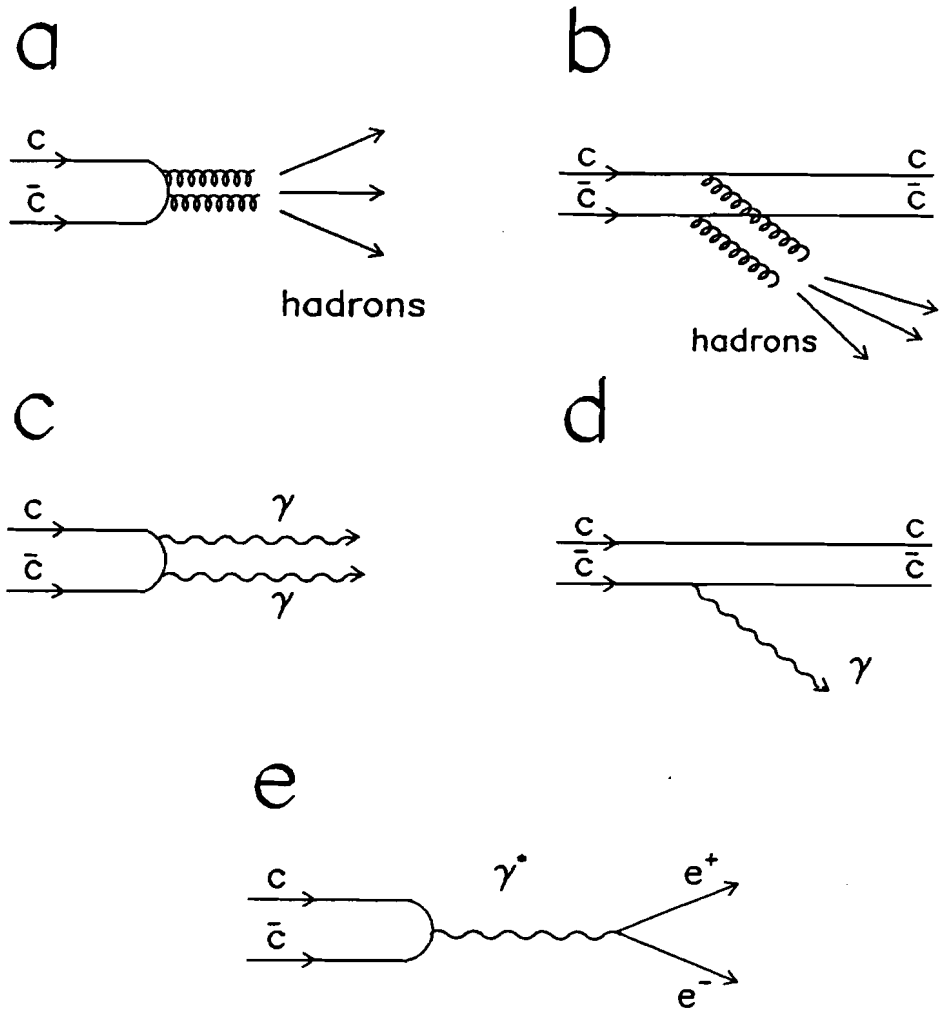

Figure 1.4: Decays of charmonium: a) annihilation to 2 or 3 gluons, b) hadronic transition, c) annihilation to 2 or 3 photons, d) radiative transition, e) annihilation to e^+e^- or $\mu^+\mu^-$ through a virtual photon.

a) final state must be a color singlet, so decays into one gluon are forbidden,

b) C-parity must be conserved; the 2-gluon and 2-photon final states have $C = +1$, the 3-photon final state has $C = -1$, while the 3-gluon combination can have either $C = +1$ or $C = -1$ [9],

c) a massive spin-1 particle cannot decay into two massless spin-1 particles (Yang's theorem [36]),

d) only the $J^{PC} = 1^{--}$ states can decay into e^+e^- or $\mu^+\mu^-$ via a virtual photon.

Perturbative QCD predictions for annihilation decay rates have been summarized in Table 6 of Ref. [1]. The annihilation rates of the S states are proportional to the square of the wave function at the origin, while for the $L \neq 0$ states the decay rates are proportional to the square of the L-th derivative of the radial wave function at $r = 0$. Since properties of the wave functions are derived from model-dependent potentials, predictions for ratios of decay rates, in which the wave function dependence cancels out, are usually more reliable than predictions for the absolute rates.

Radiative QCD corrections are another source of uncertainty in predictions for the annihilation rates. The first order corrections can be as big as 30% [1], which suggests that higher order terms, which have not been calculated, may be important.

b) Radiative transitions

Radiative transitions with the emission of one photon are allowed between charmonium states of opposite C-parity. The interaction of a charmonium state with the electromagnetic field of a photon can be described by a non-relativistic Hamiltonian [9]

$$\mathcal{H}_{em} = -e_c\frac{\vec{v}}{2}\left[\vec{A}(\frac{\vec{r}}{2}) + \vec{A}(-\frac{\vec{r}}{2})\right] + \frac{\mu_c}{2}\vec{\Delta}\left[\vec{H}(\frac{\vec{r}}{2}) + \vec{H}(-\frac{\vec{r}}{2})\right] - \mu_c\vec{S}\left[\vec{H}(\frac{\vec{r}}{2}) - \vec{H}(-\frac{\vec{r}}{2})\right], \quad (1.12)$$

where $\vec{A}$ and $\vec{H}$ are vector potential and magnetic field, $\vec{r}$ is the quark-antiquark distance, $\vec{v} = \frac{d\vec{r}}{dt}$, and e_c and μ_c are electric charge and magnetic moment of the c quark. $\vec{S} = 1/2(\vec{\sigma_1} + \vec{\sigma_2})$ and $\vec{\Delta} = \vec{\sigma_1} - \vec{\sigma_2}$, where $\vec{\sigma_1}$, $\vec{\sigma_2}$ are Pauli matrices corresponding to quark spins. The first term in the Hamiltonian describes the interaction of the charge with the electric field, and the second and third term describe the interaction of the magnetic moment with the magnetic field. Symmetry properties of the terms in $\mathcal{H}_{em}$ determine selection rules for different types of radiative transitions. The first term is parity-odd and independent of spin, therefore it connects states of opposite parity and of the same spin. By similar arguments, the second term links states of the same parity and different spins, and the third term connects states of opposite parity and non-zero spin. The dominating radiative transitions between charmonium states are shown in Fig. 1.2.

The rates for radiative transitions are proportional to the squared matrix element $|\langle f|\mathcal{H}_{em}|i\rangle|^2$, where f and i denote final and initial charmonium states. In the long wavelength approximation (in which the factor $e^{-i\vec{k}\cdot\vec{r}}$ in the expression for the electromagnetic field is approximated by 1), the rates for the electric (E1) and magnetic (M1) decays are [9]

$$\left.\begin{array}{l}\Gamma_{E1}(n^3S_1 \to n'^3P_J\,\gamma) \\ \Gamma_{E1}(n^3P_J \to n'^3S_1\,\gamma)\end{array}\right\} = \frac{4}{27}(2J_f+1)e_c^2\alpha E_\gamma^3|E_{if}|^2, \tag{1.13}$$

$$\Gamma_{M1}(n^3S_1 \to n'^1S_0\,\gamma) = \frac{16}{3}\mu_c^2\alpha E_\gamma^3|M_{if}|^2, \tag{1.14}$$

where J_f is the spin of the final charmonium state, E_γ is photon energy, and

$$E_{if} = \int r^3 R_i(r)R_f(r)dr, \tag{1.15}$$

$$M_{if} = \int r^2 R_i(r)R_f(r)dr, \tag{1.16}$$

for the appropriate initial and final state radial wave functions R_i and R_f. The overlap

integral M_{if} vanishes for $n \neq n'$, due to the orthogonality of the wave functions. Thus, in the non-relativistic limit, the radiative transition $\psi' \rightarrow \eta_c \gamma$ is forbidden.

Comparison of experimental data with the above predictions shows that the non-relativistic description is not adequate in this case. The experimental E1 rates are a factor of 2-3 smaller than the predictions; also the non-relativistically forbidden transition $\psi' \rightarrow \eta_c \gamma$ has been observed [22]. The calculations which include relativistic corrections are generally in better agreement with experimental data [37–40].

1.3 Charmonium in $p\bar{p}$ annihilations

1.3.1 The experimental situation before E-760

The majority of the data on the charmonium system comes from experiments carried out with e^+e^- colliding beams. In e^+e^- annihilations only the charmonium states with quantum numbers of the photon, $J^{PC} = 1^{--}$, can be formed in the first-order process, $e^+e^- \rightarrow \gamma^* \rightarrow c\bar{c}$. Other charmonium states, such as χ_0, χ_1, χ_2, η_c and η_c', can be observed in radiative transitions from the J/ψ or ψ'. For the states which are formed directly in e^+e^- annihilation, the accuracy of mass and width measurements depends on the beam energy resolution, which is usually very good. However, for the states seen in radiative transitions, the accuracy is determined by the energy resolution of the detector, and is much poorer than for the directly formed states. For example, mass of the J/ψ was measured in an e^+e^- experiment with the accuracy of 0.09 MeV/c^2 [41], while mass measurements of the χ_0, χ_1 and χ_2 states, using radiative decays from the ψ', have the uncertainty of 4 MeV/c^2 [42]. In addition, event rates in radiative decays are suppressed by radiative decay branching ratios, which vary from ~ 0.1 (for $\psi' \rightarrow \chi_J \gamma$) to ~ 0.01 (for $J/\psi \rightarrow \eta_c \gamma$) [22]. The $^1P_1$ state cannot be accessed by one-photon radiative transitions from J/ψ or ψ', because of C-parity

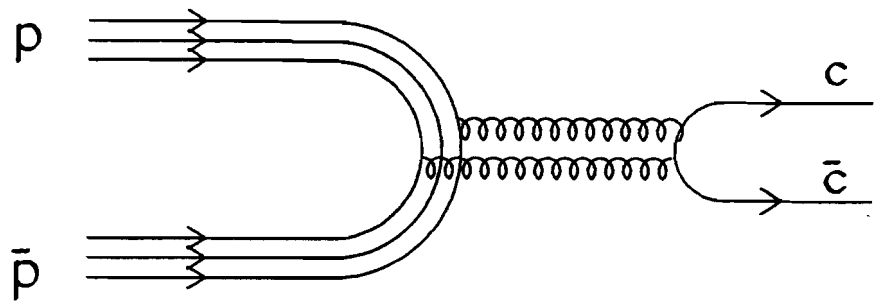

Figure 1.5: Formation of charmonium states in $p\bar{p}$ annihilation.

conservation. The $^1D_2$ and $^3D_2$ states cannot be accessed in this way either, because they have higher masses than the ψ'.

As a result of these experimental limitations, the information on charmonium states obtained in e^+e^- experiments was quite incomplete. Only in the cases of the J/ψ and its radial excitations were the parameters such as mass, total width and branching ratios precisely measured. Total and partial widths of the χ_J states and of the η_c were poorly known; the η_c' state was seen by only one experiment, and still needs to be confirmed; the states $^1P_1$, $^1D_2$ and $^3D_2$ were not seen at all [43].

1.3.2 Charmonium in $p\bar{p}$ annihilations: R704 and E-760

In proton-antiproton annihilations, all charmonium states can be formed directly[2], through a two- or three-gluon intermediate state (Fig. 1.5). In $p\bar{p}$ annihilation experiments, the masses and total widths of charmonium states are determined by analyzing event yields as a function of center of mass energy; thus, the accuracy is limited only by

[2]Formation of the η_c, η_c', χ_0 and $^1P_1$ states may be suppressed by the QCD helicity selection rule; this is discussed in more detail in section 2.2.1a.

beam momentum resolution, as in e^+e^- experiments.

Construction of antiproton accumulator rings at CERN and at Fermilab made it possible to study charmonium states formed in $p\bar{p}$ annihilations. The technique was pioneered in 1983-1984 by the CERN experiment R704 [44], which used the antiproton beam circulating in the ring 2 of the Intersecting Storage Rings (ISR), and an internal H_2 gas jet target. R704 proved the feasibility of the technique; however, because of the ISR shutdown, only a few weeks of effective data taking was possible. Thus, many questions about the charmonium spectrum remained unanswered.

In 1985, experiment E-760 at Fermilab was proposed, in order to further study charmonium states formed in $p\bar{p}$ annihilations [45]. E-760 uses the same technique as R704, but with greater detector acceptance, better beam energy resolution, higher instantaneous luminosity (which determines event rates), and much longer running time, which means it is able to study charmonium states with much better precision.

A challenge in $p\bar{p}$ charmonium experiments is to pick out the signal from a very large non-resonant hadronic background, which is a factor of 10^6-10^8 larger than the signal. It is thus impractical to search for hadronic decay modes of charmonium. Instead, electromagnetic decays (or hadronic transitions to J/ψ, with J/ψ decaying to e^+e^-), which provide clean signatures, can be used. Examples of such decays are given below

$$\eta_c \rightarrow \gamma\gamma, \tag{1.17}$$

$$J/\psi \rightarrow e^+e^-, \tag{1.18}$$

$$\chi_0 \rightarrow J/\psi\,\gamma \rightarrow e^+e^-\gamma, \tag{1.19}$$

$$\chi_0 \rightarrow \gamma\gamma, \tag{1.20}$$

$$\chi_1 \rightarrow J/\psi\,\gamma \rightarrow e^+e^-\gamma, \tag{1.21}$$

$$\chi_2 \rightarrow J/\psi\,\gamma \rightarrow e^+e^-\gamma, \tag{1.22}$$

$$\chi_2 \rightarrow \gamma\gamma, \tag{1.23}$$

$$^1P_1 \rightarrow J/\psi\pi^0 \rightarrow e^+e^-\gamma\gamma, \tag{1.24}$$

$$^1P_1 \rightarrow J/\psi\pi^+\pi^- \rightarrow e^+e^-\pi^+\pi^-, \tag{1.25}$$

$$^1P_1 \rightarrow \eta_c\gamma \rightarrow \gamma\gamma\gamma, \tag{1.26}$$

$$\psi' \rightarrow e^+e^-, \tag{1.27}$$

$$\psi' \rightarrow J/\psi + anything \rightarrow e^+e^- + anything, \tag{1.28}$$

$$\eta_c' \rightarrow \gamma\gamma. \tag{1.29}$$

Experiment E-760 took data during two running periods: July through August, 1990, and August through December, 1991. The results include discovery of the $^1P_1$ state [46], the first measurement of the total width of the χ_1 and improved measurements of the χ_2 width and of the χ_1, χ_2 masses [47], measurement of the total widths of the J/ψ and ψ' and of the J/ψ mass [48,49], measurement of the $p\bar{p}$ branching ratios of the J/ψ, ψ', χ_1 and χ_2, measurement of the $\gamma\gamma$ partial widths of the χ_2 and η_c [50,51], and measurement of angular distributions in radiative decays of χ_1 and χ_2 (this analysis). The results are summarized in Table 1.2. For comparison, previous world average results from Ref. [43] are also given.

Several open questions in charmonium spectroscopy are left for the next run of the E-760, which is scheduled to start in the fall of 1994 [52]. They include confirmation of the $^1P_1$ state and precise measurement of its parameters, search for the η_c', $^1D_2$ and $^3D_2$ states, and measurement of parameters of the χ_0 state. In particular, E-760 did not measure the χ_0 during the 1990-1991 running period, because the cross section for the reaction 1.19, which is proportional to $(2J+1) \times BR(\chi_0 \rightarrow p\bar{p}) \times BR(\chi_0 \rightarrow J/\psi\gamma)$, is at least a factor of 100 smaller than in the cases of χ_1 and χ_2 [22].

Table 1.2: Summary of E-760 results from the 1990-1991 running period; for comparison, previous world average results from Ref.[43] are shown in parentheses; statistical and systematic errors have been added in quadrature.

state	mass [MeV/c^2]	total width [MeV]	BR($p\bar{p}$) [$\times 10^{-4}$]	other measurements	Ref.
χ_1	3510.53 ± 0.13 (3510.6 ± 0.5)	0.88 ± 0.14 (< 1.3, 95%CL)	0.78 ± 0.15 (0.54 - 12.0)	angular distribution	[47], this anal.
χ_2	3556.15 ± 0.14 (3556.3 ± 0.4)	1.98 ± 0.18 ($2.6 \pm {}^{1.2}_{0.9}$)	0.91 ± 0.16 ($0.90 \pm {}^{0.45}_{0.32}$)	$\Gamma_{\gamma\gamma} = 342 \pm {}^{115}_{110}$eV ($280 \pm 200$), angular distribution	[47,50], this anal.
$^1P_1$	3526.2 ± 0.25 (—)	< 1.1 (90%CL) (—)			[46]
J/ψ	3096.87 ± 0.05 (3096.93 ± 0.09)	0.099 ± 0.013 (0.068 ± 0.010)	$18.2 \pm {}^{3.9}_{3.5}$ (21.6 ± 1.1)		[48,49]
ψ'		0.306 ± 0.039 (0.243 ± 0.043)	$2.61 \pm {}^{0.43}_{0.40}$ (1.9 ± 0.5)		[48,49]
$\eta_c{}^a$	2989.9 ± 2.2 (2979.6 ± 1.6)	15.5 ± 9.3 ($10.3 \pm {}^{3.8}_{3.4}$)		$\Gamma_{\gamma\gamma} = 5.4 \pm 3.4$keV ($8 \pm {}^{7}_{5}$)	[51]

[a]Preliminary.

Chapter 2

Theory of angular distributions in

$$p\bar{p} \rightarrow \chi_J \rightarrow J/\psi\ \gamma \rightarrow e^+e^-\gamma$$

The angular distribution for the reactions

$$p\bar{p} \rightarrow \chi_J \rightarrow J/\psi\ \gamma \rightarrow e^+e^-\gamma \qquad (J = 0, 1, 2) \qquad (2.1)$$

can be described using the helicity formalism. Such a description depends only on the kinematics of the process, and does not make any assumptions about dynamics of $p\bar{p}$ annihilation or radiative decay of the χ_J. Dynamical information enters the formula in the form of free parameters which can be determined by experiment. The parameters are sensitive to the features of the $p\bar{p}$ annihilation process, the properties of the $c\bar{c}$ bound state and the nature of its radiative decay.

In the first section of this chapter (2.1) I define the angles used to describe events, present a general angular distribution formula for the reactions 2.1, and discuss specific cases of $J = 0$, 1 and 2. In the second section (2.2) I review theoretical predictions for the dynamical parameters of the angular distribution.

2.1 Angular distribution function in the helicity formalism

2.1.1 Definition of angles

The kinematics of reactions 2.1 are conventionally described using three angles: θ, θ' and ϕ', which are defined as follows (see Fig. 2.1):

θ is the polar angle of the J/ψ in the χ_J rest frame, with the Z axis along the $\bar{p}$ direction;

θ' is the polar angle of the e^+ in the J/ψ rest frame, with the Z' axis opposite to the γ direction;

ϕ' is the azimuthal angle of the e^+ in the J/ψ rest frame; the X' axis is in the plane defined by the $\bar{p}$ and γ, and its direction is chosen in such way that $\phi'(\bar{p}) = 0$.

It is important to specify the angles unambiguously, because differences in definitions (e.g. $\phi' \to \phi' + \pi$) between theory and experiment can lead to confusion. I am using the same definition as Ridener *et al.* [3], whose formula is used in this analysis. The definition of θ in the R704 paper [7] is different than ours, $\theta_{R704} = \pi - \theta_{E760}$.

2.1.2 General form of the angular distribution function

The helicity λ of a particle is defined as the component of its spin $\vec{J}$ along its direction of motion,

$$\lambda = \vec{J} \cdot \frac{\vec{p}}{p}, \tag{2.2}$$

where $\vec{p}$ is the momentum of the particle.

Helicity is well defined for both massive and massless particles. It is invariant under ordinary rotations and under Lorentz boosts along the direction of $\vec{p}$ [1]. These features make

[1] For boosts along $\vec{p}$, helicity changes sign if the boost velocity is greater than the velocity of the particle.

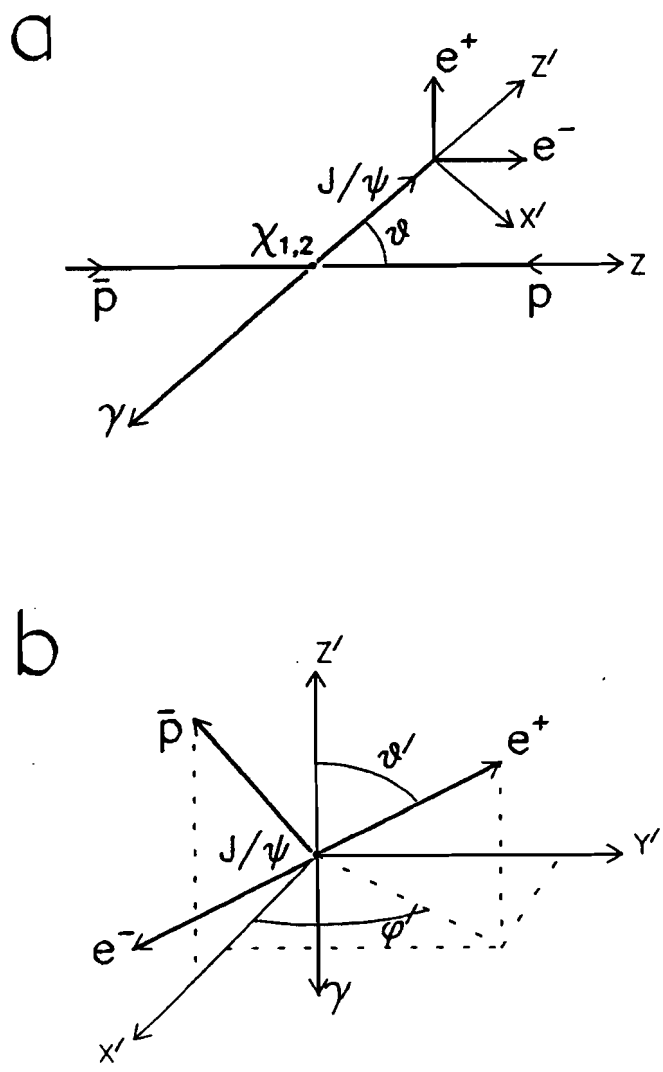

Figure 2.1: Definition of angles θ, θ' and ϕ': (a) χ_J rest frame, (b) J/ψ rest frame (γ, Y', and Z' are in the plane of the paper).

the helicity formalism a convenient tool for describing angular distributions in relativistic scattering and decay processes [53].

The angular distribution in reactions 2.1 is described by the following formula [3]:

$$W_J(\theta,\theta',\phi') = \frac{3(2J+1)}{64\pi^2}\sum_{\lambda=0,\pm1}|B^J_\lambda|^2\sum_{\nu,\nu'=-J}^{J}\sum_{\mu=\pm1}A^J_{|\nu|}A^{J*}_{|\nu'|}d^J_{\nu\lambda}(\theta)d^J_{\nu'\lambda}(\theta) \times\sum_{k=\pm1}D^1_{\sigma' k}(\phi',\theta',-\phi')D^{1*}_{\sigma k}(\phi',\theta',-\phi'). \quad (2.3)$$

The helicity amplitudes B^J_λ, A^J_ν are dynamical parameters of the formation and decay processes. The indices denote particle helicities, which are defined as follows (see Fig. 2.2):

λ is the projection of the χ_J spin on the $\bar{p}$ direction;

ν is the projection of the χ_J spin on the J/ψ direction;

μ is the helicity of the photon;

σ $= \nu + \mu$ is the helicity of the J/ψ, $\sigma' = \nu' + \mu$;

k is the component of the total angular momentum of the e^+e^- system in the e^+ direction.

Rotation matrices $D^I_{mn}(\alpha,\beta,\gamma)$ can be written as $D^I_{mn}(\alpha,\beta,\gamma) = e^{-i\alpha m}d^I_{mn}(\beta)e^{-i\gamma n}$, and the explicit form of the d^I_{mn} functions can be found in Refs. [54].

I now discuss the helicity amplitudes in more detail. The spin projection of the χ_J on the $\bar{p}$ direction is described by the formation helicity amplitude B_λ. The χ_J helicity $\lambda(\chi_J)$ equals $\lambda(\bar{p}) - \lambda(p) = 0, \pm1$, so B_λ can also be written as $B_{\lambda(\bar{p}),\lambda(p)}$. Parity and charge-conjugation invariance imply that helicity amplitudes satisfy the following relations [55]

$$B^J_{\lambda_1,\lambda_2} = \eta_P(-1)^J B^J_{-\lambda_1,-\lambda_2}, \quad (2.4)$$

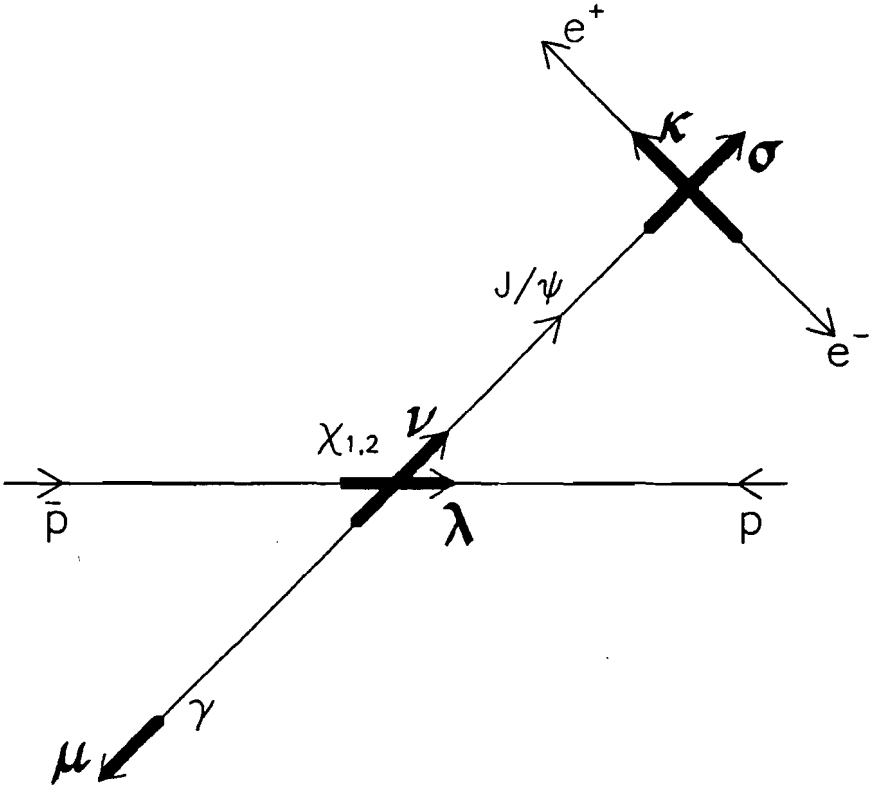

Figure 2.2: Schematic sketch showing helicities in the reactions $p\bar{p} \to \chi_J \to J/\psi\gamma \to e^+e^-\gamma$.

and

$$B^J_{\lambda_1,\lambda_2} = \eta_C(-1)^J B^J_{\lambda_2,\lambda_1}, \tag{2.5}$$

where η_P and η_C are parity and C-parity eigenvalues of the charmonium state. From parity conservation, $B_{+1} \equiv B_{+\frac{1}{2},-\frac{1}{2}} = \eta_P(-1)^J B_{-\frac{1}{2},+\frac{1}{2}} \equiv \eta_P(-1)^J B_{-1}$, and thus $|B_1|^2 = |B_{-1}|^2$. I will use the notation $B_1^2 \equiv |B_1|^2 = |B_{-1}|^2$ and $B_0^2 \equiv |B_0|^2$, and the normalization condition

$$B_0^2 + 2B_1^2 = 1. \tag{2.6}$$

This condition leaves one independent formation helicity amplitude as a free parameter of the angular distribution.

Helicity amplitudes A_ν describe the spin component of the χ_J in the J/ψ direction. The allowed values of ν are $-J, -J+1, ...J$, with the constraint that the absolute value of J/ψ helicity $|\sigma| = |\nu + \mu|$ must be ≤ 1. Again, from parity conservation, I get $A_\nu = (-1)^J A_{-\nu}$ ($\nu \neq 0$), which leaves $(J+1)$ independent helicity amplitudes $A_0, A_1, ...A_J$. After imposing the following normalization condition,

$$\sum_{\nu=0}^{J} |A_\nu|^2 = 1, \tag{2.7}$$

we are left with J independent amplitudes A_ν. They can be expressed as linear combinations of multipole transition amplitudes a_k ($k=1, ..J+1$),

$$A_\nu = \sum_{k=1}^{J+1} a_k \sqrt{\frac{2k+1}{2J+1}} \langle k, 1; 1, \nu - 1 | J, \nu \rangle. \tag{2.8}$$

The explicit transformation from A_ν to a_k for $J = 1, 2$ can be found in Ref. [56]. The

multipole amplitudes also satisfy the normalization condition,

$$\sum_{k=1}^{J+1} |a_k|^2 = 1, \tag{2.9}$$

and conventionally it is assumed that $a_1 \geq 0$. Since χ_J and J/ψ have opposite parities, the amplitudes a_1, a_2 and a_3 correspond to electric dipole (E1), magnetic quadrupole (M2) and electric octupole (E3) transitions.

In general the amplitudes B_λ and A_ν can be complex numbers. However, the angular distribution is only sensitive to the absolute values of the formation amplitudes B_λ (Eq. 2.3). In addition, because the imaginary part of A_ν is predicted to be very small (see Eqs.2.20-2.22), I will assume that A_ν and a_k are real.

2.1.3 Specific cases of χ_0, χ_1 and χ_2

a) χ_0

For the χ_0, which has quantum numbers $J^{PC} = 0^{++}$, the spin component in any direction must be equal to zero, and consequently $B_1 = 0$ and $A_1 = A_2 = 0$. In terms of multipole transitions only the dipole transition is allowed, so $a_1 = 1$ and $a_2 = a_3 = 0$. This also follows from angular momentum conservation, since for a radiative transition of multipolarity k (with corresponding amplitude a_k) between the states of total angular momentum J_i and J_f, the angular momentum carried by the photon must satisfy $J_i + J_f \geq k \geq |J_i - J_f|$.

Consequently, the angular distribution function does not contain any dynamical parameters and is given by

$$W_0(\theta, \theta', \phi') = \frac{3}{64\pi^2}(1 + \cos^2\theta'). \tag{2.10}$$

Because there are no free parameters in this angular distribution, it would be useful as a test of the angular distribution analysis. However, E-760 did not collect any χ_0 data during

the 1990 and 1991 runs (see section 1.3.2).

b) χ_1

The χ_1 is in a $J^{PC} = 1^{++}$ state, so both formation helicity amplitudes B_0 and B_1 can be non-zero. However, from charge-conjugation invariance (Eq.2.5), $B_{+\frac{1}{2},+\frac{1}{2}} = \eta_C(-1)^J B_{+\frac{1}{2},+\frac{1}{2}} = -B_{+\frac{1}{2},+\frac{1}{2}} = 0$, and similarly $B_{-\frac{1}{2},-\frac{1}{2}} = -B_{-\frac{1}{2},-\frac{1}{2}} = 0$. Consequently, $B_0^2 \equiv |B_{+\frac{1}{2},+\frac{1}{2}}|^2 + |B_{-\frac{1}{2},-\frac{1}{2}}|^2$ must be equal to zero, and B_1^2 must be equal to one from the normalization condition 2.6.

The spin component of the χ_1 in the J/ψ direction can be 0 or $pm1$, so both A_0 and A_1 can have non-zero values. This corresponds to non-vanishing dipole and quadrupole transition amplitudes, a_1 and a_2. The normalization condition 2.9 leaves one independent parameter in the angular distribution function, chosen conventionally to be a_2.

The angular distribution function has the form

$$W_1(\theta,\theta',\phi') = \frac{9}{64\pi^2}\left(K_1 + K_2 + (K_3 + K_4\cos^2\theta)\cos^2\theta' - K_5\sin 2\theta \sin 2\theta' \cos\phi'\right), \quad (2.11)$$

where

$$\begin{aligned} K_1 &= \frac{1}{2}, \\ K_2 &= \frac{1}{2}(2A_1^2 - 1), \\ K_3 &= \frac{1}{2} - A_1^2, \\ K_4 &= -\frac{1}{2}, \\ \text{and } K_5 &= \frac{1}{4}A_1 A_0. \end{aligned}$$

Fig. 2.3 shows partially integrated angular distributions: $W_1(\theta) \equiv \int\int W_1(\theta,\theta',\phi')d\cos\theta' d\phi'$ and $W_1(\theta') \equiv \int\int W_1(\theta,\theta',\phi')d\cos\theta\, d\phi'$, for several values of the quadrupole amplitude a_2.

$W_1(\phi') \equiv \int\int W_1(\theta, \theta', \phi') d\cos\theta \, d\cos\theta'$ is constant.

c) χ_2

The χ_2 has quantum numbers $J^{PC} = 2^{++}$, so both formation helicity amplitudes B_0 and B_1 can be non-zero. The spin projection in the direction of J/ψ can be 0, ± 1 or ± 2, with corresponding decay helicity amplitudes A_0, A_1 and A_2. In terms of the multipole transitions, all three amplitudes a_1, a_2 and a_3 can have non-zero values. Using the normalization conditions 2.6, 2.9, we are left with three independent parameters, chosen to be B_0^2, a_2, and a_3, which carry information on the dynamics of both the formation process and of the radiative decay.

The angular distribution function can be written as

$$\begin{aligned} W_2(\theta, \theta', \phi') &= \frac{15}{64\pi^2}\Big(K_1 + K_2\cos^2\theta + K_3\cos^4\theta + (K_4 + K_5\cos^2\theta + K_6\cos^4\theta)\cos^2\theta' \\ &\quad + (K_7 + K_8\cos^2\theta + K_9\cos^4\theta)\sin^2\theta'\cos 2\phi' \\ &\quad - (K_{10} + K_{11}\cos^2\theta)\sin 2\theta \sin 2\theta' \cos\phi'\Big), \end{aligned} \tag{2.12}$$

where

$$\begin{aligned} K_1 &= \frac{1}{8}(2A_0^2 + 3A_2^2 - R(2A_0^2 - 4A_1^2 + A_2^2)), \\ K_2 &= \frac{3}{4}(-2A_0^2 + 4A_1^2 - A_2^2 + R(4A_0^2 - 6A_1^2 + A_2^2)), \\ K_3 &= \frac{1}{8}(6A_0^2 - 8A_1^2 + A_2^2)(3 - 5R), \\ K_4 &= \frac{1}{8}(2A_0^2 + 3A_2^2 - R(2A_0^2 + 4A_1^2 + A_2^2)), \\ K_5 &= \frac{3}{4}(-2A_0^2 - 4A_1^2 - A_2^2 + R(4A_0^2 + 6A_1^2 + A_2^2)), \\ K_6 &= \frac{1}{8}(6A_0^2 + 8A_1^2 + A_2^2)(3 - 5R), \\ K_7 &= \frac{\sqrt{6}}{4}(R - 1)A_0A_2, \end{aligned}$$

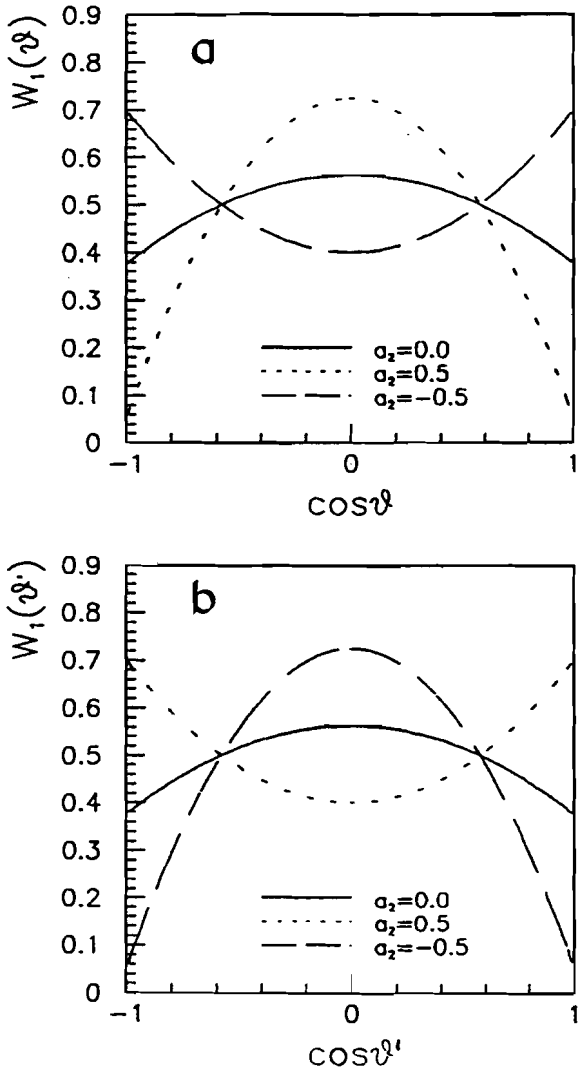

Figure 2.3: Angular distribution function W_1 as a function of (a) $\cos\theta$ and (b) $\cos\theta'$, for several values of a_2.

$$
\begin{aligned}
K_8 &= \frac{\sqrt{6}}{4}(4-6R)A_0A_2, \\
K_9 &= \frac{\sqrt{6}}{4}(5R-3)A_0A_2, \\
K_{10} &= \frac{\sqrt{3}}{4}(A_0A_1+\sqrt{\frac{3}{2}}A_1A_2-R(2A_0A_1+\sqrt{\frac{3}{2}}A_1A_2)), \\
\text{and} \qquad K_{11} &= \frac{1}{4\sqrt{3}}(5R-3)(3A_0A_1+\sqrt{\frac{3}{2}}A_1A_2),
\end{aligned}
$$

and R is defined as

$$R = \frac{2B_1^2}{B_0^2+2B_1^2}. \tag{2.13}$$

Fig. 2.4 shows partially integrated angular distributions $W_2(\theta)$, $W_2(\theta')$ and $W_2(\phi')$, defined analogously as in the case of χ_1, for several values of a_2 and B_0^2. Obviously, only $W_2(\theta)$ depends on B_0^2. For a given value of a_2, the dependence on B_0^2 is rather weak, which indicates that our measurement of B_0^2 will be less accurate than that of a_2.

2.2 Predictions for the angular distribution parameters

2.2.1 Helicity in the annihilation $p\bar{p} \to \chi_2$

a) Helicity selection rule of massless QCD

The simplest prediction for helicity amplitudes in the formation process comes as a consequence of the helicity selection rule of massless QCD [4,57]. The rule states that, for massless quarks, the $q\bar{q}g$ vertex vanishes unless the quark and the antiquark have opposite helicities. (This can be shown using massless helicity spinors $u^{(\lambda)}(k) = \sqrt{E}(1+\gamma_5 2\lambda)\phi^{(\lambda)}(\hat{k})$ and $v^{(\lambda')}(k') = -\sqrt{E}(1-\gamma_5 2\lambda')\chi^{(\lambda')}(\hat{k}')$, and $q\bar{q}g$ vertex $V^\mu = \bar{u}^{(\lambda)}(k)\gamma^\mu v^{(\lambda')}(k')$ [58]). If we assume that in the annihilation process (shown in Fig. 1.5) the proton and antiproton are made of massless, collinear quarks which annihilate in pairs, it follows that the helicities

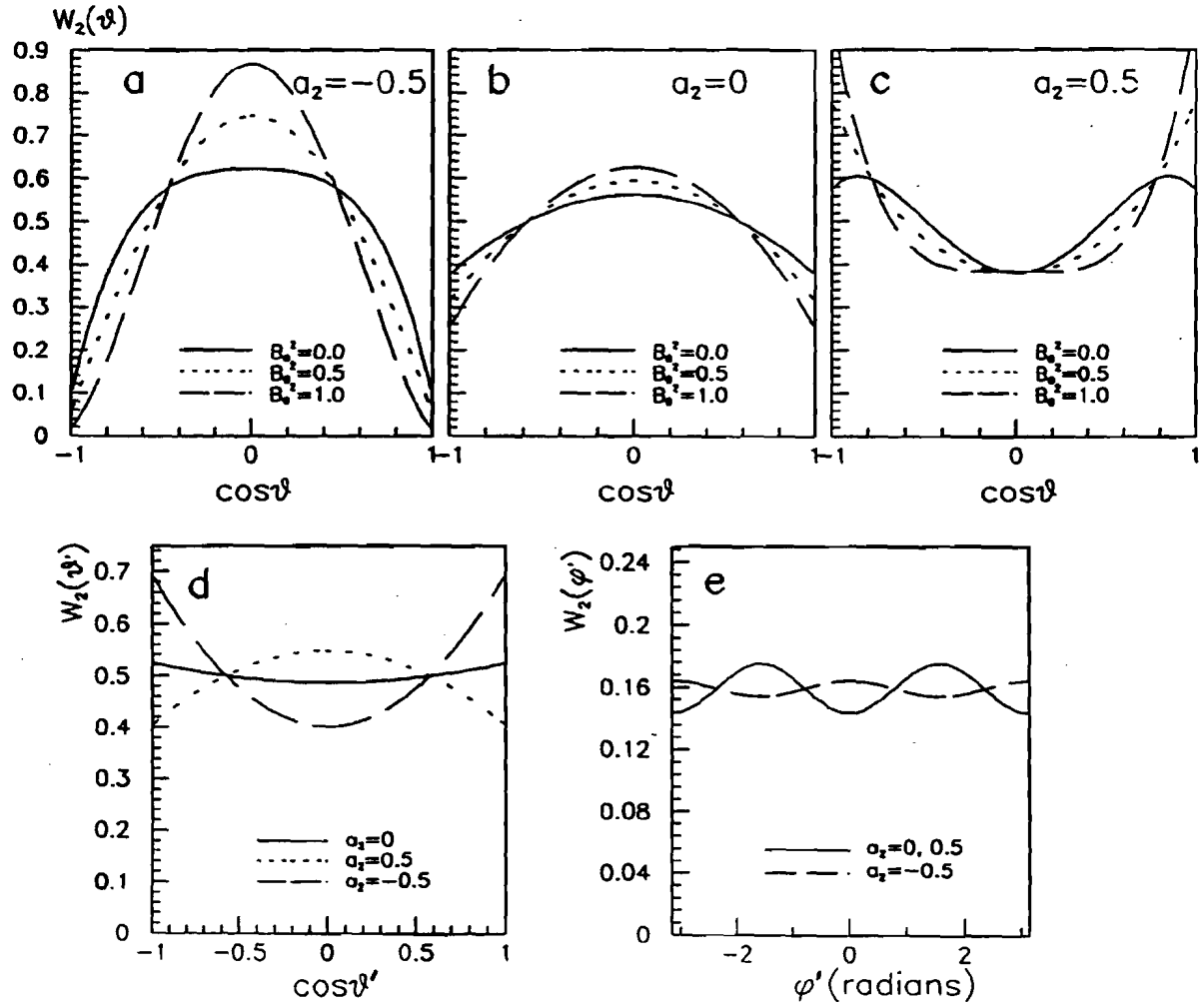

Figure 2.4: Angular distribution function W_2 as a function of (a,b,c) $\cos\theta$, (d) $\cos\theta'$ and (e) ϕ', for several values of a_2 and B_0^2.

of the p and $\bar{p}$ must also be opposite. Thus, $\lambda(\chi_2) = \lambda(\bar{p}) - \lambda(p) = \pm 1$, and

$$2B_1^2 = 1 \qquad \text{and} \qquad B_0^2 = 0. \tag{2.14}$$

This result is a direct consequence of the parton picture of the $p\bar{p}$ annihilation and of the gluon spin.

The vanishing of the helicity zero amplitude in $p\bar{p}$ annihilation puts a constraint on the angular distribution in the reaction $p\bar{p} \to \chi_2 \to J/\psi\,\gamma$. Other consequences of the helicity selection rule include vanishing branching ratios to $p\bar{p}$ of all $J = 0$ charmonium states (η_c, η_c', χ_0), and of the $^1P_1$ state. The latter must be zero because helicity zero is forbidden by Eq. 2.14, and helicities ± 1 are forbidden by parity and C-parity invariance (Eqs. 2.4,2.5).

The helicity selection rule prediction is a good first-order approximation, but it is expected to be violated to some extent, because the assumption that light quarks are massless is not completely justified at charmonium energies. It will be shown in the next section that violation of Eq. 2.14, due to a non-zero quark masses, is of the order of $m_p^2/m_\chi^2 \approx 0.1$, where m_p is the mass of the proton.

Violations of the helicity selection rule in the charmonium system have already been observed in experiments, as non-zero branching ratios BR($\eta_c \to p\bar{p}$) [22] and BR($^1P_1 \to p\bar{p}$) [46]. Another experimental evidence comes from analysis of angular distribution in the reaction $e^+e^- \to J/\psi \to p\bar{p}$ [12], which implies [56] that in the time-reversed process $p\bar{p} \to J/\psi$, B_0^2 is non-zero, $B_0^2(p\bar{p} \to J/\psi) = 0.102 \pm^{0.025}_{0.024}$.

b) Effective lagrangian approach

The contribution of helicity zero in $\bar{p}p$ annihilation due to the non-zero proton mass can be evaluated using the effective lagrangian approach. The interaction of a $J^{PC} = 2^{++}$ field

with a proton and antiproton can be described by the following lagrangian [9, 59]

$$L_{eff} \propto \bar{p}\,(\gamma_\mu \overleftrightarrow{\partial}_\nu + \gamma_\nu \overleftrightarrow{\partial}_\mu + \frac{2}{3}\eta_{\mu\nu}\,\not{\partial})\,p\,T^{\mu\nu}, \tag{2.15}$$

$$\eta_{\mu\nu} = -g_{\mu\nu} + \frac{q_\mu g_\nu}{q^2},$$

where p and $\bar{p}$ are spinors representing the proton and antiproton, and $T^{\mu\nu}$ is a tensor field describing the χ_2. Taking standard tensors t) corresponding to helicity ± 1 and 0 states of the χ_2, and Dirac spinors of mass m_p to describe the proton and antiproton [58], one obtains

$$\frac{B_0^2}{B_1^2} = \frac{16}{3}\left(\frac{m_p}{m_{\chi_2}}\right)^2, \tag{2.16}$$

where B_0^2 is the probability of $p\bar{p}$ annihilation with helicity 0, and $2\,B_1^2$ is the probability of helicity ± 1. Taking into account the normalization condition 2.6, one gets

$$B_0^2 = 0.157. \tag{2.17}$$

Analogous predictions can be made for the reaction $p\bar{p} \to J/\psi$, using $L_{eff} \propto \bar{p}\gamma_\mu p V^\mu$. The result, $\frac{B_0^2}{B_1^2}(p\bar{p} \to J/\psi) = 4(\frac{m_p}{m_{J/\psi}})^2$, or $B_0^2(p\bar{p} \to J/\psi) = 0.155$, is in rough agreement with the experimental result (see section 2.2.1a), while the prediction of massless QCD is in disagreement with that result.

Even though the effective lagrangian approach offers an improvement compared to massless QCD by incorporating a non-zero proton mass, it neglects the quark structure of the proton and the antiproton, treating them as pointlike objects. A more realistic description of $p\bar{p}$ annihilation is discussed in the following section.

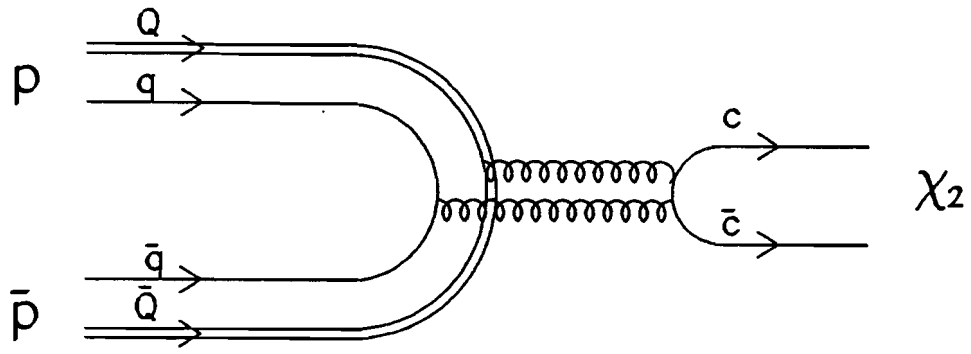

Figure 2.5: Schematic picture of the annihilation $p\bar{p} \to \chi_2$, in the quark-diquark model of the proton (Q stands for a diquark and q for a quark).

c) QCD calculation using quark-diquark model of the proton

The contribution of helicity zero in $p\bar{p} \to \chi_2$ annihilation has also been predicted by a QCD-based calculation, using a quark-diquark model of the proton [60]. In a standard QCD scheme, an exclusive interaction is described by the convolution of a hard elementary process, involving free hadron constituents, with a soft part, the hadronic wave function, which models the hadronization of the constituents into the observed particles. In the quark-diquark model it is assumed that the elementary constituents of the proton are a quark and a diquark (bound state of two quarks); the annihilation process is shown schematically in Fig. 2.5. The quark-diquark model is used in order to model non-perturbative effects, namely sharing of the proton momentum by its constituents; motivation for using this model can be found in Refs. [60, 61] and references therein.

An advantage of the quark-diquark approach, compared to the standard pure quark model, is that the $Q\bar{Q}g$ vertex (where Q stands for diquark) allows a spin flip for massless quarks and diquarks, while the $q\bar{q}g$ vertex does not. Consequently, the coupling of $p\bar{p}$ to $J = 0$ charmonium states (such as η_c and χ_0) is not forbidden, and also the contribution

of helicity zero in $p\bar{p} \to \chi_2$ does not vanish. Alternatively, one could use the standard pure quark approach with massive quarks, which allows spin flip; I am not aware of such a calculation for the helicity zero contribution in $p\bar{p} \to \chi_2$. Other predictions made using the pure quark approach, of the partial widths $\Gamma(\chi_{1,2} \to p\bar{p})$, seem to be more dependent on the proton wave function than the predictions of the quark-diquark scheme [62].

In the calculation of Ref. [60], quarks and diquarks are assigned non-zero (running) masses. The acceptable ranges of the free parameters of the model are determined [62] by comparing the predictions for the widths $\Gamma(\chi_{1,2} \to p\bar{p})$ with experimental results. The contribution of helicity zero in $p\bar{p} \to \chi_2$ is found to be

$$B_0^2 \approx 0.16. \tag{2.18}$$

The prediction is not sensitive to the parameters of the model, including the quark-diquark momentum distribution.

It should be mentioned that while the quark-diquark approach is successful in predicting the widths $\Gamma(\chi_{1,2} \to p\bar{p})$, and allows for the decay $\eta_c \to p\bar{p}$, it fails to predict the rate of that decay: the measured rate is four orders of magnitude larger than the theoretical prediction [62].

2.2.2 Multipolarity in the radiative decays $\chi_{1,2} \to J/\psi\,\gamma$

In the non-relativistic, long-wavelength approximation, the radiative decays $\chi_{1,2} \to J/\psi\,\gamma$ are pure dipole transitions. Higher order multipoles arise as a consequence of relativistic corrections to the interaction of the radiation field with charmonium [5, 37, 63, 64]. The amplitudes corresponding to higher multipoles are of the relative order of v^2/c^2 (or E_γ/m_c, where E_γ is the photon energy), with $v^2/c^2 \approx 0.15$ in charmonium.

The radiative widths $\Gamma(\chi_{1,2} \to J/\psi\gamma)$ receive contributions only of the order of $(v^2/c^2)^2$ from the higher multipoles, because the interference terms (E1 with M2 and with E3), which are proportional to v^2/c^2, cancel out when integrated over all angles. In addition, the widths are sensitive to the nature of the $c\bar{c}$ potential, relativistic corrections, and coupled channel effects[2] [37,38]. On the other hand, the angular distributions depend on higher multipoles at the order v^2/c^2, and they are not sensitive to the potential; thus, the angular distributions are uniquely suited to study the contributions of higher multipoles.

The higher multipole amplitudes in the decays $\chi_J \to J/\psi\gamma$ and $\psi', \psi'' \to \chi_J\gamma$, have been calculated in Ref. [5]. The calculation uses the framework of the potential model of charmonium, and takes into account relativistic effects of the order v^2/c^2. The hamiltonian of the interaction of charmonium with the radiation field, which is a relativistic generalization of the hamiltonian given by Eq. 1.12, is written as

$$\mathcal{H}_{em} = \sum_{j=1}^{2} \frac{ie_c}{2}\left(\vec{A}_j\cdot[\vec{r}_j,\mathcal{H}_0] + [\vec{r}_j,\mathcal{H}_0]\cdot\vec{A}_j - \frac{e_c}{m_c}(1+\kappa_c)\vec{S}_j\cdot\vec{B}_j - \frac{e_c}{2m_c^2}(1+2\kappa_c)\vec{S}_j\cdot(\vec{E}_j\times\vec{p}_j)\right), \tag{2.19}$$

where $\vec{A}_j = \vec{A}(\vec{r}_j,t)$ etc, $\mathcal{H}_0$ is the relativistic hamiltonian of the isolated charmonium system, and e_c, m_c and κ_c are the charge, mass, and anomalous magnetic moment of the charmed quark. Eq. 2.19 includes only those terms which contribute to parity-changing one-photon transitions, to relative order v^2/c^2.

a) $\chi_2 \to J/\psi\gamma$

In the case of the χ_2, the normalized multipole amplitudes are the following

$$a_1 \simeq 1, \tag{2.20}$$

[2]Coupling between charmonium states due to common decay channels to charmed mesons, see Ref. [29] for details.

$$a_2 \simeq -\frac{iE_\gamma}{2m_c}\sqrt{\frac{3}{5}}\frac{\frac{1}{3}\langle\psi\|T_2\|\chi_2\rangle + \frac{i}{\sqrt{2}}(1+\kappa_c)\langle\psi\|S_2\|\chi_2\rangle}{\langle\psi\|X_1\|\chi_2\rangle}, \quad (2.21)$$

and

$$a_3 \simeq -\frac{iE_\gamma}{2m_c}\frac{1}{\sqrt{35}}\frac{\langle\psi\|T_3\|\chi_2\rangle}{\langle\psi\|X_1\|\chi_2\rangle}. \quad (2.22)$$

The reduced matrix elements can be expressed in terms of integrals I_1,..I_4, involving radial wave-functions of the initial and the final charmonium states

$$\begin{aligned}
\langle\psi\|X_1\|\chi_2\rangle &= -\frac{\sqrt{5}}{3}\left(aI_1 - \frac{b}{5\sqrt{2}}I_2\right), \\
\langle\psi\|T_2\|\chi_2\rangle &= -\frac{\sqrt{3}}{2\sqrt{5}}bI_2, \\
\langle\psi\|S_2\|\chi_2\rangle &= \sqrt{\frac{5}{6}}\left(aI_1 + b\frac{\sqrt{2}}{5}I_2\right), \\
\text{and} \quad \langle\psi\|T_3\|\chi_2\rangle &= -\frac{i\sqrt{2}}{5\sqrt{7}}b(3I_4 + 8I_2). \quad (2.23)
\end{aligned}$$

The numerical values of the integrals are given in Table I of Ref. [5]. The coefficients a, b specify the fractions of S- and D-wave in the J/ψ: $|\psi\rangle = a|1^3S_1\rangle + b|1^3D_1\rangle$. The admixture of D-wave is expected to be small: the mixing due to relativistic effects, calculated in first order perturbation theory, is $b = -1.5\%$ [38], and the mixing due to coupled channels is of the order of 10^{-4} [30]). If b is assumed to be zero, expressions 2.21, 2.22 become independent of the matrix elements, and thus independent of the potential:

$$a_2 \simeq -\frac{3}{\sqrt{5}}\frac{E_\gamma}{4m_c}(1+\kappa_c), \quad (2.24)$$

and

$$a_3 \simeq 0. \quad (2.25)$$

The photon energy $E_\gamma = \frac{m_\chi^2 - m_\psi^2}{2m_\chi} = 430$ MeV for χ_2.

The quadrupole amplitude a_2 is sensitive to the charmed quark mass and its magnetic moment. The value of m_c in the literature varies between 1.3 and 1.8 GeV/c^2; the anomalous

magnetic moment will be discussed later. Assuming $m_c = 1.5\ \mathrm{GeV/c^2}$ and $\kappa_c = 0$, one gets $a_2 = -0.096$.

The vanishing of the octupole amplitude a_3 can be explained in terms of the single-quark radiation hypothesis (SQR) [65]. In this hypothesis it is assumed that the photon is emitted by one quark (as opposed to the charmonium as a whole), orbiting around the other spectator quark; this assumption is apparent in the form of the hamiltonian (Eq. 2.19). The total angular momentum of a quark orbiting the χ_2 ($L = 1$) is $J_i = 3/2$; the final angular momentum, of the quark orbiting the J/ψ ($L = 0$) is $J_f = 1/2$. From angular momentum conservation, the multipolarity k is restricted to $J_i + J_f \geq k \geq |J_i - J_f|$, thus the octupole transition is forbidden.

If there is an admixture of D-wave in the J/ψ, the above argument no longer holds. However, using Eqs. 2.22, 2.23, and the values $I_1 = 0.418$, $I_2 = 0.664$, $I_4 = -0.890$ [5], one obtains $a_3 = 0.022 \cdot b$; thus, for $b = -1.5\%$, the octupole amplitude has a negligibly small value of 0.0003.

b) $\chi_1 \rightarrow J/\psi\,\gamma$

In the case of the χ_1 the general formulae for a_1, a_2 are the same as in the case of the χ_2 (Eqs. 2.20, 2.21), with $|\chi_2\rangle$ replaced by $|\chi_1\rangle$ in the reduced matrix elements. The matrix elements are

$$\begin{aligned} \langle \psi \| X_1 \| \chi_1 \rangle &= \frac{1}{\sqrt{3}} \left(a I_1 + \frac{b}{\sqrt{2}} I_2 \right), \\ \langle \psi \| T_2 \| \chi_1 \rangle &= -\frac{3}{2\sqrt{5}} b I_2, \\ \text{and} \qquad \langle \psi \| S_2 \| \chi_1 \rangle &= -\frac{5}{3\sqrt{10}} \left(a I_1 + b \frac{2\sqrt{2}}{5} I_2 \right). \end{aligned} \tag{2.26}$$

As in the case of the χ_2, with the assumption of no D-wave mixing ($b = 0$) the quadrupole amplitude becomes independent of the potential

$$a_2 \simeq -\frac{E_\gamma}{4m_c}(1 + \kappa_c), \tag{2.27}$$

with $E_\gamma = 389\,\mathrm{MeV}$ in the case of the χ_1. Assuming $m_c = 1.5\,\mathrm{GeV/c^2}$ and $\kappa_c = 0$, one obtains $a_2 = -0.065$.

The expressions for $a_2(\chi_2)$ and $a_2(\chi_1)$, given by Eqs. 2.24 and 2.27, coincide with those of Ref. [63], after the helicity amplitudes given in that reference are expressed in terms of the normalized multipole amplitudes.

c) Anomalous magnetic moment of the charmed quark

The quadrupole amplitudes are sensitive to the anomalous magnetic moment of the charmed quark; a short discussion of this topic follows. The anomalous magnetic moment κ measures deviations of the magnetic moment $\vec{\mu}$ from that of a free Dirac particle:

$$\vec{\mu} = \frac{e}{2m}(1 + \kappa)\vec{\sigma}. \tag{2.28}$$

In the case of a quark in a bound system, such deviation can be caused by non-perturbative binding effects, see Ref. [66]. A simple model calculation in this reference, considering fermions confined in a rigid sphere, suggests that the resulting deviations are 20% or less. In Refs. [67] anomalous magnetic moments of light quarks in hadrons, due to higher order QCD corrections, are proposed, in order to explain radiative decay rates of vector mesons, and magnetic moments of baryons. Because of the non-perturbative nature of the anomalous magnetic moments of bound quarks, they cannot be calculated; rather, they have to be determined from experimental measurements.

The anomalous magnetic moment of a charmed quark in charmonium can, in principle, be determined by studying the M1 decays $J/\psi, \psi' \to \eta_c \gamma$. The rates of these decays are sensitive to κ_c; in the non-relativistic limit, the rate for the J/ψ is proportional to the square of the magnetic moment (Eqs. 1.14, 2.28)

$$\Gamma(J/\psi \to \eta_c \gamma) = \frac{16}{3} \left(\frac{e_c}{2m_c}(1+\kappa_c) \right)^2 \alpha {E_\gamma}^3. \tag{2.29}$$

Using the measured value $\Gamma(J/\psi \to \eta_c \gamma) = 1.09 \pm 0.32\,\mathrm{keV}$ [22], $m_c = 1.5 \pm 0.3\,\mathrm{GeV/c^2}$ and $E_\gamma = 0.115\,\mathrm{GeV}$, one obtains $\kappa_c = -0.38 \pm 0.09 \pm 0.10$, where the first error is due to experimental error on the width, and the second corresponds to the uncertainty of m_c. The non-relativistic approach is obviously an over-simplification, as was discussed in section 1.2.3b. A relativistic calculation of the M1 rates for the J/ψ and ψ' is presented in Ref. [38]. Comparing their prediction for the J/ψ with the measured value (assuming a purely scalar confining potential, $\eta_s = 1$), one gets $\kappa_c = -0.01 \pm^{0.08}_{0.10}$, with the error due to the experimental uncertainty of the width. However, in order to explain the measured value of the ψ' width, the model requires a much bigger value of the anomalous magnetic moment, $\kappa_c = -0.80 \pm 0.04$, in contradiction with the previously obtained value. In Ref. [40] it is shown that this problem can be remedied by using a different (non-singular) c-$\bar{c}$ potential. The resulting predictions for both J/ψ and ψ', made with the assumption $\kappa_c = 0$, are in reasonable agreement with experimental values. In summary, it seems that the predictions for the M1 decay rates, especially for the ψ', are very sensitive to other factors, like the choice of potential and coupled channel effects (see Ref. [68]), and cannot be used to reliably determine κ_c. In fact, measurement of κ_c from another process would offer a useful constraint for these calculations. The E1 decay rates ($\psi' \to \chi_J \gamma$ and $\chi_J \to J/\psi \gamma$) also receive corrections due to the anomalous magnetic moment [37, 38, 63], but these corrections are much smaller than in the case of the M1 transitions.

Chapter 3

E-760 experimental setup

In order to study charmonium states formed in $p\bar{p}$ annihilation, the Fermilab experiment E-760 used the $\bar{p}$ beam circulating in the Antiproton Accumulator, colliding with a hydrogen gas jet target. Interactions were recorded with a detector optimized for detection of electromagnetic decays of charmonium states. This chapter describes the E-760 beam, target, detector, trigger and data acquisition system.

3.1 The antiproton beam

For a precision study of the charmonium spectrum in the $p\bar{p}$ annihilation, the antiproton beam has to meet the following requirements:

1. The beam energy E_b must be adjustable between 3.8 and 7.1 GeV (total energy), in order to be able to reach all charmonium states of interest;

2. The beam momentum spread (or center-of-mass energy spread) must be very small, in order to measure masses and widths of narrow charmonium states like J/ψ, ψ', χ_1, and χ_2;

3. High $\bar{p}$ beam currents are needed, in order to achieve the high luminosities needed to detect signals of the order of several picobarns (e.g. $^1P_1$, η_c, and η_c').

These requirements are satisfied by the antiproton beam of the Fermilab antiproton source [48,49,69–71]. The antiproton source was originally designed to accumulate and

cool[1] antiprotons, at $E_b = 8.8\,\mathrm{GeV}$, for the Tevatron colliding beam program. For E-760, the antiproton Accumulator was used in a different mode, because the beam had to be decelerated. The operation of the $\bar{p}$ source for E-760, and the beam characteristics, are briefly described below. The beam parameters quoted come from Refs. [48,49], unless otherwise specified.

Fig. 3.1 shows the location of the $\bar{p}$ source (consisting of the Debuncher and the Accumulator rings), and of the E-760 experimental area in the Fermilab machine complex. The antiprotons were produced by bombarding a copper target with 120 GeV protons, accelerated in the Main Ring. Antiprotons of total energy of $\sim 8.8\,\mathrm{GeV}$ were collected, with a typical yield of 1 antiproton per 10^5 incident protons, and transported to the Debuncher ring, where the large momentum spread of the beam was reduced. The antiprotons were then injected into the Accumulator ring, where the beam was continuously accumulated and cooled. The antiproton accumulation (or stacking) rate was $\sim\ 10^{10}\ \bar{p}$/hour. At the end of the stacking process, there were typically 3.5×10^{11} antiprotons circulating in the Accumulator. At that time, the beam was decelerated to the desired energy, at a rate of $\sim\ 20\,\mathrm{MeV/s}$. After deceleration, the beam was cooled again, then the gas jet target was turned on and data taking began. Table A.1 in the Appendix shows beam energies corresponding to the masses of charmonium states.

Stochastic cooling of the beam [69,72] was essential for the success of the experiment. It counteracted the growth of beam emittance[2] and the loss of beam energy resulting from repeated traversal of the gas jet target, and reduced the beam energy spread. The achieved momentum spread of the beam was $\Delta p_b/p_b \approx 2 \times 10^{-4}$ (r.m.s.), which corresponds to a center-of-mass energy spread $\Delta E_{cm} = \frac{m_p c^2}{E_{cm}} \Delta E_b$ of 220 keV at the η_c energy, and 310 keV at the ψ' energy.

[1] Reduce momentum and energy spread of the beam.

[2] Emittance is a measure of transverse momentum spread of a beam.

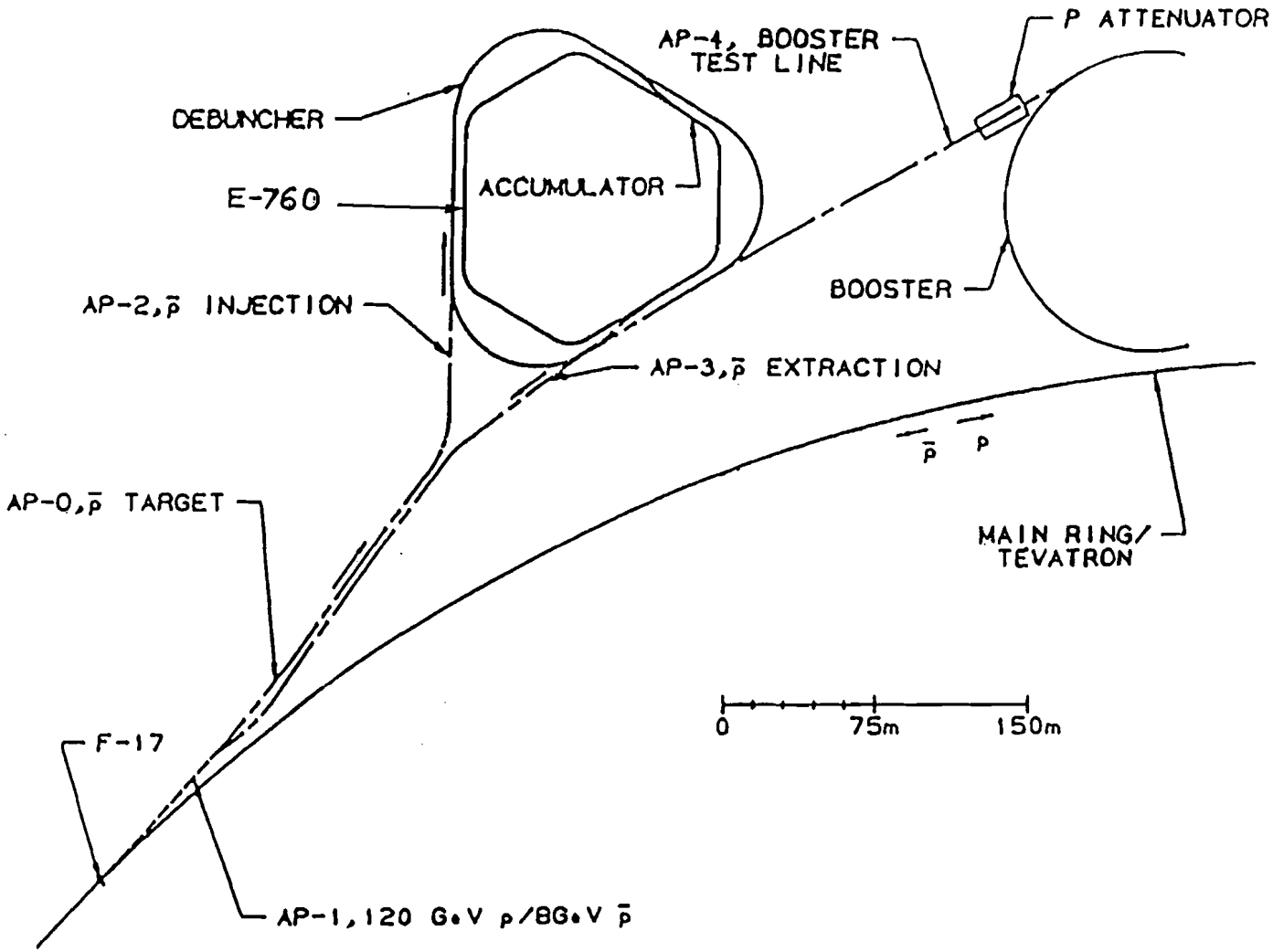

Figure 3.1: Location of the $\bar{p}$ source and the E-760 in the Fermilab machine complex.

The beam had a diameter of $\sim 5mm$ (for 95% containment), and it traversed the gas jet target with a frequency of 0.61-0.63 MHz. The lifetime of the beam was 50-90 hours when the gas jet target was on. Each stack was used for 1-2 lifetimes; then the remainder of the beam was discarded, and accumulation of a new stack begun.

3.2 The hydrogen gas jet target

The E-760 target consisted of a continuously flowing H_2 gas jet, crossing the antiproton beam at 90°. The instantaneous luminosity L, which determines the number of $p\bar{p}$ interactions in unit time ($N_{int} = L \cdot \sigma_{tot}$, where σ_{tot} is the total $p\bar{p}$ cross-section), can be expressed as

$$L = N_p \cdot f_r \cdot \rho, \tag{3.1}$$

where N_p is the number of circulating antiprotons, f_r is their revolution frequency, and ρ is the thickness of the target traversed by the antiprotons (in units of atoms/cm^2). The optimal thickness of the target is 10^{13}-10^{14} atoms/cm^2: a much thicker target would perturb the beam too much, while a thinner one would lead to an unacceptably low luminosity.

A target with the required density and appropriate geometry was built using the technique of molecular cluster jet beams [73]. In the expansion of a gas from high pressure and low temperature through a nozzle of special geometry and very small aperture (30 μm), a flux of large clusters of H_2 molecules is created. These are moving at supersonic speeds, hence the name "jet".

The target system used by E-760 was similar in design and performance to that of the R704 experiment [44]. The gas expansion took place at typical operating conditions of $P_0 = 10$ bar and $T_0 = 77$°K [45]. A system of collimators selected the central, denser part of the jet which, after crossing the Accumulator ring, was absorbed by the sink pumps. In

order to limit the increase of pressure in the Accumulator vacuum pipe, both the expansion and the sink chambers were separated from the vacuum pipe by several pumping stages.

The density of the target was $\sim 5 \times 10^{13}$ atoms/cm^2 [47], and the peak luminosities obtained were $\sim 9 \times 10^{30}$cm^{-2}s^{-1}. The density of the target could be adjusted during data taking, in order to maximize the time-integrated luminosity

$$L_{int} = \int L(t)\, dt, \tag{3.2}$$

which depends on both the target density and on the antiproton beam lifetime.

The transverse size of the interaction region was determined by the beam size (~ 5 mm), and the longitudinal size by the thickness of the H_2 jet (~ 6 mm). A point-like interaction region was fundamental for simplifying the design of the detector, and it facilitated event reconstruction.

3.3 The E-760 detector

The E-760 detector was a large acceptance, high-resolution, non-magnetic spectrometer. It was designed to select electromagnetic final states (such as large invariant mass e^+e^-, $e^+e^-\gamma$, $\gamma\gamma$, and multi-γ states) from a very large hadronic background.

The detector, shown in Fig. 3.2, had cylindrical symmetry around the beam pipe. It covered the complete azimuth, and the laboratory polar angle θ_{lab} from 2° to 70°. In addition, there was the luminosity monitor detector, which covered 2° in azimuth and the θ_{lab} range from 80° to 92°.

The main detector consisted of a central part, which covered the θ_{lab} range from 10° to 70°, and of a forward part, which extended the θ_{lab} coverage down to 2°. The central part included the following detectors (arranged in cylindrical layers, from the beam pipe out)

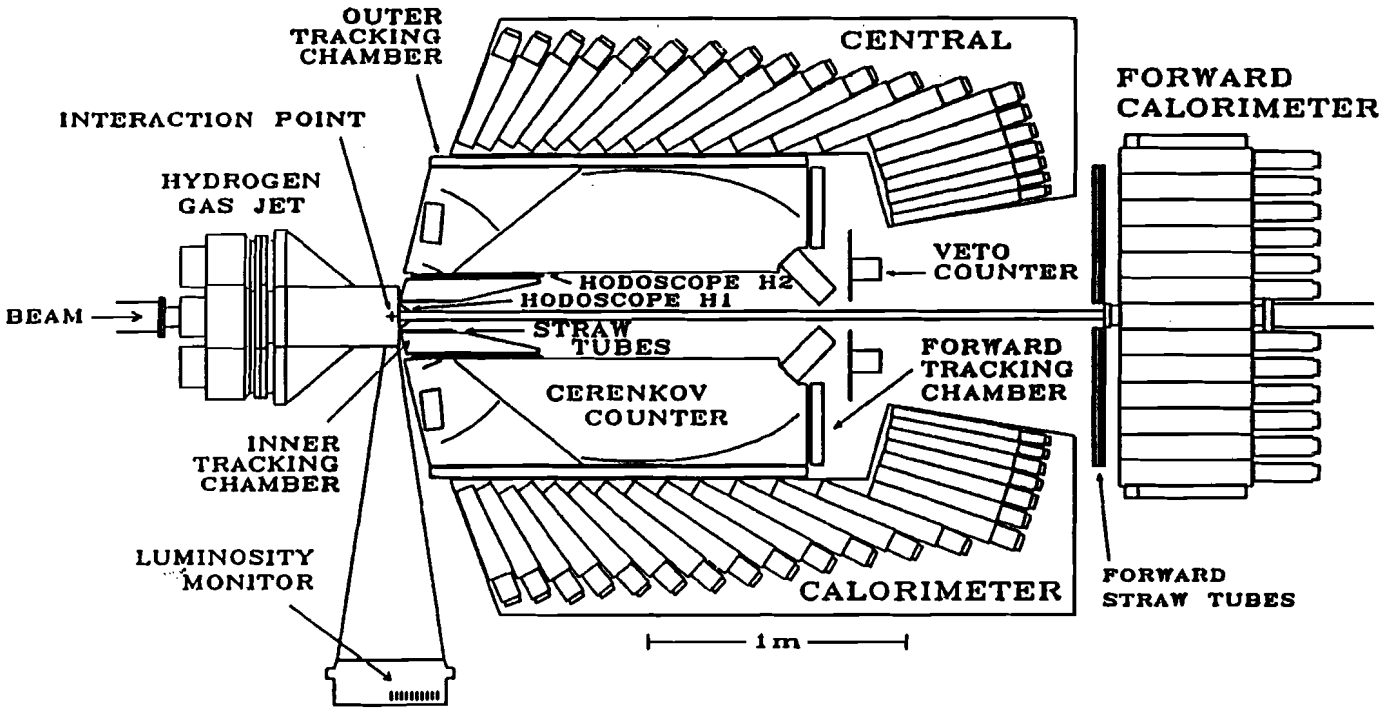

Figure 3.2: Layout of the E-760 detector.

a) the scintillator hodoscope H1,

b) the inner straw tube chamber,

c) the inner tracking chamber,

d) the scintillator hodoscope H2,

e) the threshold Cherenkov counter,

f) the outer tracking chambers,

g) the central electromagnetic calorimeter (CCAL).

The forward part consisted of the following detectors (placed perpendicularly to the beam pipe)

h) the forward veto counter,

i) the forward straw tube chamber,

j) the forward electromagnetic calorimeter (FCAL).

The hodoscopes and the veto counter were used to identify charged particles, the Cherenkov counter provided electron/hadron discrimination, the tracking chambers (this term includes also the straw chambers) provided measurement of charged particle trajectories, and the calorimeters measured the energy and direction of electrons and photons. Additionally, all the detectors, except for the tracking chambers, were used for trigger purposes.

In the following sections, the design and performance of these detectors is described in detail.

3.3.1 The hodoscopes H1 and H2 and the forward veto counter

The scintillator hodoscope H1 was the closest detector to the interaction point. It consisted of 8 azimuthal elements, surrounding the beam pipe. The second scintillator hodoscope H2 was placed at a radius of 17 cm from the beam line, and consisted of 32 azimuthal elements. The light from both H1 and H2 was collected by lightguides and detected by photomultipliers. Since the light yield of H2 was good (average of 50-100 photoelectrons per minimum ionizing particle [48]), the pulse height was also used to distinguish single charged particles from close e^+e^- pairs originating from Dalitz decays or from photon conversions.

The forward veto counter was placed 178 cm downstream from the interaction point. It had an approximately annular shape, with an inner radius of 3.8 cm and an outer radius of 38 cm, and consisted of 8 azimuthal scintillators. The light was collected by phototubes attached directly to the counter surface.

3.3.2 The Cherenkov counter

The Cherenkov counter [74] was placed immediately outside the H2 hodoscope. It was divided into two separate, gas tight sections, covering θ_{lab} regions from 15° to 38° and from 38° to 70° respectively. Each cell was divided into 8 azimuthal sections.

The small-angle section was filled with CO_2, and the large-angle section with Freon-13, at atmospheric pressure and room temperature. As a result of this design, the hadron momentum threshold for Cherenkov radiation was above the maximum possible hadron momentum in the entire θ_{lab} range covered by the counter.

Light collection was simplified by the small size of the interaction region. Light was focused on the windows of photomultipliers by elipsoidal mirrors in the small angle section, and by an arrangement of spherical and flat mirrors in the large angle section.

The light yield was 4-16 photoelectrons in the small angle section, and 6-10 photoelectrons in the large angle section. The Cherenkov discriminator threshold was set at 0.5 photoelectrons, in order to maximize efficiency for electrons. Outside of the region of the partition, separating the two gas tight sections, the efficiency was found to be 99.8%. In the partition region (θ_{lab} from 33° to 39°) the efficiency varied between 60% and 80%, depending on θ_{lab} [75]. The inefficiency was due in part to shadowing from the partition, which covered larger than expected θ_{lab} range because the detector was placed $\sim$ 1 cm downstream from the nominal position, and in part to poor quality of two mirrors in the partition region.

The electron/hadron discrimination power was studied using clean samples of charged pion and proton tracks. It was found that approximately 1% of hadrons were associated with a Cherenkov signal above the discriminator threshold.

3.3.3 The tracking chambers

The inner straw tube chamber [76] was the innermost tracking detector, located just outside of the H1 hodoscope. It consisted of two cylindrical layers of aluminized mylar tubes (*straws*), approximately 10 mm in diameter. The azimuthal angle information was obtained by drift time measurement, and the longitudinal coordinate[3] was determined by charge division on the resistive anode wires.

The inner tracking chamber occupied the space between the inner straw chamber and the hodoscope H2. It consisted of two detectors: the radial projection chamber (RPC) on the inside, and the multiwire proportional chamber (MWPC) [77]. The RPC provided measurements of 3-dimensional particle trajectories, measuring the azimuthal and radial coordinates using wire number and drift time, and the longitudinal coordinates using charge

[3]The asimuthal and longitudnal coordinates refer to the frame in which the Z axis is along the beam direction.

division along resistive sense wires. Additionally, it provided measurements of the charged particle energy loss, which was used to distinguish single electrons from close e^+e^- pairs. The digital readout of the MWPC wires allowed the resolution of the left-right ambiguity in drift time RPC measurements, and the analog cathode readout improved resolution of the longitudinal coordinate measurement.

The outer tracking chambers [78] included two detectors: the cylindrical limited streamer tube (LST) chamber, and the forward tracking chamber (FTC). The LST barrel occupied the space between the Cherenkov counter and the CCAL; the FTC was a planar, annular multiwire proportional chamber, placed perpendicularly to the beam pipe, 170 cm downstream from the interaction point. The outer tracking chambers provided azimuthal and polar angle measurement for charged particles.

The forward straw tube chamber was placed 321 cm downstream from the interaction point, in front of the FCAL. It consisted of four octagonal planes of straw tubes (10 mm diameter), and provided position measurement for charged particles in the forward direction.

The overall angular resolution of the tracking system in the central part was $\Delta\theta_{lab} \approx$ 4 mrad and $\Delta\phi_{lab} \approx 7$ mrad (r.m.s.) [47].

3.3.4 The calorimeters

a) The central calorimeter (CCAL)

The central electromagnetic calorimeter [79] covered full azimuth and the θ_{lab} range from 10.6° to 70°. It consisted of 1280 lead glass (F2) blocks, each pointing to the interaction region. The blocks were arranged in 64 identical sections in ϕ_{lab} (*wedges*), and in 20 polar *rings*. Each block covered 5.625° in ϕ_{lab} and between 1.1° and 5.2° in θ_{lab}. The length of blocks varied from 38 cm to 50 cm, which corresponds to 12–15.9 radiation lengths, and the distance from the interaction region to the face of a block varied from 72 cm to 197 cm.

The blocks were tightly packed together, and were separated by thin stainless steel supports (*cracks*). The cracks in the ϕ_{lab} direction were 1.52 mm thick, and those in the θ_{lab} direction were 0.25 m m thick. Light from the blocks was collected by the photomultipliers glued to the back surface of the blocks, and the output from the phototubes was digitized in 11-bit ADC's.

In addition to using individual signals, the blocks were grouped in 40 segments of 5×8 blocks, forming a coarse θ_{lab}-ϕ_{lab} grid. The signals within each group were summed, and used in the fast trigger logic [80] (section 3.4.1). The summed signals were also used to classify the CCAL signals as *on-time* and *out-of-time* with respect to the trigger [81]. This was accomplished by additionally recording the summed signals with a delay of $\sim$ 100 ns, and comparing magnitudes of delayed and un-delayed signals. The method worked reliably for energy deposits greater than 200 MeV.

During the 1991 run the CCAL calibration constants[4] were determined using a large number of $p\bar{p} \rightarrow \pi^0\pi^0 \rightarrow \gamma\gamma\gamma\gamma$ events. For each event, photon energies can be predicted using their measured directions; the calibration constants were adjusted so that the average difference between measured and observed energies was minimized. The calibration constants were updated approximately once per stack, to reflect their change in time. During the 1990 run, the $\pi^0\pi^0$ events could not be used for calibration purposes, because of improper timing of the *neutral* trigger (see section 3.4), through which these events were accepted. Instead, the calibration constants were determined using the $p\bar{p} \rightarrow J/\psi \rightarrow e^+e^-$ events. The number of these events was much smaller than the number of $\pi^0\pi^0$ events, since they required special data taking at $E_{cm} = m_{J/\psi}c^2$, while the latter were produced at any value of E_{cm}. Consequently, the calibration constants during the 1990 run were less accurate, and the effective 1990 energy resolution of the CCAL was worse than during the 1991 run.

The effect of the steel cracks on the CCAL performance was studied during the CCAL

[4] Proportionality constants between ADC counts and energy units.

tests at BNL [79], and also using the E-760 data. Energy loss in the vicinity of the cracks was parametrized as $\Delta E/E = A\exp(-d/\lambda)$, where d is the track distance from a crack, $\lambda \approx 0.42$ cm and $A \approx 16.1\%$ (for the cracks in ϕ_{lab} direction). Corrections for this effect were made in the off-line analysis program. The cracks also caused deterioration of energy and position resolution in their vicinity, which was taken into account in the off-line resolution parametrization.

Energy and position resolution were studied using a sample of $\sim$4000 $p\bar{p}\rightarrow J/\psi\rightarrow e^+e^-$ events. The effective energy resolution (r.m.s.) was parametrized as

$$\Delta E/E = 5\%/\sqrt{E\,[\mathrm{GeV}]} + 0.5\% + 30\%\,(f_{cor} - 1) \tag{3.3}$$

for the 1991 run, and

$$\Delta E/E = 5\%/\sqrt{E\,[\mathrm{GeV}]} + 3.0\% + 30\%\,(f_{cor} - 1) \tag{3.4}$$

for the 1990 run. The higher value of the second term for the 1990 run is due to less accurate calibration. The third term is due to the cracks (f_{cor} is the crack correction factor for the energy), and is important only for the tracks hitting within 1 cm from a crack. The position resolution (r.m.s.) was parametrized as follows

$$\Delta\theta_{lab}\,[\mathrm{mrad}] = (3.7 + 1.6\,d_\theta)\frac{126.5}{R}, \tag{3.5}$$

$$\Delta\phi_{lab}\,[\mathrm{mrad}] = (5.9 + 2.6\,d_\phi)\frac{78.7}{R\sin\theta_{lab}}, \tag{3.6}$$

where d_θ, d_ϕ are distances (in cm) of the track from the nearest crack along the θ_{lab}, ϕ_{lab} directions respectively, and R is the distance (in cm) of the shower center of gravity from the interaction point. The spatial resolution averaged over the CCAL surface was

$\langle \Delta\theta_{lab} \rangle \approx 5$ mrad, and $\langle \Delta\phi_{lab} \rangle \approx 8$ mrad.

b) The forward calorimeter (FCAL)

The forward calorimeter [82] was a sampling electromagnetic calorimeter. It was placed 340 cm downstream from the interaction point, and extended the θ_{lab} coverage of the E-760 detector down to $\sim 2°$. It consisted of 144 rectangular modules, arranged in a 13×13 array, with 6 modules removed in each array corner, and one center module removed in order to allow for the beam pipe. Each module consisted of 148 alternating layers of lead and scintillator plates. The transverse dimensions of modules were 10×10 cm^2, and module length was 48.4 cm, corresponding to 14.2 radiation lengths. The light from each module was collected by a wavelength-shifter bar placed on one side of the lead-scintillator stack, through a light guide, to a photomultiplier.

In addition to using individual signals, the FCAL modules were grouped into 6 segments (24 modules each), and the summed signals from the segments were used for trigger purposes. The summed signals were also read out by a TDC, providing timing information for FCAL energy deposits. (This feature was implemented only in 1991.)

The FCAL calibration constants were determined using signals from cosmic ray muons, passing vertically through the calorimeter. (Muons deposit a constant, on average, amount of energy per unit path length.) In 1990, such events were collected during special FCAL cosmic runs between the E-760 stacks; in 1991, the FCAL cosmic trigger was implemented as a part of the general trigger, and the cosmic events were collected continuously during the E-760 data taking. The calibration constants were updated on a weekly basis; this was necessary in order to account for observed photomultiplier gain changes with the luminosity.

The performance of the FCAL was studied using photons from several reactions, including $p\bar{p} \to \chi_J \to J/\psi\,\gamma \to e^+e^-\gamma$, and $p\bar{p} \to \pi^0\eta \to \gamma\gamma\gamma\gamma$, as well as EGS4 Monte Carlo simulator of electromagnetic showers [83]. It was found that the response of the FCAL blocks varied

(up to 20%) as a function of the distance of a hit from the wavelength-shifter bar, because of attenuation of light in the scintillator plates. Corrections for this effect were implemented in the off-line analysis program.

The effective FCAL energy resolution was found to be

$$\Delta E/E \approx 19\%/\sqrt{E\,[\mathrm{GeV}]}, \tag{3.7}$$

and the position resolution

$$\Delta x \approx \Delta y \approx 3\,\mathrm{cm}, \tag{3.8}$$

where x and y are cartesian coordinates in the plane perpendicular to the beam direction.

3.3.5 The luminosity monitor

The luminosity monitor [84] was mounted approximately 1.5 m below the interaction point, and consisted of a $1 \times 5\,\mathrm{cm}^2$ and 0.5 mm deep silicon detector. It detected recoil protons elastically scattered at θ_{lab}=86.5°. The integrated luminosity was determined by normalizing the recoil counts to the known $p\bar{p}$ elastic scattering cross section,

$$L_{int} = N_{elastic} / \left(\frac{d\sigma_{elastic}}{d\Omega} d\Omega \right), \tag{3.9}$$

where $d\Omega$ is the solid angle subtended by the silicon detector. The ±4% uncertainty in the integrated luminosity measurement was due mainly to the uncertainties in the elastic cross section and in the solid angle $d\Omega$.

3.4 Trigger and data acquisition

This experiment was designed to look for two kinds of charmonium decays: decays with a high invariant mass e^+e^- pair in the final state (e.g. reactions 1.18, 1.21), and exclusive decays to two or more photons (e.g. 1.17, 1.26). A trigger designed for detection of e^+e^- pairs (so called *charged* trigger), and a trigger for the neutral final states (*neutral* trigger), were used in parallel during the data taking. The data analysed in this thesis come from the *charged* trigger, which is described below. (Description of the *neutral* trigger can be found in Ref. [50].)

3.4.1 Charged trigger

The exclusive e^+e^- final state has a simple signature of two electron tracks satisfying 2-body decay kinematics; in the inclusive decays of charmonium states to $J/\psi \rightarrow e^+e^-$, the J/ψ carries a significant fraction of the $\bar{p}$ momentum, and the 2-body kinematical correlation of the e^+e^- pair is only slightly distorted. Thus, the *charged* trigger required two high energy, approximately back-to-back electrons, defined by signals in the Cherenkov, hodoscopes H1 and H2, and the CCAL. In addition, in order to cover the region where the Cherenkov was inefficient, and to study the efficiency of the CCAL component of the trigger, three other triggers with relaxed Cherenkov or CCAL requirements were run simultaneously. Thus, the *charged* trigger was a logical OR of four subtriggers (called *2-,1-,0-Cherenkov,* and *no-CCAL* respectively), and was defined as follows

$$
\begin{array}{llllllll}
 & (PBG1 & \otimes\ ee & \otimes\ nH1{\leq}4 & \otimes\ nH2{\leq}4) & & & 2\text{-}Cher \\
\oplus & (PBG1 & \otimes\ ehh & \otimes\ nH1{=}2 & \otimes\ nH2{\leq}2 & \otimes\ copl) & & 1\text{-}Cher \\
\oplus & (PBG1 & \otimes\ hh & \otimes\ nH1{=}2 & \otimes\ nH2{\leq}2 & \otimes\ copl \otimes \overline{FCH}) & & 0\text{-}Cher \\
\oplus & & (ee & \otimes\ nH1{=}2 & \otimes\ nH2{\leq}2) & & & no\text{-}CCAL
\end{array}
$$

where

$\otimes$,$\oplus$ denote logical AND and OR operations respectively;

$PBG1$ denotes two coincident signals in the CCAL 5×8 block segments, above a θ_{lab}-dependent energy threshold, and separated in ϕ_{lab} by more than 90°;

e denotes an electron track, defined by a coincidence of signals from H1, H2 and Cherenkov modules overlapping in ϕ_{lab};

h denotes a charged track, defined similarly to the electron track, but without the Cherenkov requirement;

$nH1,2$ denote hit multiplicities in the H1 and H2 hodoscopes;

copl (coplanarity) denotes the requirement that the two H2 hits be separated in ϕ_{lab} by 16 ± 1 hodoscope elements;

$\overline{FCH}$ denotes the requirement of no signal in the forward veto counter.

The thresholds for the PBG1 were determined from the event kinematics [80]. Fig. A.2 in the Appendix shows energy of electrons from the decay $\chi_{1,2} \rightarrow J/\psi\,\gamma \rightarrow e^+e^-\gamma$ as a function of θ_{lab} (from a Monte Carlo simulation). For each of the five θ_{lab} regions, corresponding to the θ_{lab}-ϕ_{lab} summer grid, the thresholds were set at 70% of the lowest kinematically allowed electron energy in that region.

3.4.2 Data acquisition

The data were read from CAMAC using the Fermilab Smart Crate Controller system [85] and the ACP microprocessor farm [86]. The events were then transferred to the *Front-End* MicroVAX II, and written to magnetic tapes.

The hardware trigger rates for the *charged* trigger were less than 25 Hz, which was low enough to write all events to tape. For the *neutral* trigger, the rates were as high as 800 Hz at peak luminosity, and it was necessary to use a second-level ACP trigger, in order to reduce rates to manageable level.

In addition to writing events to tape, the *Front-End* VAX was continuously sending a fraction of events to the *Monitor* MicroVAX II. These events were used as input to an on-line program which monitored performance of the detectors, and to the on-line event-display program. An example of the event display, for the $\chi_2 \rightarrow J/\psi\,\gamma \rightarrow e^+e^-\gamma$ reaction, is shown in Figs. 3.3 and 3.4.

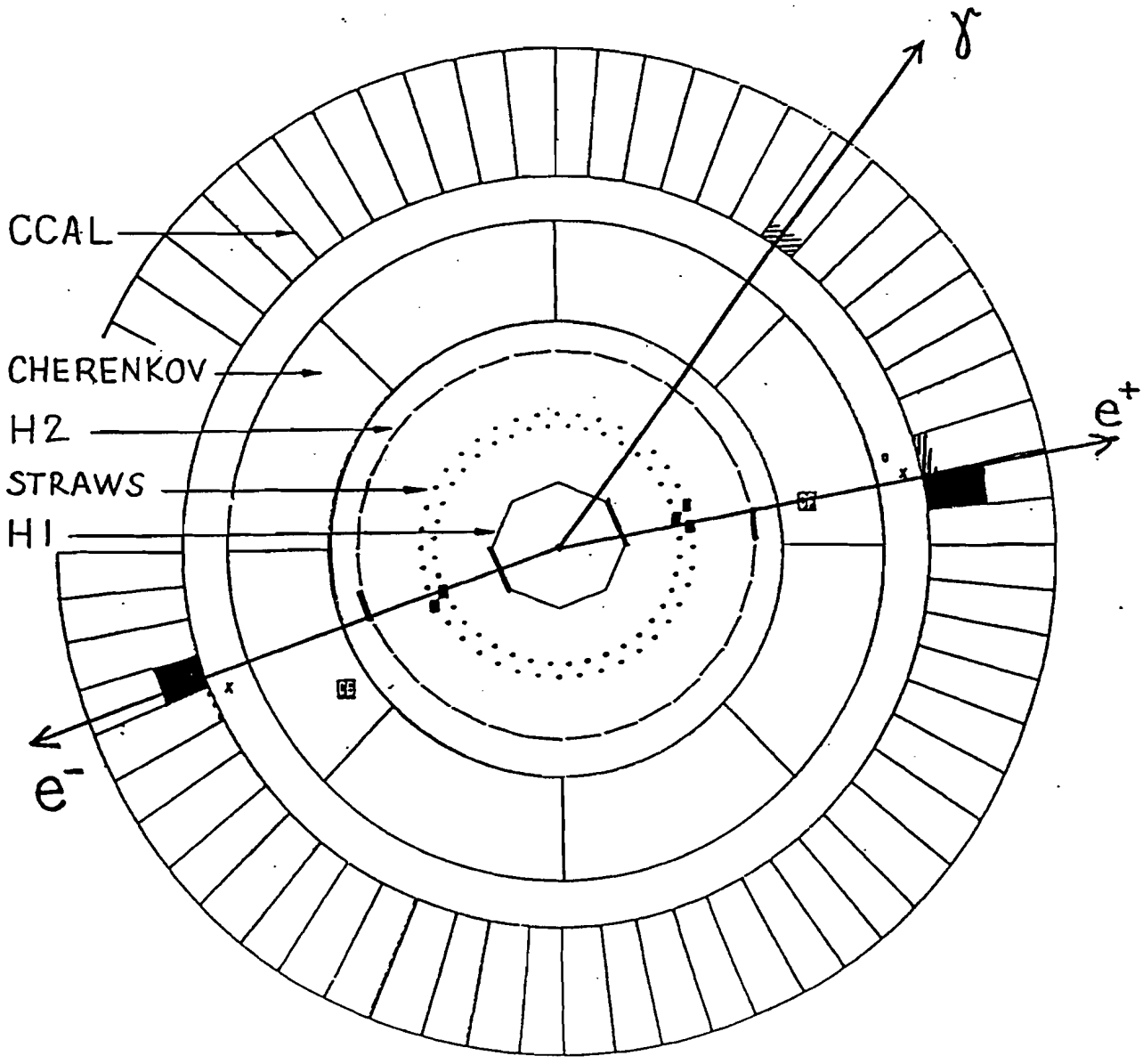

Figure 3.3: A typical $\chi_2 \rightarrow J/\psi\gamma \rightarrow e^+e^-\gamma$ event, seen on the E-760 event display: cross section through the detector in the plane perpendicular to the beam direction (not to scale).

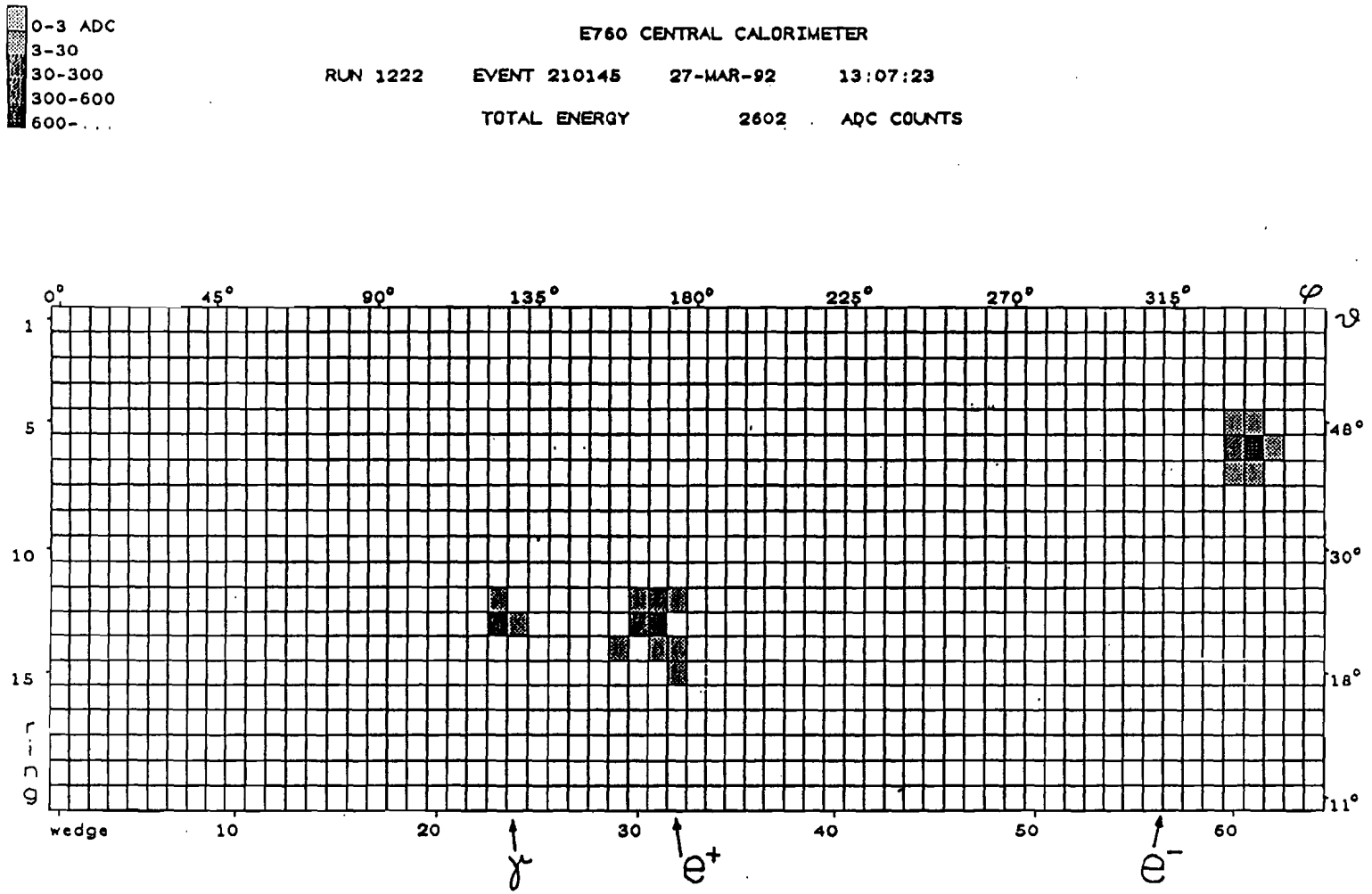

Figure 3.4: A typical $\chi_2 \rightarrow J/\psi\gamma \rightarrow e^+e^-\gamma$ event, seen on the E-760 event display: an unfolded view of the CCAL. The grid shows CCAL blocks (not to scale), and the shading shows energy deposits.

Chapter 4

Data analysis

This chapter describes the analysis which was done to to extract angular distribution parameters from the data. The first section (4.1) explains the preliminary off-line analysis and DST-making process. This part of the analysis was common to all E-760 studies involving charmonium states decaying into J/ψ (reactions 1.18, 1.21, 1.22, 1.24, 1.25, 1.27, 1.28). The remainder of this chapter is devoted to the particular analysis of the angular distributions in the reactions

$$p\bar{p} \rightarrow \chi_{1,2} \rightarrow J/\psi\gamma \rightarrow e^+e^-\gamma. \tag{4.1}$$

In section 4.2 I discuss kinematic fitting and how it is used in the event selection. Determination of the angles which define kinematics of each event is described in section 4.3. Raw and acceptance corrected angular distributions are presented in section 4.4, and some qualitative conclusions about the values of angular distribution parameters are made. The maximum likelihood method used to determine the parameters is described in section 4.5. In section 4.6 sources of systematic errors are discussed, and modifications to the likelihood function and to the data sample in order to reduce these errors are described.

4.1 Preliminary data analysis

4.1.1 Data summary

Table 4.1 shows a summary of the data used in the analysis of the angular distributions. In addition to the χ_1 and χ_2 data, I have listed the data which were used to estimate background levels.

In the 1990 run, the χ_1 and χ_2 data were collected not only to study the angular distributions, but also to measure masses and widths of the $\chi_{1,2}$ states [47]. The beam energy was changed in small steps (energy scan) in order to measure the cross-section as a function of center-of-mass energy E_{cm}. This is the reason for listing an energy range in Tab. 4.1, instead of a single value. In the 1991 run, the χ_2 data were collected at E_{cm} corresponding to the peak cross-section. (During the first stack a mini-scan was performed in order to find the cross-section peak). The 1991 background data were also collected at several energies, and were primarily used to search for structures in the cross-section corresponding to the $^1P_1$ [46] and η_c' charmonium states.

4.1.2 Preliminary off-line analysis and DST's

The goal of the preliminary off-line analysis was to convert electronic detector signals into particle momenta and energies, and to reduce the number of events for the final analysis, based on event characteristics. Events selected in this process were written to Data Summary Tapes (DST's).

The process of converting electronic signals to particle tracks consisted of the following steps:

1. decoding CAMAC module and channel number into detector channel number;

Table 4.1: Summary of data used for analysis of angular distributions.

year	resonance	stack	E_{cm} [MeV]	integrated luminosity [nb^{-1}]
1991	χ_2	1	3555-3557	797
		2	3556	706
		3	3556	1072
				total **2576**
	background ($^1P_1$ search)	1-16	3522-3526	15860
	background (η_c' search)	1-6	3591-3621	5945
1990	χ_1	1	3509-3512	526
		2	3510	99
		3	3509-3511	401
				total **1026**
	χ_2	1	3556	63
		2	3554-3564	398
		3	3554-3558	619
		4	3557	80
				total **1159**
	background ($^1P_1$ search)	1-4	3524	1262

2. pedestal subtraction;

3. signal calibration/normalization;

4. calorimeter cluster finding and energy corrections (e.g. for energy lost in CCAL cracks);

5. transformation of hit and cluster coordinates from detector reference frames to a common laboratory frame;

6. charged track finding (combining hits from charged-particle detectors); and

7. association of charged tracks with calorimeter clusters.

The DST's were made in three levels. The first-level DST selection was based on the trigger type, separating *charged* trigger events from *neutral* and other trigger types. The second-level selection relied on event kinematics, and the requirements were slightly different for the 1990 and 1991 data. For the 1990 data, the selection required a pair of CCAL clusters (found by the ACP software) with an invariant mass equal to the J/ψ mass $\pm 15\%$. In order to assure full efficiency of the selection, events were also accepted if the total energy was greater than 1/2 of the total available energy and the number of CCAL and FCAL clusters was ≤ 4, or if there were two charged tracks defined by H1, H2 and Cherenkov coincidence. For the 1991 data, the second-level selection was simplified, and the only requirement was the existence of a pair of CCAL clusters with invariant mass greater than 2.5 GeV/c^2. The third-level DST selection required that the high mass clusters be associated with charged tracks compatible with electrons: each cluster had to be associated with an H2 hit and a Cherenkov signal, if it was in the region where the Cherenkov was fully efficient (θ_{lab} range of 15-33° and 39-60°).

The reduction factor between the first and the third DST level was approximately 10^3. For example, in the 1991 run there were 12,466,946 *charged* trigger events collected at the

χ_2 energy, and the final DST contained 13,970 events. The number of events on the third-level DST's was small enough to perform more time-consuming analysis, such as kinematic fitting.

4.2 Kinematic fitting and event selection

4.2.1 Kinematic Fitting

Kinematic fitting [87, 88] was used for three purposes. First, to provide a way of selecting χ events from the background, based on the fit probability. Second, to find the optimal 4-momentum values of the final state particles, using the measured values and the constraint equations. And third, to determine the 4-momentum of a photon in the cases when it was not measured.

In the reactions 4.1 there are five constraint equations: total energy, 3-momentum conservation and the J/ψ mass. The effective number of constraints is equal to the number of constraint equations minus the number of unknowns. In the case when all three final state particles are detected, there are no unknowns, and the effective number of constraints is equal to 5–0=5 (5C fit). If energy and direction (two angles) of a photon are not known, the effective number of constraints is 5–3=2 (2C fit).

The SQUAW program package [89] was used to perform the kinematic fitting. The electrons were chosen as the two highest energy clusters in the CCAL, since kinematics of the reactions 4.1 forbid a CCAL photon to have higher energy than electrons. For the purpose of event selection (described in section 4.2.2), a 2C fit was first performed on all events, disregarding the measured energy and direction of the photon. In the next step, a 5C fit was done in the cases when the photon was detected, in order to improve the accuracy of direction and energy determination.

Since kinematic fitting was later used to select events, and the event selection process should not bias the angular distribution, accurate knowledge of measurement resolution is very important. If, for example, the resolution errors were underestimated in some region of the acceptance, the fit probability in that region would be lower, and a cut on probability could introduce a bias in the angular distribution. Position resolution of the CCAL has been thoroughly studied and is presently better known than that of the tracking detectors, therefore I chose to use just the CCAL position measurement in the kinematic fit. (If a photon was going in the forward direction, the FCAL position measurement was used.) Such an approach was feasible because the position resolution of the CCAL was almost as good as that of the tracking system (see sections 3.3.3, 3.3.4).

The assumptions about detector resolution made in the kinematic fitting program were tested on a control sample of χ_2 events. The events were selected using the *electron quality index*, which was based on the Cherenkov, H2 and RPC signals and on transverse shower profile in the CCAL; it is described in more detail in Ref. [47]. (The event selection used later for the angular distribution analysis does not rely on the electron quality index, see section 4.2.2.) Fig. 4.1 shows the 5C fit probability for the χ_2 events. The 1991 and 1990 data are shown separately, because the effective energy resolution of the CCAL was different in the two years. Both probability distributions are essentially flat, which shows that the resolution assumed in the fitting program was correct. (The spike at zero is due in part to the background, and in part to bad measurements of electron or photon tracks, caused mainly by energy losses in the CCAL cracks.) The assumptions about detector resolution were additionally studied by looking at the stretch functions, or pulls, of the kinematic fit [88], which separate energy and position measurement information.

The distribution of 5C fit probability for background events (selected using the same algorithm on the 1991 η_c' search data) is shown in Fig. 4.2. It is strongly peaked at zero, indicating that a probability cut will remove most of background events.

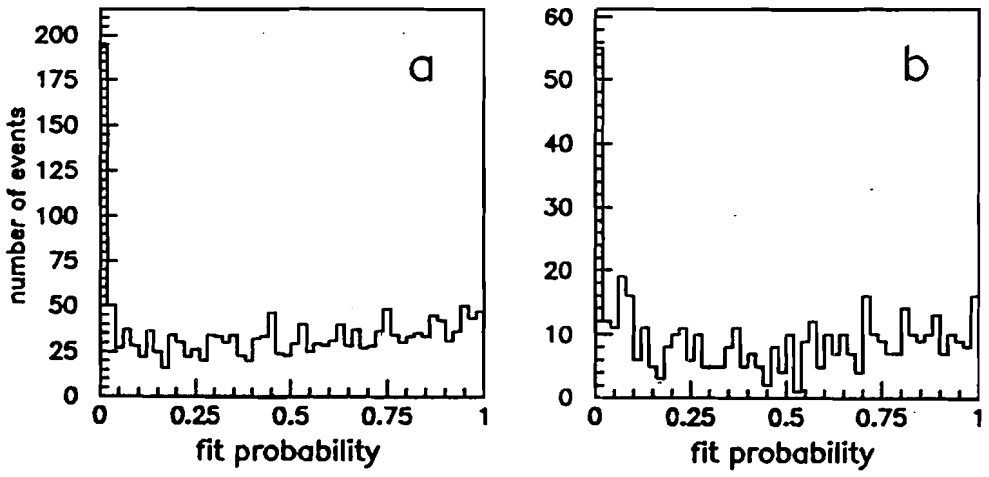

Figure 4.1: Probability of the 5C kinematic fit for (a) 1991 and (b) 1990 χ_2 data, selected using the electron quality index.

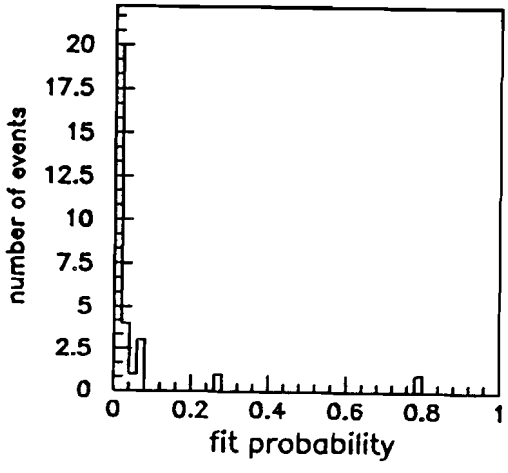

Figure 4.2: Probability of the 5C kinematic fit for background data (η_c' search), selected using the electron quality index.

4.2.2 Initial event selection

The goal of the event selection algorithm is to accept the maximum number of signal events while rejecting the maximum number of background events. In addition, the selection used for the angular distribution analysis should not bias the angular distribution of the data.

The event selection which was used by E-760 to measure masses and widths of the χ_1 and χ_2 states [47] was based on the electron quality index. Such a selection could introduce a bias in the angular distribution, because of non-uniform efficiency of the detectors, and residual angle-dependence of the signals.

In order to avoid this kind of bias, event selection used in this analysis was based only on the kinematic fit and on event topology. For electrons, only the information from the CCAL was used, where the efficiency is uniform and the resolution (in energy and position) is well known. The selection was designed to include events with the photon detected in the CCAL or in the FCAL, as well as those events in which the photon was not detected. In order to treat all events in the same way, independent of the θ_{lab} of the photon, in the selection process I have used the 2C kinematic fit, which relies only on the e^+ and e^- signals. Additionally, a very low threshold on the fit probability was used, avoiding systematic effects due to underestimated measurement errors. After the kinematic fit, a cut on the number of on-time CCAL clusters, depending on the predicted photon direction, was applied in order to further reduce the background. In addition, I have restricted the θ_{lab} range of the electrons to the region where the H1 hodoscope (which was a part of the trigger) was fully efficient.

The cuts applied to the data are summarized below:

1. $\theta_{lab}^{e^+}$ and $\theta_{lab}^{e^-}$ are between 15° and 60°;

2. invariant mass of the e^+e^- pair is between 2.8 and 3.4 GeV/c^2;

3. probability of the 2C fit is greater than 0.001; and

4. if photon is predicted to be within the CCAL acceptance ($7.6° < \theta^{\gamma}_{lab} < 76°$) [1] the number of on-time CCAL clusters must be ≤ 3; otherwise the number of on-time CCAL clusters must be 2.

Table 4.2 lists the number of events which survive the above cuts.

Table 4.2: Number of events surviving the initial event selection.

	χ_2 (1991)	χ_2 (1990)	χ_1 (1990)
3-rd level DST	13970	2806	2477
after selection	2638	580	483

To show qualitatively the effect of the selection on the data, in Fig. 4.3a I plot the e^+e^- invariant mass distribution, for all events from the third level χ_2 DST (unshaded histogram), and after the cuts described above (shaded histogram). Fig. 4.3 b shows analogous distributions for the background data (η_c' search), with the number of events normalized to the same integrated luminosity. The plots demonstrate that the selection leaves the major part of the signal, which appears as a peak around the J/ψ mass, while rejecting almost all background events. The contamination of the 1991 χ_2 sample with background events is approximately 2%.

A study of systematic effects (described in section 4.6) has shown that several additional cuts are needed in order to minimize systematic errors of angular distribution parameters. Some of these cuts also further reduce the background. The summary of the final event

[1] This range is bigger than actual CCAL acceptance, allowing a margin for the accuracy of predicted direction.

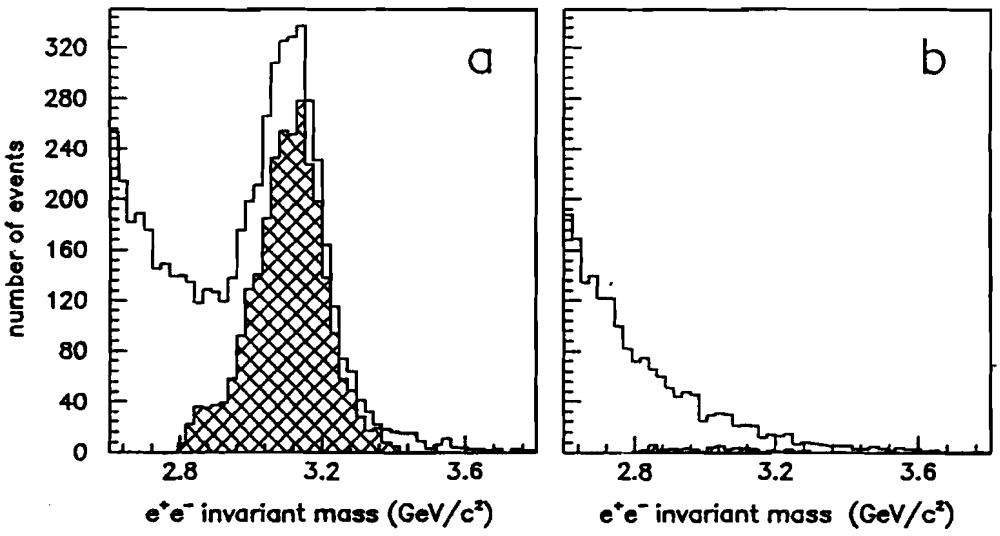

Figure 4.3: e^+e^- invariant mass spectrum for events from the third level DST (unshaded), and after the initial event selection (shaded); (a) χ_2 data (1991) and (b) background data (η_c' search) normalized to the same integrated luminosity.

sample and background estimate is given in section 4.7.

4.3 Determination of angles

For each selected event, angles θ, θ' and ϕ' (defined in section 2.1.1) were determined using fitted laboratory 4-momenta of the electrons and the photon. The following algorithm was used to calculate the angles:

1. boost all three particles to the rest frame of the χ_J, (the Lorentz factor $\gamma = \frac{m_\chi}{2m_p} =$ 1.8708 for χ_1 and 1.8951 for χ_2);

2. calculate the 4-momentum of the J/ψ in the χ_J frame as a sum of the two electrons, and determine θ;

3. calculate 4-momenta of the electrons in the rotated frame in which the Z' axis is opposite to the direction of the photon;

4. boost electrons along the Z' direction to the J/ψ rest frame ($\gamma = \frac{m_\chi^2+m_{J/\psi}^2}{2m_\chi m_{J/\psi}} = 1.0079$ for χ_1 and 1.0096 for χ_2); and

5. select randomly one of the electrons as e^+ and calculate its θ' and ϕ'.

The resolution in θ, θ' and ϕ' depends on energy and position resolution of the detector and on which kind of kinematic fit (5C or 2C) is used. A Monte Carlo simulation, taking into account CCAL and FCAL resolutions, was used to estimate the accuracy of determining the angles[2]. Fig. 4.4 shows the resolution in $\cos\theta$, $\cos\theta'$ and ϕ' of the 5C and 2C kinematic fits, and Table 4.3 shows the corresponding r.m.s. values.

Table 4.3: R.M.S. resolution in $\cos\theta$, $\cos\theta'$ and ϕ' for 5C and 2C kinematic fits (Monte Carlo).

	5C fit		2C fit	
	1991 run	1990 run	1991 run	1990 run
$\cos\theta$	0.009	0.009	0.052	0.073
$\cos\theta'$	0.010	0.012	0.079	0.100
ϕ' (radians)	0.033	0.038	0.106	0.129

As expected, the resolution of the 5C fit is better than that of the 2C. Therefore, to determine the angles, I have used 5C kinematic fit for all events for which the 5C fit probability was greater than 0.01. For the remaining events, when the photon was either not detected or badly measured (e.g. hitting close to a calorimeter edge), the results of the 2C fit were used.

[2]The simulation took into account different effective CCAL energy resolutions in the 1990 and 1991 runs.

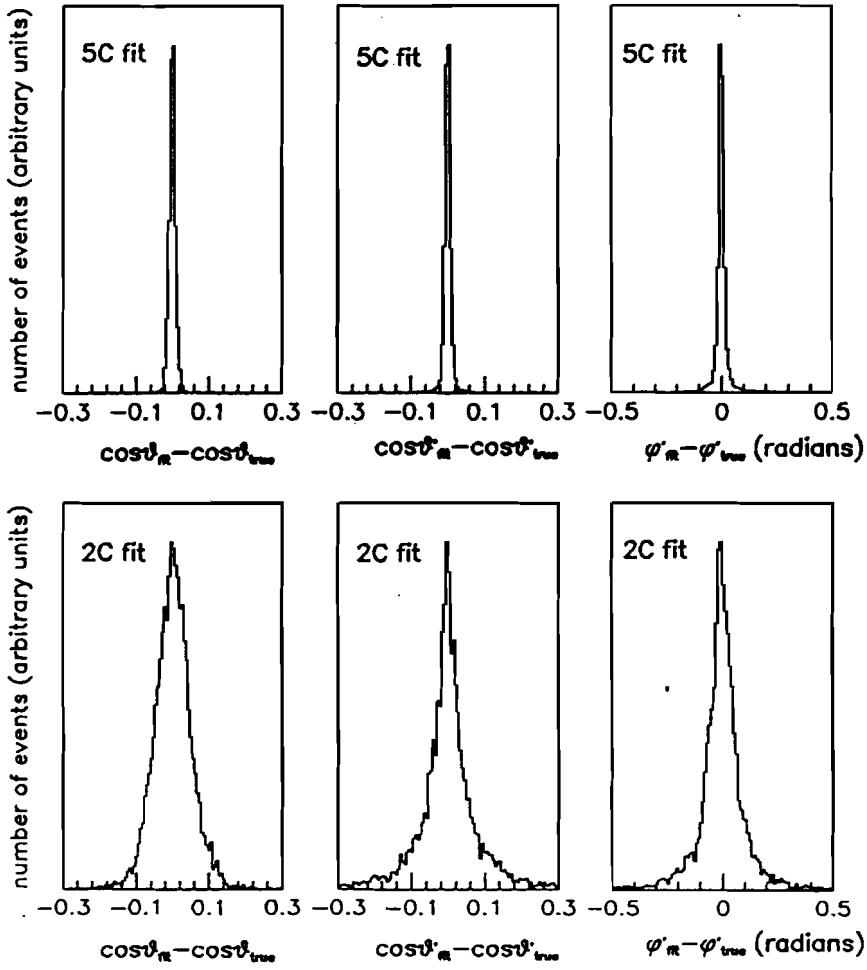

Figure 4.4: Resolution in $\cos\theta$, $\cos\theta'$ and ϕ' for 5C and 2C kinematic fit (Monte Carlo).

4.4 Raw and acceptance corrected distributions

Before proceeding with the full angular distribution analysis in three dimensions, it is useful to look at one-dimensional projections of the data, in order to make rough estimates of the values of the angular distribution parameters. The distributions of raw data in $\cos\theta$, $\cos\theta'$ and ϕ' are shown in Fig. 4.5 (χ_2 data, 1991 run) and Fig. 4.6 (χ_1 data). Since the electrons go back-to-back in the J/ψ rest frame, the angular distribution is invariant under the transformation $\cos\theta' \to -\cos\theta'$ and $\phi' \to \phi' + \pi$. Therefore, only a half of the $\cos\theta'$ and ϕ' range is shown. The uncorrected $\cos\theta$ plot does not have to be symmetric with respect to $\cos\theta \to -\cos\theta$, because the cuts in $\theta^{e^+}_{lab}$ and $\theta^{e^-}_{lab}$ (described in section 4.2.2) are not symmetric in the c.m. frame of the χ_J.

The raw data plots cannot be compared directly to the theoretical functions $W_J(\theta, \theta', \phi')$. They are distorted by detector acceptance and, to a smaller extent, by trigger and detector inefficiency. In this section I want to look at qualitative features of the data, thus I correct the data only for the geometric acceptance; other corrections will be discussed in section 4.6.

Geometric acceptance is defined by the cuts in $\theta^{e^+}_{lab}$ and $\theta^{e^-}_{lab}$. Fig. 4.7 shows the acceptance as a function of $\cos\theta$, $\cos\theta'$ and ϕ', for χ_2 (thin line) and χ_1 (thick line) events. The acceptance plots were generated using a Monte Carlo simulation, assuming the angular distribution corresponding to formation helicity ± 1 and a pure dipole radiative decay. In general, the shape of acceptance projections depends on the angular distribution, but the changes are small if the angular distribution parameters vary between the values assumed above and the values which were actually measured.

Fig. 4.8 shows the χ_2 distributions corrected for geometric acceptance. Comparing the plots with the theoretical shapes shown in Fig. 2.4, one can see that the slow rise of the $\cos\theta'$ distribution between 0 and 1 suggests that $a_2(\chi_2)$ is between -0.5 and 0. Also the $\cos\theta$ distribution, peaked at 0, hints at small and negative value of $a_2(\chi_2)$. The shape of

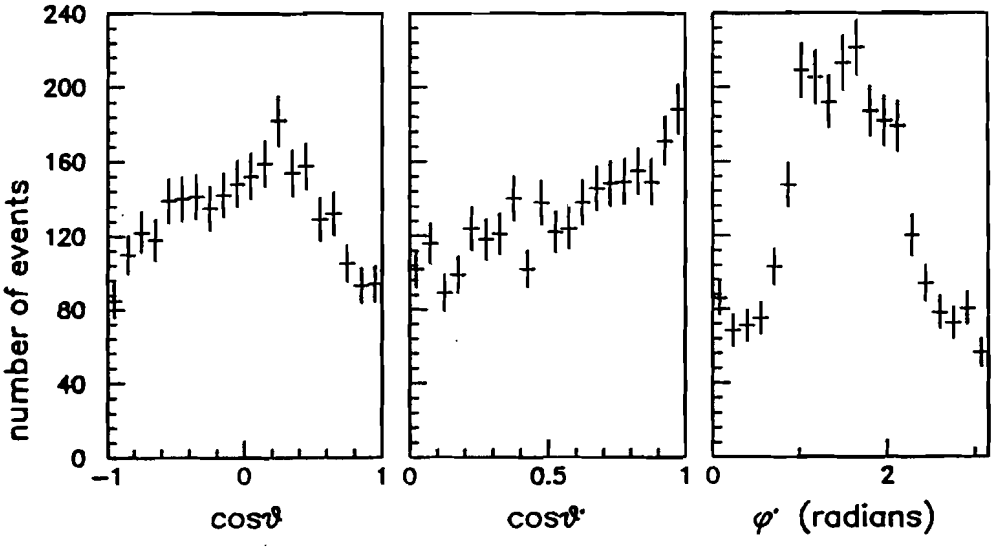

Figure 4.5: Raw data distributions in $\cos\theta$, $\cos\theta'$ and ϕ', χ_2 data (1991).

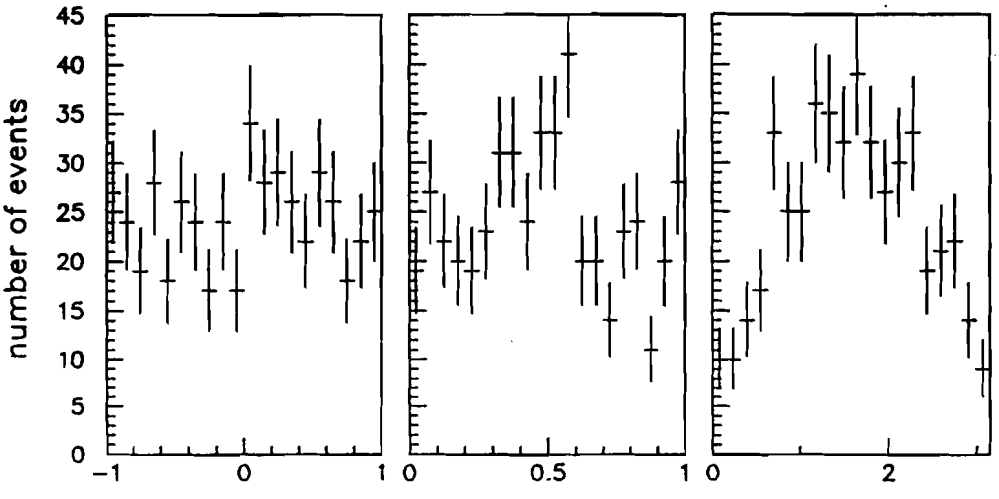

Figure 4.6: Raw data distributions in $\cos\theta$, $\cos\theta'$ and ϕ', χ_1 data.

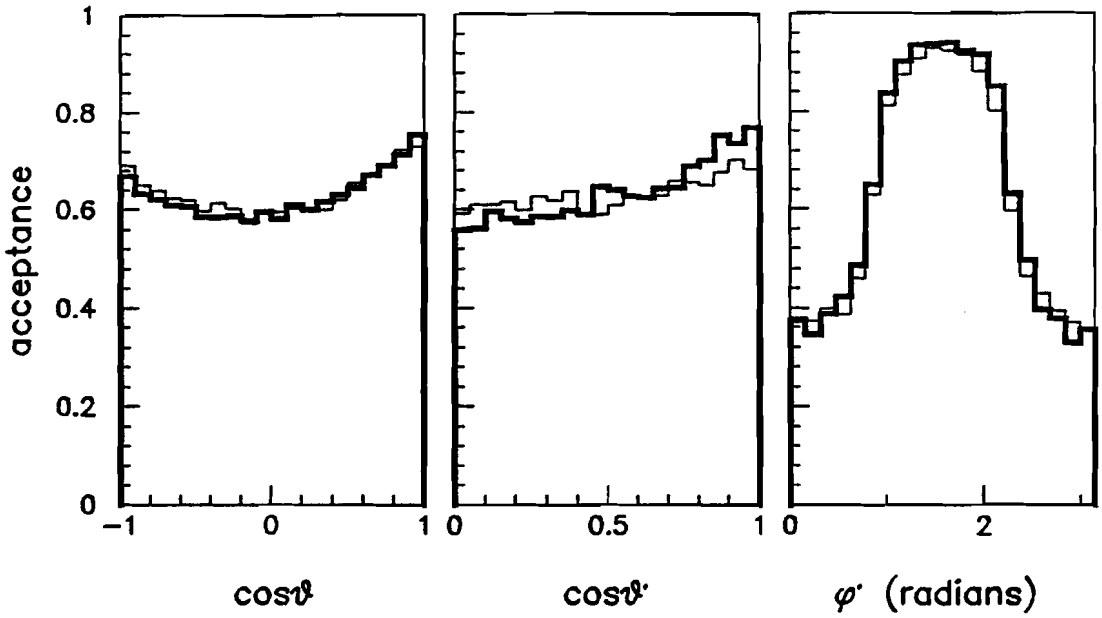

Figure 4.7: Geometric acceptance for χ_2 (thin line), and for χ_1 (thick line), assuming $B_0 = 0$ and $a_2 = a_3 = 0$.

the $\cos\theta$ distribution is not very sensitive to the value of $B_0^2(\chi_2)$, and it is hard to draw any conclusions about this parameter from the one-dimensional plots.

The acceptance-corrected distributions for χ_1 are shown in Fig. 4.9. Comparison of the distributions in $\cos\theta$ and $\cos\theta'$ with the theoretical curves (Fig. 2.3) suggests that $a_2(\chi_1)$ is a small negative number, between -0.3 and 0.

4.5 The maximum likelihood method

The maximum likelihood method [88] was used to find the most probable values of the angular distribution parameters. The likelihood function was defined as

$$\mathcal{L}(a_2, a_3, B_0) = \prod_{i=1}^{N_{events}} P_i(\theta, \theta', \phi'; a_2, a_3, B_0). \tag{4.2}$$

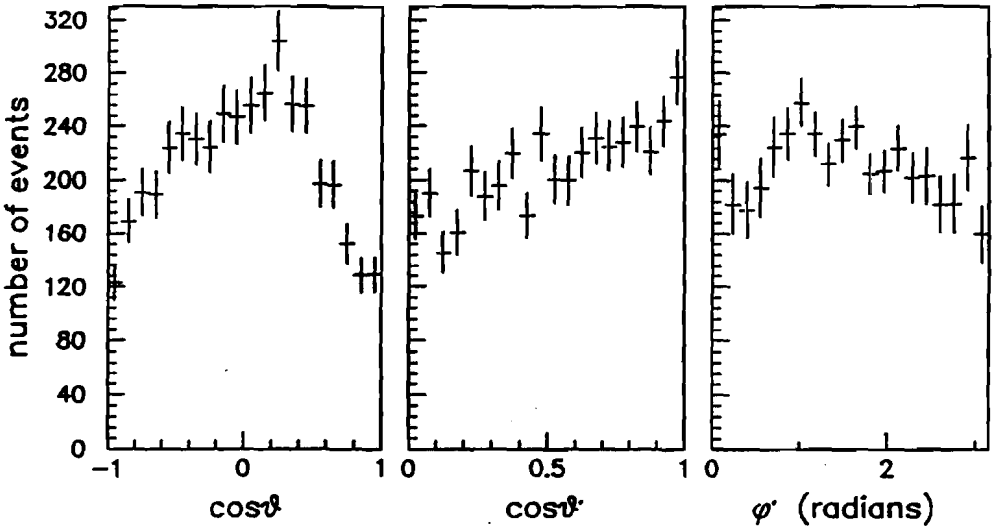

Figure 4.8: Acceptance corrected distributions in $\cos\theta$, $\cos\theta'$ and ϕ', χ_2 data (1991).

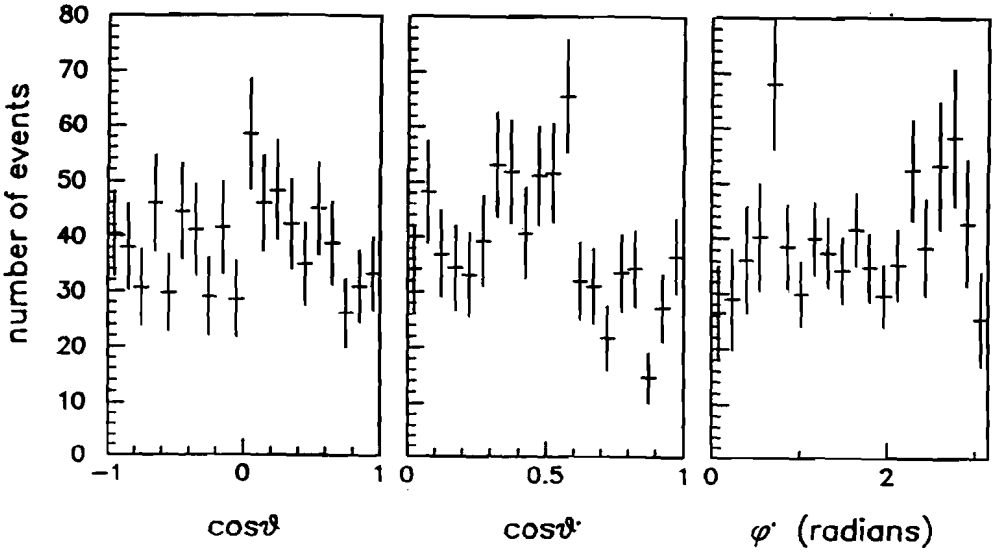

Figure 4.9: Acceptance corrected distributions in $\cos\theta$, $\cos\theta'$ and ϕ', χ_1 data.

The probability density P_i of getting an event with particular values of θ, θ' and ϕ' is given by

$$P_i(\theta,\theta',\phi';a_2,a_3,B_0) = \frac{W_J(\theta,\theta',\phi';a_2,a_3,B_0)\cdot\varepsilon(\theta,\theta',\phi')}{\int W_J(\theta,\theta',\phi';a_2,a_3,B_0)\cdot\varepsilon(\theta,\theta',\phi')\,d\Omega}. \tag{4.3}$$

Here W_J is the theoretical distribution function, $\varepsilon(\theta,\theta',\phi')$ is a product of efficiency and acceptance, and the integral is performed over the entire space.

The form of the likelihood function given by Equations 4.2 and 4.3 is rather inconvenient for fitting, because it involves a three-dimensional integral for each point in the a_2-a_3-B_0 space. This difficulty can be solved if we recall that the function W_J can be written as (Eqs. 2.11, 2.12)

$$W_J(\theta,\theta',\phi';a_2,a_3,B_0) = \sum_{j=1,N} f_j^J(\theta,\theta',\phi')\cdot K_j^J(a_2,a_3,B_0), \tag{4.4}$$

with N=5 for χ_1 and 11 for χ_2. The denominator in Eq. 4.3 becomes

$$\int W_J(\theta,\theta',\phi';a_2,a_3,B_0)\cdot\varepsilon(\theta,\theta',\phi')\,d\Omega = \sum_{j=1,N} F_j^J\cdot K_j^J(a_2,a_3,B_0), \tag{4.5}$$

where

$$F_j = \int f_j^J(\theta,\theta',\phi')\cdot\varepsilon(\theta,\theta',\phi')\,d\Omega. \tag{4.6}$$

The coefficients F_j^J are independent of the angular distribution parameters a_2, a_3, and B_0. The f_j's are known functions of θ, θ' and ϕ', so the coefficients F_j can be calculated numerically for any specific efficiency×acceptance configuration $\varepsilon(\theta,\theta',\phi')$.

In our case the efficiency is assumed to be uniform throughout the detector, and the acceptance is defined by the cuts on $\theta_{lab}^{e^+}$ and $\theta_{lab}^{e^-}$, and additional cuts which are introduced in section 4.6. The coefficients F_j were calculated by the Monte Carlo integration method, using 10^7 generated events.

In order to find the most probable values of the angular distribution parameters a_2, a_3, and B_0, the negative logarithm of the likelihood function was minimized using the CERN program package MINUIT [90]. In particular, the errors were calculated by the program MINOS, which takes into account non-linearities and parameter correlations.

The fitting procedure was tested on Monte Carlo simulated data. Events were generated according the the theoretical distribution function, assuming certain values of angular distribution parameters. They were then selected using the acceptance cuts, and the maximum likelihood fit was performed. The results of the fit agreed within the errors with the values assumed in the event generator.

Since the theoretical distribution function $W_J(\theta, \theta', \phi')$ is linear in B_0^2, the likelihood function $\mathcal{L}$ is approximately a gaussian function of B_0^2, and the statistical errors of B_0^2 are symmetric (which is not the case for B_0). For this reason, I will use B_0^2 rather than B_0 when presenting the results of the fit.

4.6 Study of systematic effects

A thorough study of possible biases of the data was performed, and several effects were found which could introduce systematic errors to the results. These effects are due to trigger inefficiency and detector resolution.

4.6.1 Trigger inefficiency

The *charged* trigger, which was used for the radiative decays of χ_1 and χ_2, was a logical OR of four subtriggers, described in detail in section 3.4. Table 4.4 shows the breakup of the $\chi_{1,2}$ events into the four subtriggers.

A significant fraction of events ($\sim$ 13%) did not pass the *2-Cherenkov* subtrigger, and

was accepted mostly by the *1-Cherenkov* subtrigger. The main reason was inefficiency of the Cherenkov counter in the partition region (see section 3.3.2). In 63% of the *1-Cherenkov* events one of the electron tracks had no Cherenkov signal and was in the θ_{lab} range of 32°-40° (close to the partition). In the remaining 37% of the *1-Cherenkov* events, both electron tracks had a Cherenkov signal, but the azimuthal correlation between Cherenkov and hodoscope modules, which was required by the trigger, was not satisfied. Occurrence of such events can be explained by the finite size of the interaction region.

The *1-Cherenkov* subtrigger was less efficient than the *2-Cherenkov*, because of the additional requirements on multiplicity of hits in the hodoscopes and on electron track azimuthal coplanarity. In the following sections the inefficiency due to these requirements is estimated and ways of correcting for it are described.

a) H1 and H2 multiplicity

The *1-Cherenkov* subtrigger required no more than 2 hits in each of the H1 and H2 hodoscopes. The efficiency of this requirement was studied using a sample of 1671 χ_2 events (from the 1991 run), which satisfied the *2-Cherenkov* subtrigger. (In this subtrigger, the requirement on the H1, H2 hit multiplicity was less restrictive: at most 4 hits were allowed).

Table 4.4: Number of events satisfying the four subtriggers of the charged trigger. (The *0-Cherenkov* subtrigger was not used during the 1990 run.)

	χ_2 (1991)	χ_2 (1990)	χ_1 (1990)
$2-Cherenkov$	2264	520	443
$1-Cherenkov$	335	60	40
$0-Cherenkov$	32	0	0
$no-CCAL$	7	0	0
total	2638	580	483

It was found that 499 events from this sample did not satisfy the H1, H2 multiplicity requirement, with the majority of these events having 3 hits in either H1 or H2. The extra hits in the hodoscopes can be attributed to three effects [91]: δ-rays[3] due to accidental interactions of the beam with the target, δ-rays caused by electrons interacting in the inner part of the detector, and photon conversions.

The relative inefficiency of the *1-Cherenkov* subtrigger caused by the hodoscope multiplicity requirement can be estimated as $\epsilon_{mult} = (1671-499)/1671 = 70 \pm 1\%$. If we consider only the events with one of the electrons in the Cherenkov partition region (which is the case for most *1-Cherenkov* events) the relative inefficiency is $\epsilon'_{mult} = 74 \pm 2\%$. An analogous study was done for the 1990 data, and the inefficiency was found to be $\epsilon_{mult} = 78 \pm 1\%$ and $\epsilon'_{mult} = 76 \pm 2\%$. The fact that the inefficiency was smaller in the 1990 run can be explained by lower (on average) beam currents, and consequently lower rate of δ-rays due to beam interactions.

In order to correct for this inefficiency the *1-Cherenkov* events were assigned a higher weighting factor w in the likelihood function, which was redefined as [88]

$$L = \mathcal{L}_{2e} \cdot \mathcal{L}_{1e}{}^{w}, \tag{4.7}$$

where $\mathcal{L}_{2e}$ and $\mathcal{L}_{1e}$ are products of event probability density (Eq.4.2) for *2-Cherenkov* and *1-Cherenkov* subtriggers, respectively. The few remaining *0-Cherenkov* and *no-CCAL* events were treated in the same way as the *1-Cherenkov* events. The weighting factor was chosen as $w = 1/\epsilon'_{mult} \cdot 63\% + 1/\epsilon_{mult} \cdot 37\%$, in order to account for the fact that 63% of the *1-Cherenkov* events have an electron track in the partition region. Substituting the values of ϵ'_{mult} and ϵ_{mult}, I obtain $w = 1.38$ for the 1991 run, and $w = 1.30$ for the 1990 run.

The procedure of treating events with weights described above underestimates statistical

[3] Energetic knock-on electrons.

errors, because the effective number of events in the likelihood function ($\sum_{i=1}^{N_{events}} w_i$) is bigger than the actual number of events. In our case, the effect was found to be very small, less than 3% of the size of the errors. Nevertheless, the errors were corrected in an approximate way [88], by multiplying the errors obtained from MINOS by the square root of the average event weight.

b) H2 coplanarity cut

The requirement of H2 coplanarity imposed on *1-Cherenkov* events introduced a significant bias to the angular distribution, since it is strongly correlated with the angles θ, θ' and ϕ'. (In the case of the decay $\chi_{1,2} \to J/\psi\gamma \to e^+e^-\gamma$, some of the momentum is carried away by the photon, and the e^+ and e^- are not completely coplanar.) Monte Carlo studies showed that the systematic shift of angular distribution parameters due to this cut can be as big as -0.04 (difference between measured and true value) for a_2, and -0.08 for B_0^2, in the case of χ_2. The sign of the shift can be understood qualitatively using Fig. 4.10, which shows the effect of the H2 coplanarity cut on the angular distribution. The cut depletes the regions of small $\cos\theta$ and $\cos\theta'$, which changes the shapes of the distributions in such way as if a_2 and B_0^2 were smaller (compare with Fig. 2.4).

Several ways of correcting for this effect were studied, and the following method was chosen as the most reliable: the H2 coplanarity cut was imposed on all events (including the *2-Cherenkov* subtriggers), and the cut was corrected for in the likelihood function by modifying the acceptance×efficiency function $\varepsilon(\theta, \theta', \phi')$.

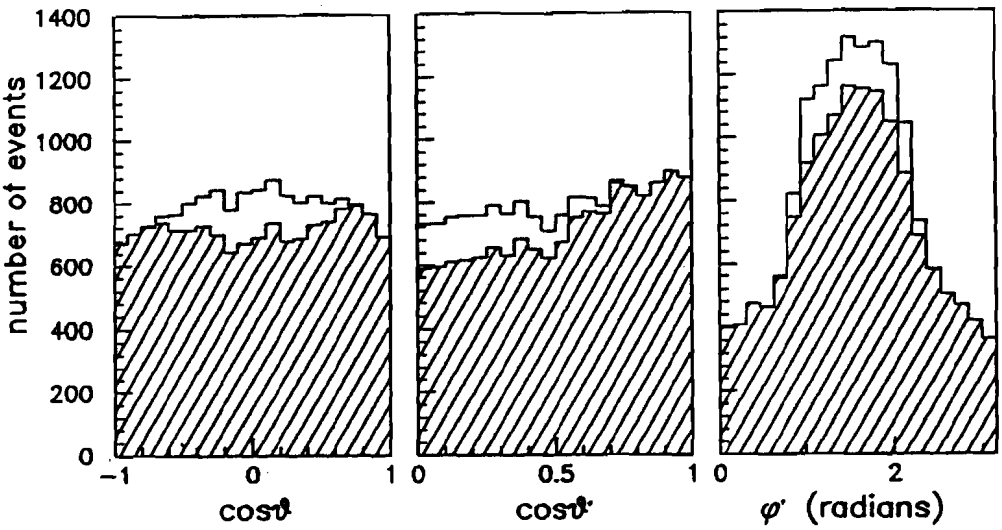

Figure 4.10: Effect of the H2 coplanarity cut on the angular distribution; unshaded histogram shows Monte Carlo generated χ_2 events after acceptance cuts, shaded histogram shows the events left after the H2 coplanarity cut.

4.6.2 Additional cuts

a) The cosθ' cut

Events with $|\cos\theta'| \approx 1$ correspond to a configuration where the photon is very close to one of the electrons. In such cases the CCAL clusters of the two particles overlap, and the event can not be properly reconstructed by the kinematic fit. (The CCAL clustering algorithm attempts to reconstruct partially overlapping clusters, but the task becomes impossible if the highest energy deposits are within the same CCAL block or in two adjacent blocks). This effect is demonstrated in Fig. 4.11, which shows a dip in the highest $\cos\theta'$ bin. In order to avoid a possible bias, events with $|\cos\theta'| > 0.95$ were rejected from the sample, and the efficiency×acceptance function $\epsilon(\theta, \theta', \phi')$ in the likelihood function was modified accordingly.

The second reason for the $\cos\theta'$ cut is the shape of the background, shown in Fig. 4.12 (data taken during the η_c' search, after the same event selection as for the $\chi_{1,2}$ data). The plot shows a strong peak at $\cos\theta'$ close to 1; the cut at $|cos\theta'| = 0.95$ reduces the background

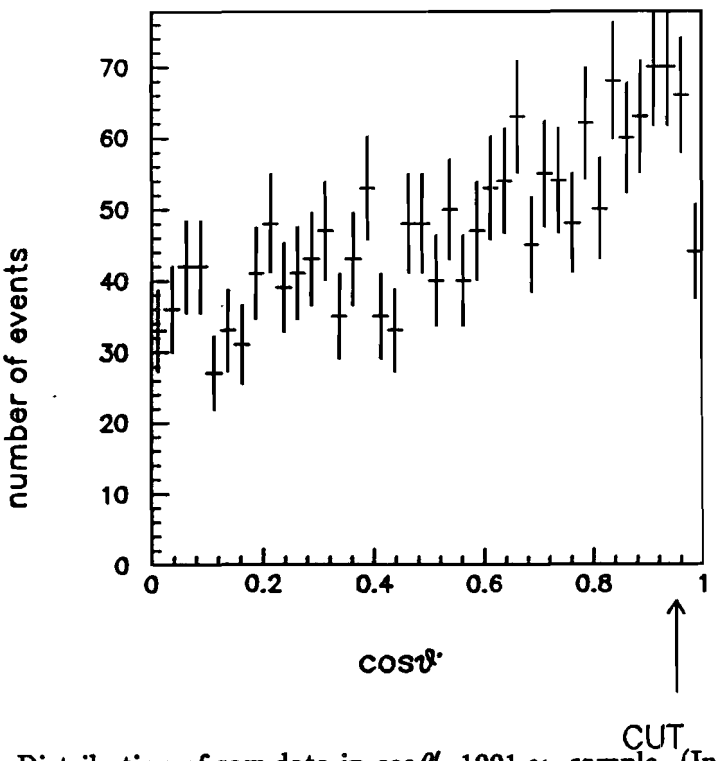

Figure 4.11: Distribution of raw data in $\cos\theta'$, 1991 χ_2 sample. (In addition to the initial event selection, the 5C fit probability was required to be > 0.1).

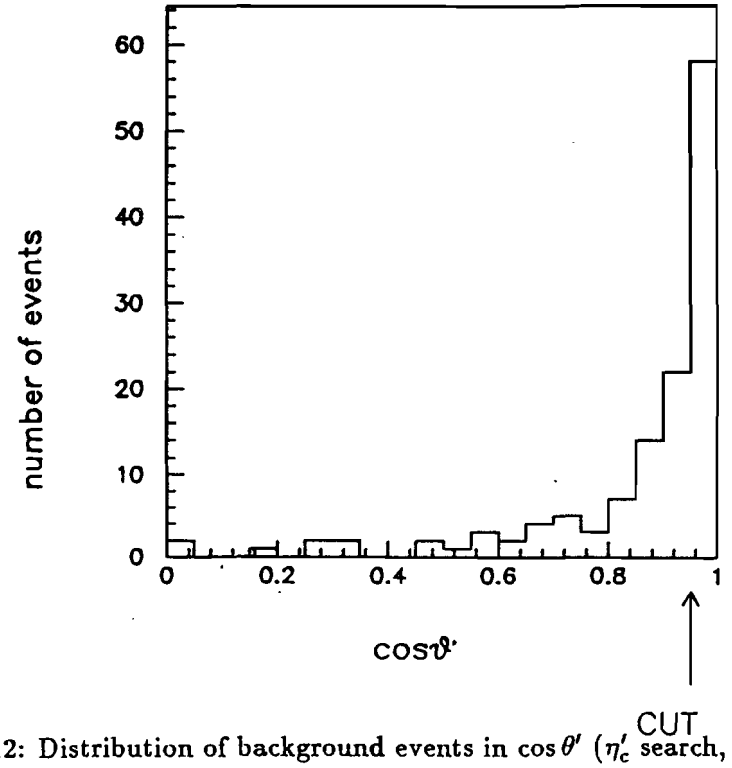

Figure 4.12: Distribution of background events in $\cos\theta'$ (η_c' search, initial event selection).

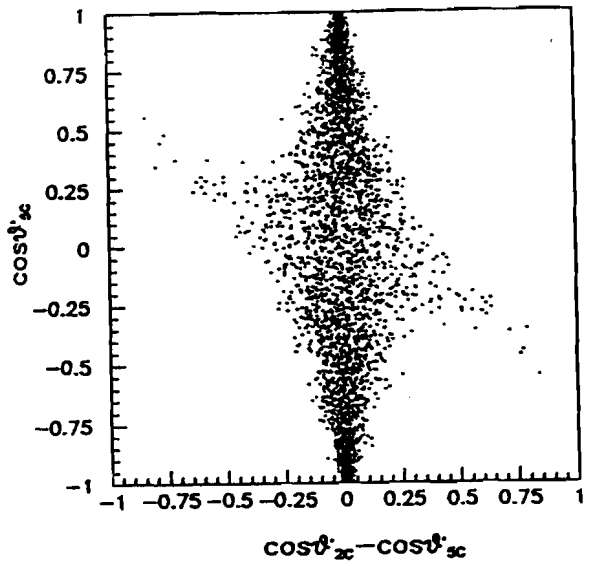

Figure 4.13: Difference between $\cos\theta'$ from the 2C and 5C kinematic fit as a function of $\cos\theta'_{5C}$, χ_2 data (1991).

by approximately a factor of two.

b) Resolution of the 2C kinematic fit

For approximately 20% of the events, the 2C kinematic fit must be used to determine the angles θ, θ' and ϕ', because the photon escaped from the back of the CCAL, or was badly measured, e.g. hitting close to a calorimeter edge. The resolution of the 2C fit is worse than that of the 5C fit by a factor of 3 to 8, as can be seen in Table 4.3. This should not bias the results provided that the resolution is constant as a function of θ, θ' and ϕ'. However, it was found that this is not true for θ'; the 2C fit resolution is much worse for small $|\cos\theta'|$ values (< 0.3) than for bigger ones. This is illustrated in Fig. 4.13, which shows the difference between $\cos\theta'$ determined by the 5C fit (which is very accurate) and by the 2C fit, as a function of $\cos\theta'_{5C}$. As a result of the non-uniform resolution, the region of small $|\cos\theta'|$ is depleted since more events are removed from it than added.

The bias of the angular distribution parameters due to this effect was studied using a Monte Carlo simulation, and was found to be between -0.01 and -0.04 for a_2, between

-0.02 and -0.05 for B_0^2, and negligible for a_3, in the χ_2 case. The size of the shift depends very strongly on detector resolution. In order to reduce this bias, an additional cut of $\theta_\gamma^{lab} < 65°$ was imposed on the data sample, which reduced the number of events for which the 2C fit must be used by approximately 60%. Even though the total number of events was reduced by $\sim 10\%$, the increase of the statistical error was smaller than the systematic error eliminated by this cut.

4.7 Final event selection and background estimate

Table 4.5 summarizes the cuts imposed on the data in order to minimize systematic errors. The last two lines show the number of events in the final event samples, and estimated number of background events.

The background was estimated in the following way. For the non-resonant background, I used the data collected during the searches for $^1P_1$ and η_c' (see Table 4.1), and imposed the same selection criteria as for the $\chi_{1,2}$ data. Table 4.6 shows number of background events surviving the selection, and the corresponding effective background cross-sections. Most of these events come from the reactions $p\bar{p} \to \pi^0\pi^0$, $\pi^0\pi^+\pi^-$ etc., with electrons coming

Table 4.5: Summary of additional cuts, final event sample, and background estimate.

	number of events		
	χ_2 (1991)	χ_2 (1990)	χ_1 (1990)
initial selection (sec. 4.2.2)	2638	580	483
after H2 coplanarity cut	2424	526	461
after $\lvert\cos\theta'\rvert < 0.95$ cut	2236	477	433
after $\theta_{lab}^{\gamma} < 65°$ cut	1904	405	360
final event selection	**1904**	**405**	**360**
background	28 ± 2	10 ± 3	9 ± 3

either from Dalitz decays, or from conversions of photons from π^0 decays. However, some of the events in the off-resonance samples are good χ_1 or χ_2 events, coming from the tails of Breit-Wigner distributions; thus the background cross-sections are overestimated. The contribution from the tails was determined to be $\sim 1.5\,\mathrm{pb}$ at the ${}^1P_1$ energy and $\sim 0.4\,\mathrm{pb}$ at the η_c'; the last line of Table 4.6 shows the effective background cross-sections after subtracting this contribution. For the final estimate of the background (shown in Table 4.5) I have used the weighted average of the 1991 η_c' and ${}^1P_1$ background cross-sections for the 1991 χ_2 data, and the 1990 ${}^1P_1$ background cross-section for the 1990 χ_1 and χ_2 data. The higher ratio of background to signal in the 1990 data is explained by the fact that the 1990 data were collected during energy scans, while the 1991 data were collected at the peak of the cross-section. The background level in all three data samples is very low, and its effect on the angular distribution should be negligible.

The procedure described above estimates the non-resonant part of the background. Since the event selection is mainly based on the e^+e^- pair characteristics, one should also consider a possibility of a resonant background coming from hadronic transitions $\chi_{1,2} \to J/\psi + X$, where $X = \pi^0$, $\pi^0\pi^0$, $\pi^+\pi^-$, $\pi^0\pi^0\pi^0$ or $\pi^+\pi^-\pi^0$. (The branching ratios for these decays are not known.) The transitions involving only neutral pions are forbidden by C-invariance. The decay to $J/\psi\ \pi^+\pi^-$ was studied by performing the kinematic fit, to the $J/\psi\ \pi^+\pi^-$ decay hypothesis, on all events from the third-level 1991 χ_2 DST which had at least four tracks; no events with fit probability greater than 0.01 were found. Taking into account geometric acceptance, and the requirement that at least one of the pions must be outside the CCAL in order to satisfy the number of CCAL clusters cut, I can set an upper limit of 3 events at the 95% confidence level; thus the contribution from this channel can be safely neglected. The decay into $J/\psi\,\pi^+\pi^-\pi^0$ has very small phase space, and with six particles in the final state its chances of surviving the cut on the number of clusters are extremely low; thus I assumed that this contribution is negligible. It should be noted, however,

Table 4.6: Estimate of non-resonant background.

	η_c' search (1991)	$^1P_1$ search (1991)	$^1P_1$ search (1990)
number of events (final selection)	57	205	13
effective cross-section	9.6 ± 1.3 pb	12.9 ± 0.9 pb	10.3 ± 2.9 pb
effective cross-section, corrected for χ tails	9.2 ± 1.3 pb	11.4 ± 0.9 pb	8.8 ± 2.9 pb

that in order to extract upper limits on the branching ratios BR($\chi_{1,2} \rightarrow J/\psi\, \pi^+\pi^-$) and BR($\chi_{1,2} \rightarrow J/\psi\, \pi^+\pi^-\pi^0$), a more careful analysis would be necessary.

Chapter 5

Results and discussion

In this chapter, results of the analysis of the angular distributions in the reactions $p\bar{p} \to \chi_{1,2} \to J/\psi\,\gamma \to e^+e^-\gamma$ are presented and discussed. Section 5.1 contains the results for the χ_2 and χ_1. Plots of the likelihood function are shown, and the angular distribution parameters which maximize the likelihood function are presented. To check consistency of the results, one-dimensional angular distributions are compared to the theoretical curves corresponding to the parameters found, and a global χ^2, which tests goodness of fit, is calculated. In section 5.2 the results of this analysis are compared with the results of previous experiments. Section 5.3 compares the results with theoretical predictions, which were discussed in detail in section 2.2.

5.1 Results

5.1.1 χ_2

The final results for the χ_2 were obtained by combining the two data samples from the 1991 and 1990 runs. However, the two data samples were first analyzed separately, in order to check their consistency.

a) The 1991 χ_2 data

Since both theoretical predictions (see section 2.2.2) and previous experimental results [7] suggest that the octupole amplitude is very small, the maximum likelihood fit was

Table 5.1: Results of the likelihood fits for χ_2.

		a_2	a_3	B_0^2
1991 data	fit 1	$-0.136\pm^{0.057}_{0.061}$	fixed at 0	$0.05\pm^{0.11}_{0.12}$
	fit 2	$-0.136\pm^{0.085}_{0.074}$	$0.000\pm^{0.060}_{0.047}$	$0.05\pm^{0.14}_{0.13}$
1990 data	fit 3	$-0.202\pm^{0.090}_{0.083}$	fixed at 0	0.00 ± 0.12
	fit 4	$-0.272\pm^{0.121}_{0.138}$	$-0.089\pm^{0.107}_{0.132}$	0.00 ± 0.09
1991 and 1990	fit 5	$-0.161\pm^{0.056}_{0.061}$	fixed at 0	$0.01\pm^{0.11}_{0.12}$
data combined	fit 6	$-0.173\pm^{0.067}_{0.040}$	$-0.017\pm^{0.042}_{0.040}$	0.00 ± 0.11

first performed assuming that $a_3 = 0$. The results of the fit are shown in Table 5.1 (fit 1). The values of a_2 and B_0^2 are those which maximize the likelihood function L (Eq. 4.7), and the statistical errors are determined by a distance from the maximum where the likelihood function decreases by a factor of $exp(-\frac{1}{2})$, which corresponds to one standard deviation. Fig. 5.1a shows the shape of the negative logarithm of the likelihood function, proving that the values of a_2 and B_0^2 quoted in Table 5.1 indeed correspond to the absolute minimum of $-lnL$. The detailed shape of the minimum is shown in Fig. 5.1b as a contour plot, with the contour lines corresponding to 1,2,3... standard deviations from the minimum.

As the next step, all three parameters, a_2, a_3, and B_0^2, were allowed to vary in the likelihood fit. The results are shown in Table 5.1 as fit 2. The octupole amplitude a_3 was found to be consistent with zero, and the values of a_2 and B_0^2 did not change compared to fit 1, which shows self-consistency of the results. The shape of the $-lnL$ function in the a_2-a_3 plane, with B_0^2 set to 0.05 (as obtained in fit 1), is shown in Fig. 5.2a. The secondary minimum of $-lnL$, at $a_2 \approx -0.9$, $a_3 \approx 0.4$, can be safely ignored, since the difference in lnL between the absolute minimum and the second one corresponds to 4.9 standard deviations. The shape of the absolute minimum is shown, as a contour plot, in Fig. 5.2b.

Fig. 5.3 shows a comparison of the data with the theoretical angular distribution function

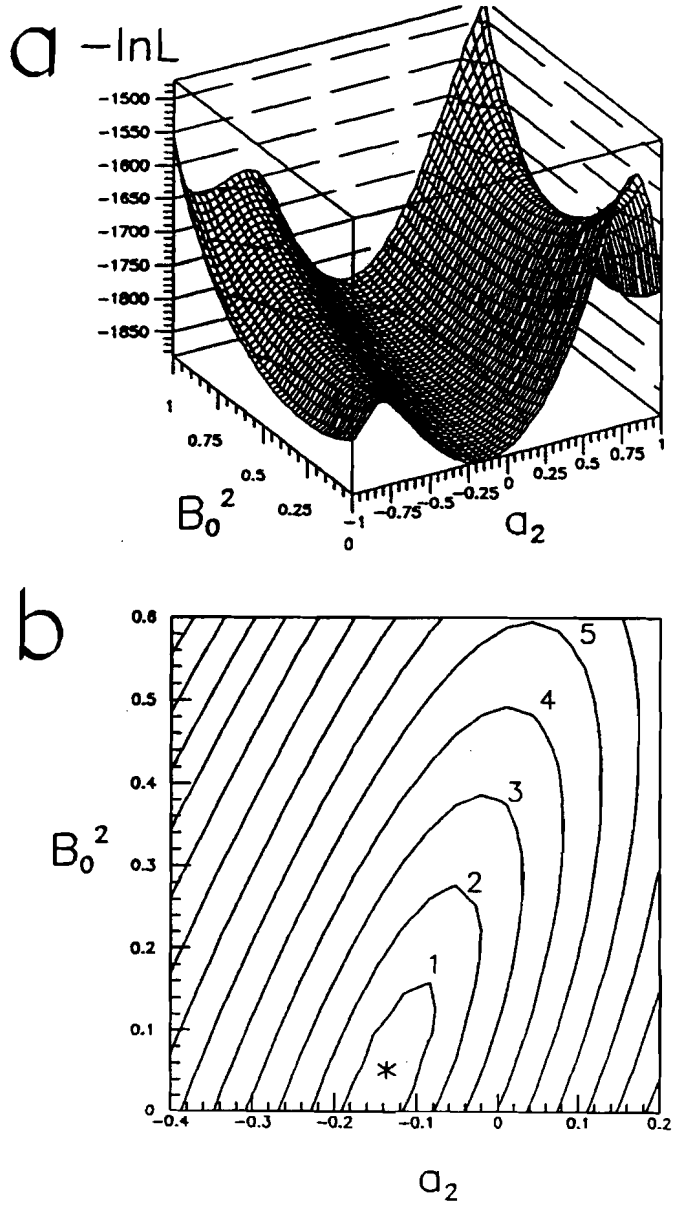

Figure 5.1: Negative logarithm of the likelihood function in the a_2-B_0^2 plane ($a_3 \equiv 0$), for the 1991 χ_2 data; (a) as a 3-dimensional plot, and (b) as a contour plot. In (b) the minimum is indicated by a cross, and contour lines correspond to 1,2,3... standard deviations.

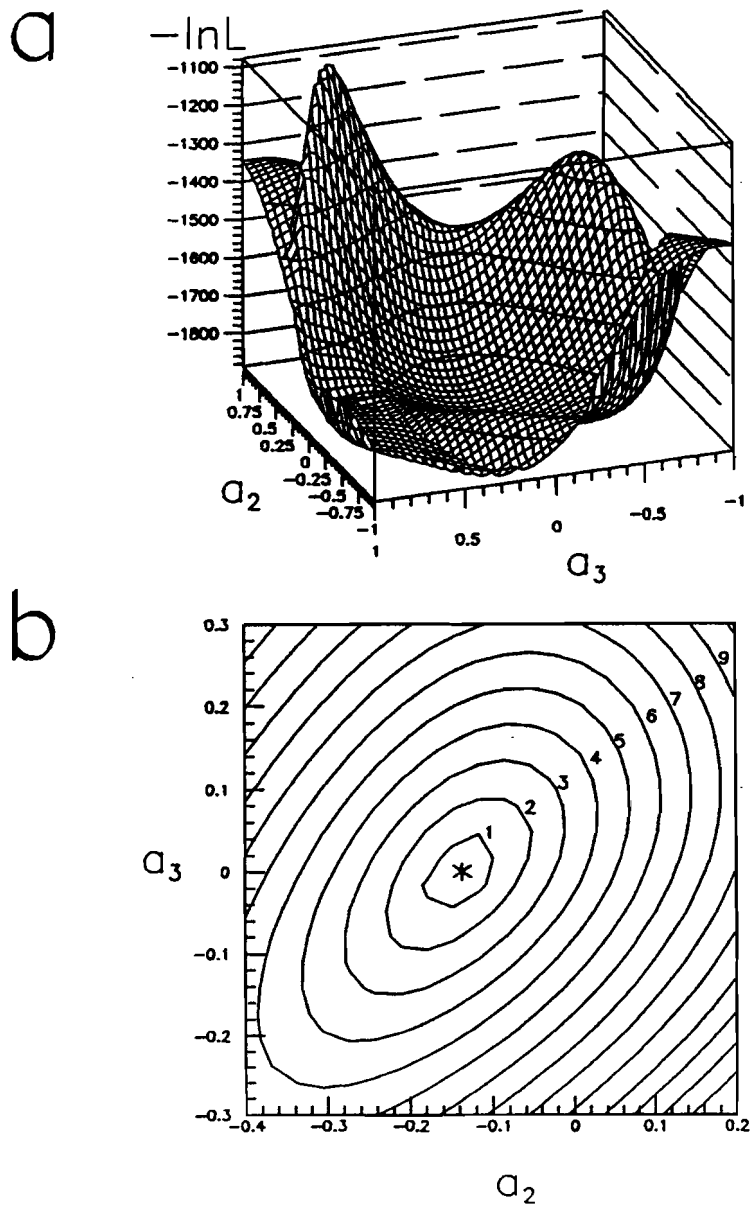

Figure 5.2: Negative logaritlım of the likelihood function in the a_2-a_3 plane ($B_0^2 \equiv 0.05$), for the 1991 χ_2 data; (a) as a 3-dimensional plot (the region where $a_2^2 + a_3^2 > 1$ is unphysical), and (b) as a contour plot. In (b) the minimum is indicated by a cross, and contour lines correspond to 1,2,3... standard deviations.

on 1-dimensional plots in $\cos\theta$, $\cos\theta'$ and ϕ'. Data points have been corrected for trigger efficiency and acceptance, so they can be compared directly with the theoretical distribution function. It should be mentioned that the data points are not exactly the same as those in Fig. 4.8, because of additional cuts and corrections described in section 4.6. The solid line is the function $W_2(\theta, \theta', \phi')$ (Eq. 2.12), with parameters a_2, a_3 and B_0^2 set to the values obtained from the 3-dimensional likelihood fit; the function is in good agreement with the data. For comparison, the dashed line in the $\cos\theta$ plot shows the theoretical function corresponding to a large positive value of a_2, which was obtained by the R704 experiment [7]. Our data are in clear disagreement with that result, which is discussed in section 5.2.2.

Since the value of the likelihood function does not provide a measure of the goodness of fit, I have estimated it using the χ^2 method. The data were binned into $5 \times 5 \times 5 = 125$ bins in $\cos\theta$, $\cos\theta'$ and ϕ', and the χ^2 was calculated as

$$\chi^2 = \sum_{i=1}^{125} \frac{(n_i^{obs} - n_i^{pred})^2}{(\sigma_i^{obs})^2}, \tag{5.1}$$

where n_i^{obs} is the observed number of events in the i-th bin and σ_i^{obs} is its error (both corrected for trigger inefficiency); n_i^{pred} is the number of events in the i-th bin predicted by a Monte Carlo, assuming the values of a_2, a_3 and B_0^2 obtained from the likelihood fit, and applying the same cuts which were applied to the data. The value of χ^2 was found to be 121.5, and with the number of degrees of freedom ($n.d.f.$) equal to 108 for fit 1 and 107 for fit 2, it corresponds to probabilities of 18% and 16%, respectively, which are quite acceptable.

b) The 1990 χ_2 data

Analogous fits for the 1990 χ_2 data were performed, and the results are shown in Table 5.1 as fits 3 and 4. The values of angular distribution parameters are consistent with

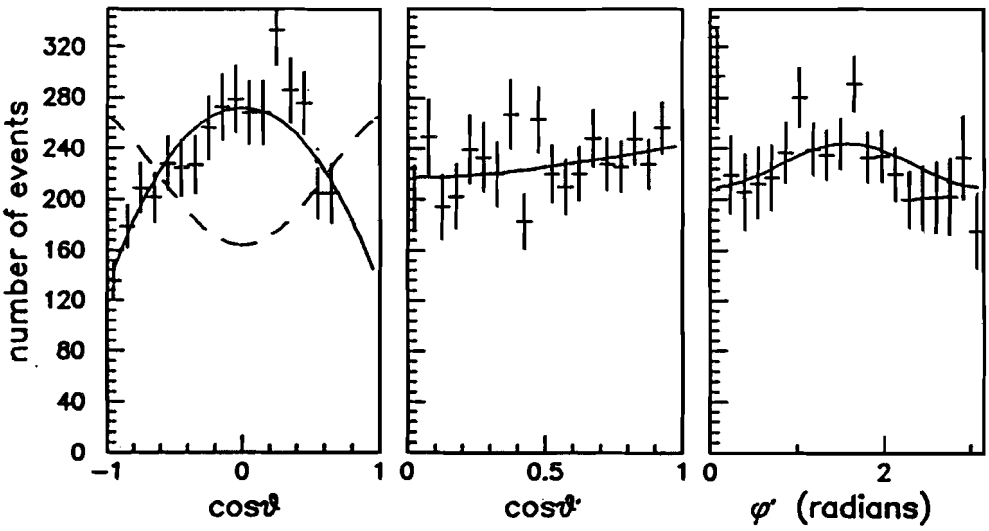

Figure 5.3: Comparison of the 1991 χ_2 data, corrected for acceptance and efficiency, with the function $W_2(\theta, \theta', \phi')$. The solid line shows the function corresponding to $a_2 = -0.136$, $a_3 = 0$ and $B_0^2 = 0.05$ (our result); dashed line shows the function corresponding to $a_2 = 0.46$, $a_3 = 0$ and $B_0^2 = 0.20$ (R704 result).

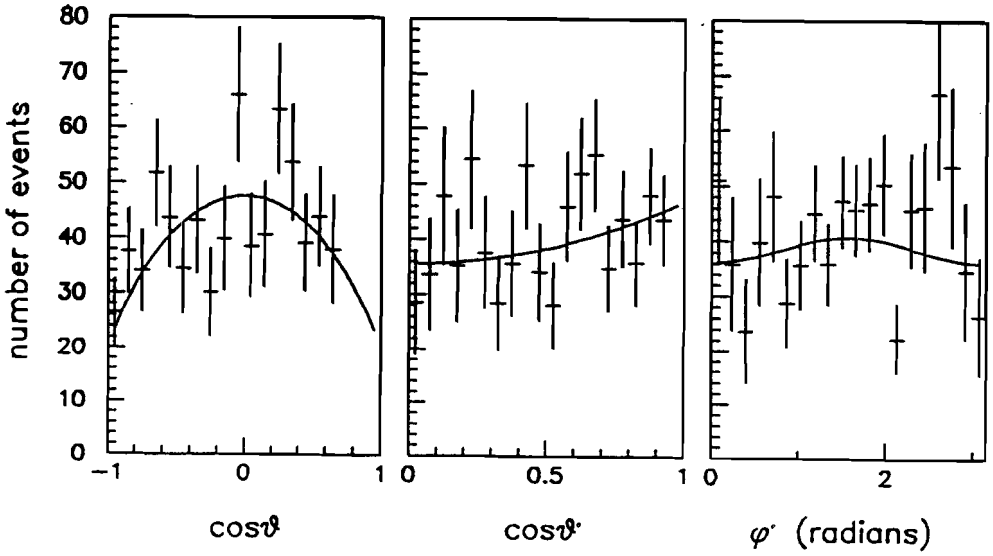

Figure 5.4: Comparison of the 1990 χ_2 data, corrected for acceptance and efficiency, with the theoretical angular distribution function. The solid line shows the function $W_2(\theta, \theta', \phi')$ corresponding to $a_2 = -0.202$, $a_3 = 0$ and $B_0^2 = 0.00$.

those obtained from the 1991 data sample. Fig. 5.4 shows the 1990 data, corrected for efficiency and acceptance, and the theoretical function $W_2(\theta, \theta', \phi')$ calculated with the parameters set to the values obtained from the 3-dimensional likelihood fit. The goodness-of-fit test was performed using the same binning as previously, and a definition of χ^2 which is appropriate for bins with few events [22]

$$\chi^2 = \sum_{i=1}^{125} [2(n_i^{pred} - n_i^{obs}) + 2n_i^{obs} \ln \frac{n_i^{obs}}{n_i^{pred}}]. \tag{5.2}$$

The values of $\chi^2/n.d.f.$ for fit 3 and fit 4 were 88.6/101 and 88.3/100 respectively, corresponding to large probabilities of 81% and 79%.

c) Final χ_2 results

Finally, the likelihood fits were performed on the combined sample of the 1990 and 1991 data. The results are shown in Table 5.1 as fit 5 and fit 6.

5.1.2 χ_1

In the case of χ_1, there is only one parameter to be determined, namely a_2. The result of the maximum likelihood fit is shown in Table 5.2 (fit 1). The negative logarithm of the likelihood function $-lnL$, as a function of a_2, is shown in Fig. 5.5, displaying a well

Table 5.2: Results of the likelihood fits for χ_1.

	a_2	B_0^2
fit 1	-0.129 ± 0.059	fixed at 0
fit 2	$-0.120 \pm {}^{0.077}_{0.066}$	$0.10 \pm {}^{0.18}_{0.19}$

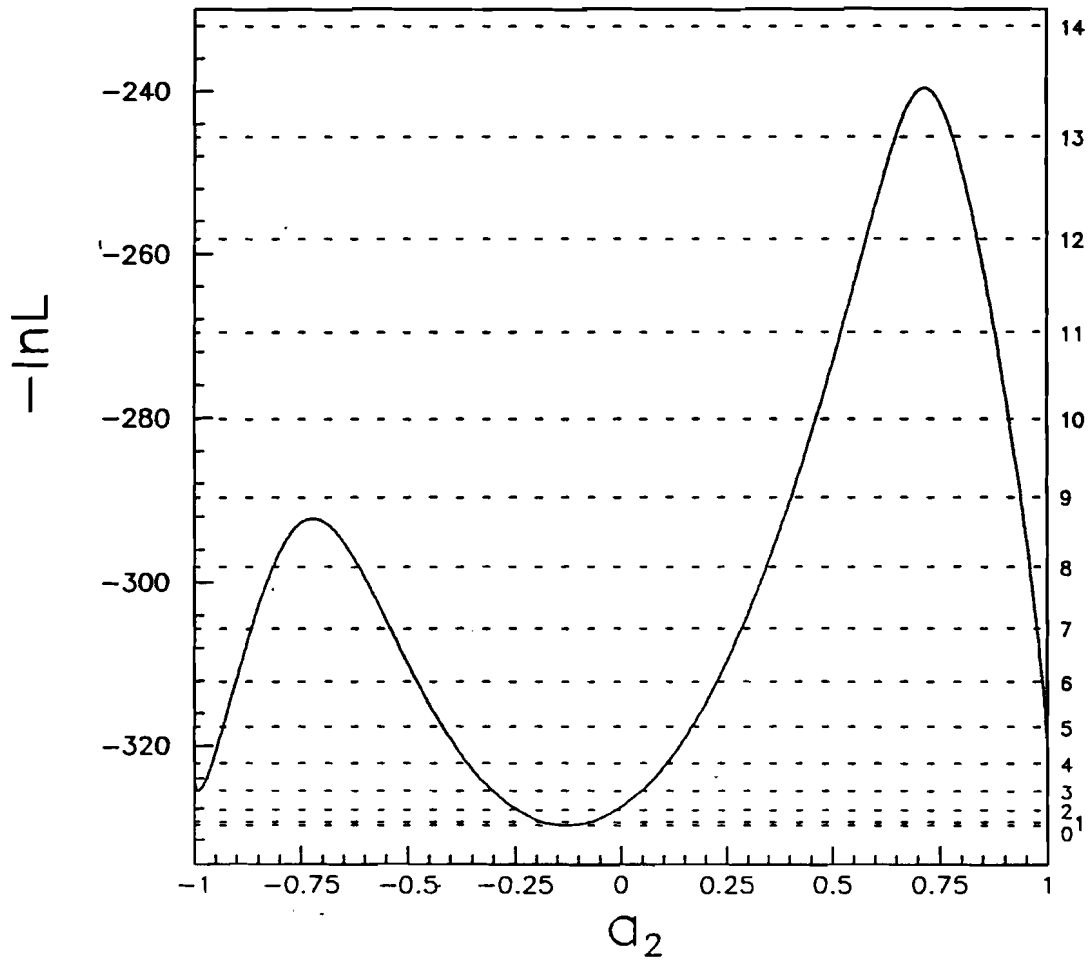

Figure 5.5: Negative logarithm of the likelihood function for the χ_1 data; dashed lines indicate levels of $-lnL$ corresponding to 0,1,2... standard deviations.

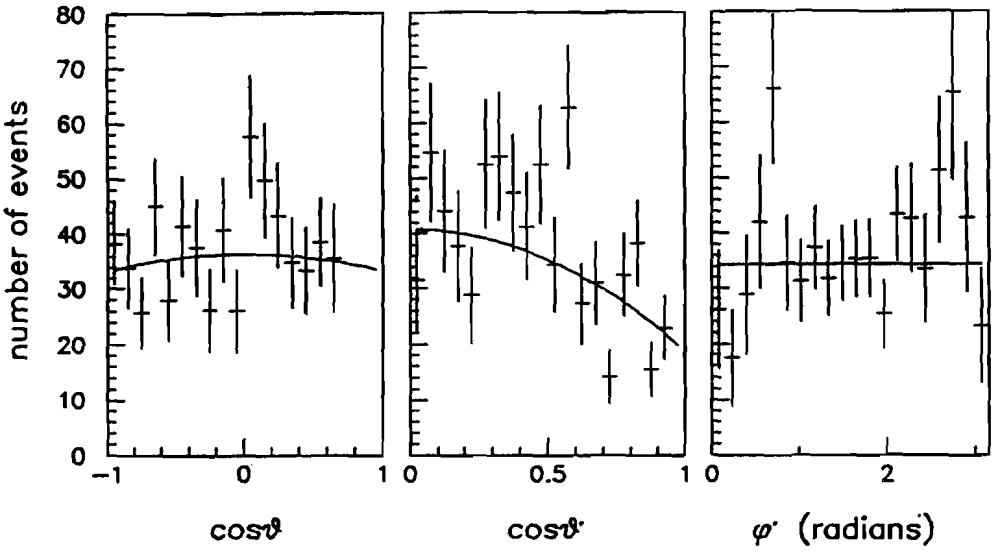

Figure 5.6: Comparison of the χ_1 data, corrected for acceptance and efficiency, with the theoretical angular distribution function. The solid line shows the function $W_1(\theta, \theta', \phi')$ corresponding to $a_2 = -0.129$.

defined minimum at $a_2 \approx -0.13$. The dashed lines indicate levels of $-lnL$ corresponding to 0,1,2,.. standard deviations from the value at the minimum. The two secondary minima at $a_2 = -1, +1$ can be neglected, since the difference in lnL between the absolute minimum and the secondary ones corresponds to 3.0 and 4.7 standard deviations, respectively.

Fig. 5.6 shows comparison of the χ_1 data, corrected for acceptance and efficiency, with the theoretical distribution function $W_1(\theta, \theta', \phi')$ (Eq. 2.11), calculated with a_2 set to -0.129 (as obtained from the likelihood fit).

The goodness-of-fit test was performed using the χ^2 defined by Eq. 5.2; the $\chi^2/n.d.f.$ was found to be 113.6/100, which corresponds to the probability of 17%.

Even though $B_0^2(\chi_1)$ must be equal to zero (see section 2.1.3), a second fit was performed, varying both a_2 and B_0^2, as a consistency check. The results are shown in Table 5.2 as fit 2. The obtained value of B_0^2 is consistent with zero, and the value of a_2 did not change significantly from that obtained in fit 1.

5.2 Comparison with previous experiments

Before E-760, the angular distributions for the reactions

$$p\bar{p} \rightarrow \chi_{1,2} \rightarrow J/\psi\,\gamma \rightarrow e^+e^-\gamma \tag{5.3}$$

were studied in only one experiment, namely R704 [7] at CERN. Due to limited statistics, R704 results suffer from large statistical uncertainty. Two other collaborations, SLAC-LBL [92] and Crystal Ball [6], studied angular distributions in the reactions

$$\begin{aligned} e^+e^- \rightarrow \psi' \rightarrow \chi_{1,2}\,\gamma \rightarrow J/\psi\,\gamma\gamma \;\; &\rightarrow \;\; e^+e^-\gamma\gamma, \\ \text{or} \;\; &\rightarrow \;\; \mu^+\mu^-\gamma\gamma, \end{aligned} \tag{5.4}$$

which enabled them to determine the multipole structure of radiative decay of the $\chi_{1,2}$ states (and also the multipole structure of the decay $\psi' \rightarrow \chi_{1,2}\,\gamma$). However, the primary goal of the angular distribution analysis done by these two experiments was to determine the spins of the χ states, which were not firmly established at the time.

Table 5.3 summarizes the three experiments (listed in chronological order). The results obtained by these experiments are compared with the results of this analysis in Table 5.4

Table 5.3: Previous experiments.

experiment	reference	reaction	events		measured parameters	
			χ_2	χ_1	χ_2	χ_1
SLAC-LBL	[92]	5.4	—	136	—	a_2
Crystal Ball	[6]	5.4	441	921	a_2 (a_3 assumed 0)	a_2
R704	[7]	5.3	54	30	B_0^2, a_2, a_3	a_2
E-760	this analysis	5.3	2309	360	B_0^2, a_2, a_3	a_2

Table 5.4: Comparison of results from previous experiments and from this analysis.

	χ_2			χ_1
	B_0^2	a_2	a_3	a_2
SLAC-LBL	—	—	—	0.09 ± 0.12
Crystal Ball	—	$-0.33 \pm {}^{0.12}_{0.29}$	—	$0.00 \pm {}^{0.01}_{0.02}$
R704	0.20 ± 0.29	$0.46 \pm {}^{0.19}_{0.18}$	0.09 ± 0.20	-0.13 ± 0.09
E-760	$0.01 \pm {}^{0.11}_{0.12}$	-0.16 ± 0.06	-0.02 ± 0.04	-0.13 ± 0.06

and in Fig. 5.7 (the figure also shows theoretical predictions, which will be discussed in section 5.3). Several comments on the comparison follow.

5.2.1 Helicity in $p\bar{p} \rightarrow \chi_2$

Our result for B_0^2 is consistent with the R704 result. The statistical uncertainty has been reduced by a factor of 2.6. In fact, the 3 standard deviations range of the R704 result covers the whole interval from 0 to 1, so our measurement is the first statistically significant evidence that the contribution of helicity zero is small.

5.2.2 Multipole structure of the decay $\chi_2 \rightarrow J/\psi\,\gamma$

The two previous measurements of the quadrupole amplitude $a_2(\chi_2)$, made by Crystal Ball and R704, were inconsistent with each other (a difference of 4.4 standard deviations). Additionally, comparison of the R704 result with theoretical predictions implied a large, negative anomalous magnetic moment of the charmed quark (see Eq. 2.24). Our measurement, which reduces the statistical uncertainty by a factor of 3-5, confirms the Crystal Ball result, and strongly disagrees with the R704 result (see Fig. 5.3).

The reason for the discrepancy between our result and that of R704 is not clear. The

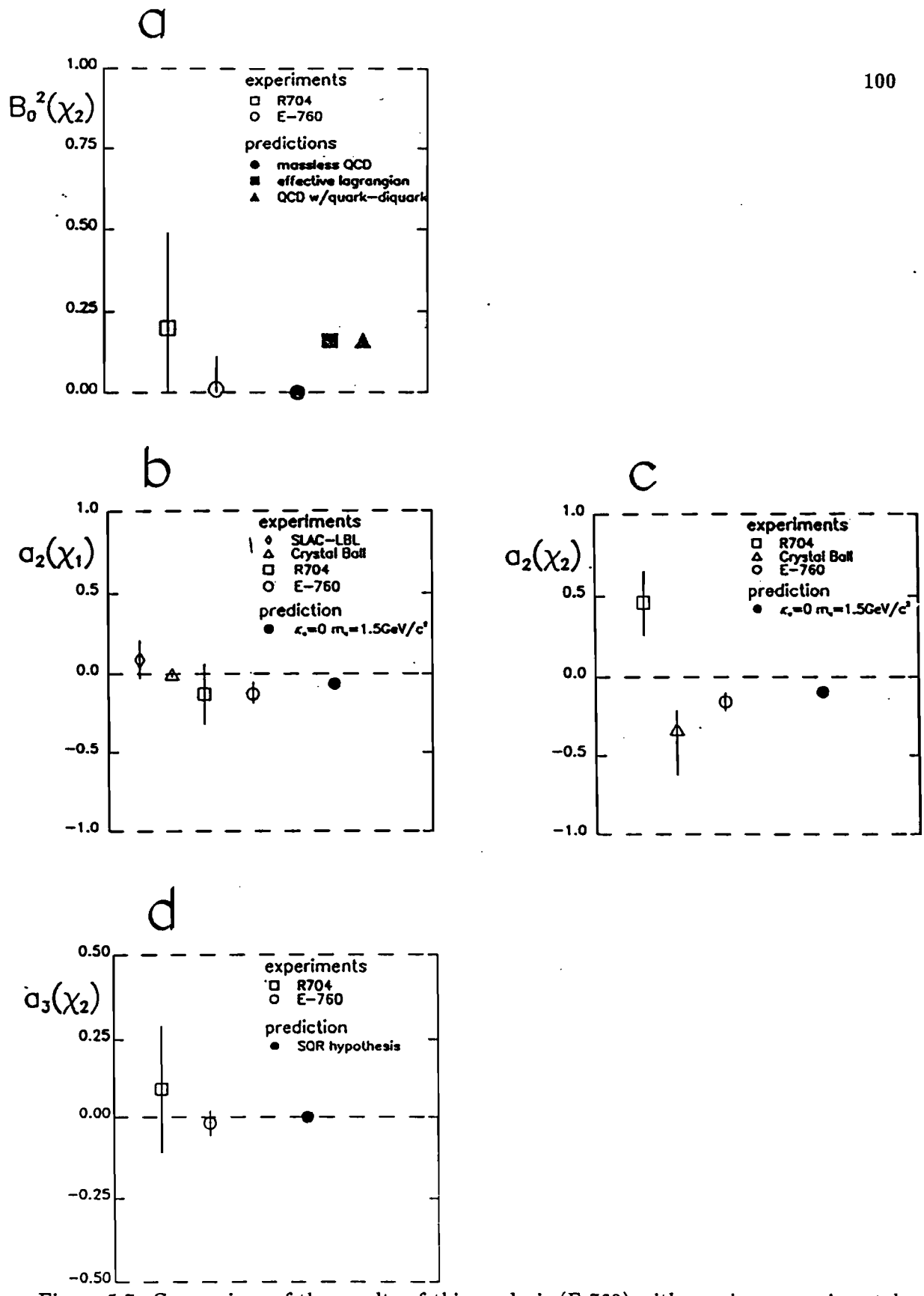

Figure 5.7: Comparison of the results of this analysis (E-760) with previous experimental results, and with theoretical predictions (references can be found in sections 5.2 and 5.3).

difference is probably not due to a statistical fluctuation (3.4 standard deviations). The angular distribution function used by R704 is consistent with their definition of θ, θ', and ϕ' [93]. One possible explanation is a bias in the R704 hardware or software event selection, which caused an excess of events with the photon going in the very forward direction (see Fig.1b of Ref. [7]).

Both R704 and this analysis find the octupole amplitude $a_3(\chi_2)$ consistent with zero; our measurement reduces the statistical uncertainty by a factor of 5.

5.2.3 Multipole structure of the decay $\chi_1 \to J/\psi\,\gamma$

All three previous measurements of the quadrupole amplitude $a_2(\chi_1)$ were consistent with zero within one standard deviation; our result is the first indication (at the 2 standard deviations level) that there is a non-zero quadrupole contribution. The most accurate measurement of $a_2(\chi_1)$ still belongs to the Crystal Ball experiment; our result is two standard deviations away from that result. As will be shown in section 5.3, comparison of the Crystal Ball result with theoretical predictions leads to some inconsistency; it would be interesting to repeat the measurement with better accuracy. In order to reach the Crystal Ball precision (0.02), we would have to increase our statistics by a factor of 8.5, which would require approximately $3300\,\mathrm{nb}^{-1}$ of integrated luminosity. The proposal for the next run [52] includes a possibility of such measurement.

Table 5.5: Comparison of theoretical predictions for B_0^2 with our result.

	B_0^2
massless QCD [4]	0
effective lagrangian [59]	0.157
QCD with quark-diquark [60]	0.16
experiment (this analysis)	$0.01 \pm^{0.11}_{0.12}$

5.3 Comparison with theoretical predictions

5.3.1 Helicity in $p\bar{p} \rightarrow \chi_2$

The three approaches of calculating the contribution of helicity zero in $p\bar{p} \rightarrow \chi_2$, which include the massless QCD helicity selection rule, effective lagrangian approach and QCD calculation using the quark-diquark model of the proton, were discussed in section 2.2.1. The predictions are summarized in Table 5.5; the same information is also shown in Fig. 5.7a. Our result is consistent with all three predictions. Even though it seems to favor the prediction of massless QCD, this is insignificant when statistical errors are taken into account. In order to be able to measure deviations of B_0^2 from zero, with statistical significance of 3 standard deviations, we would have to increase our statistics by approximately a factor of 4 (assuming that $B_0^2 = 0.16$).

5.3.2 Multipolarity in the radiative decays $\chi_{1,2} \rightarrow J/\psi\,\gamma$

The theoretical predictions for the relative contributions of quadrupole and octupole transitions [5], derived in the framework of the potential model of charmonium with relativistic corrections, were discussed in section 2.2.2.

The quadrupole amplitudes in χ_2 and χ_1 decays, given by Eqs. 2.24 and 2.27 respectively,

Table 5.6: Comparison of theoretical predictions for a_2 with our result; the uncertainty of the theoretical prediction is due to uncertainty of m_c.

	$a_2(\chi_2)$	$a_2(\chi_1)$
Ref. [5], $m_c = 1.5 \pm 0.3 \mathrm{GeV/c^2}$, $\kappa_c = 0$	-0.096 ± 0.019	-0.065 ± 0.013
experiment (this analysis)	$-0.161 \pm {}^{0.055}_{0.059}$	-0.129 ± 0.058

are sensitive to the mass m_c of the charmed quark and to its anomalous magnetic moment κ_c. The dependence of the quadrupole amplitudes $a_2(\chi_2)$ and $a_2(\chi_1)$ on κ_c, for several values of m_c, is shown in Fig. 5.8. Since the anomalous magnetic moment is expected to be small (see Section 2.2.2), we first compare our result with the predictions assuming $\kappa_c = 0$, and $m_c = 1.5 \pm 0.3\,\mathrm{GeV/c^2}$. The predictions and the experimental results are shown in Table 5.6 (see also Figs. 5.7b,c). Experimental results for both χ_2 and χ_1 are approximately one standard deviation below the predicted values; this is not a statistically significant difference, but it is interesting that the trend is the same for both states.

Alternatively, I can treat the results for the quadrupole amplitudes as measurements of the anomalous magnetic moment. The resulting values of κ_c, obtained using the Eqs. 2.24, 2.27, and $m_c = 1.5 \pm 0.3\,\mathrm{GeV/c^2}$, are shown in Table 5.7. (To get κ_c corresponding to a different value of m_c, it is enough to know that, for a given value of a_2, $(1+\kappa_c) \propto m_c$.) The results are not statistically inconsistent wi th zero, but a trend towards positive values shows for both χ_2 and χ_1.

The theoretical uncertainty, due to anomalous magnetic moment and mass of the charmed quark, cancels out (to the order E_γ/m_c) in the ratio

$$\frac{a_2(\chi_2)}{a_2(\chi_1)} = \frac{3}{\sqrt{5}} \frac{E_\gamma(\chi_2)}{E_\gamma(\chi_1)} = 1.48 \tag{5.5}$$

The experimental value of the ratio is 1.25 ± 0.72, in agreement with the prediction. It

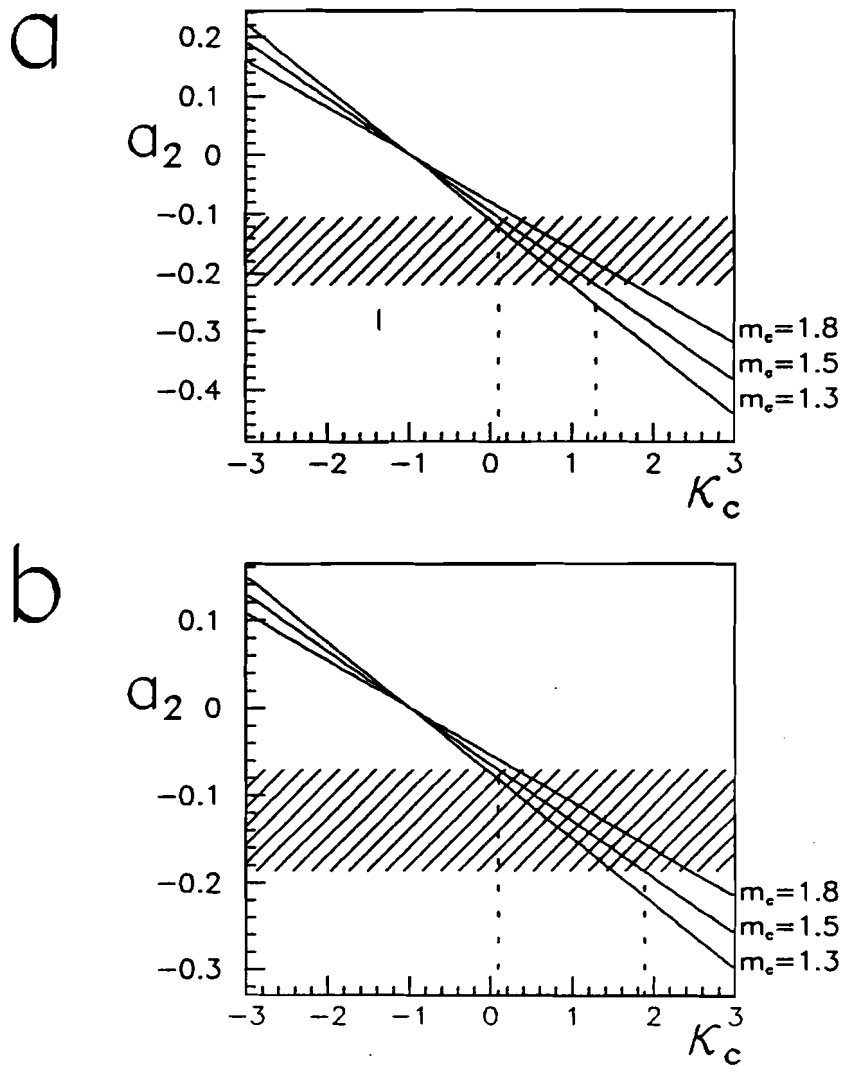

Figure 5.8: Quadrupole amplitudes (a) $a_2(\chi_2)$, and (b) $a_2(\chi_1)$, as functions of κ_c; shaded area shows the experimental results $\pm$ one standard deviation.

Table 5.7: Anomalous magnetic moment κ_c; the first error is statistical and the second is due to uncertainty of m_c.

	κ_c
from $a_2(\chi_2)$	$0.67 \pm {}^{0.57}_{0.61} \pm {}^{0.34}_{0.22}$
from $a_2(\chi_1)$	$0.99 \pm 0.89 \pm {}^{0.40}_{0.26}$
from $a_2(\chi_2)$ and $a_2(\chi_1)$ combined	$0.77 \pm 0.50 \pm {}^{0.35}_{0.24}$

should be noted that the ratio calculated using the Crystal Ball results (see Table 5.4), is inconsistent with the prediction, even though their statistical error on $a_2(\chi_1)$ is smaller than ours.

The octupole amplitude a_3 in the χ_2 decay is predicted to be zero (Eq. 2.25), which can be explained in terms of the single quark radiation hypothesis (see section 2.2.2). Our result $a_3 = -0.017 \pm {}^{0.041}_{0.038}$ is consistent with this prediction. The SQR argument is not valid if there is an admixture of D-wave in J/ψ, but even a sizable admixture b of D-wave results in a negligibly small value of the octupole amplitude: $a_3 \approx 0.022 \times b$. Thus, a measurement of the octupole amplitude is not useful for determining b.

Chapter 6

Conclusions

Experiment E-760 at Fermilab is the first high-statistics experiment which studied charmonium states formed in $p\bar{p}$ annihilation. In this process, it is possible to study charmonium states which are difficult or impossible to obtain in e^+e^- annihilation. During the 1990-1991 running period, we discovered the $^1P_1$ charmonium state, and made precision measurements of the parameters of the χ_1, χ_2, J/ψ, ψ' and η_c charmonium states [46–51].

This thesis describes the measurement of the angular distributions in the reactions $p\bar{p}\rightarrow\chi_{1,2}\rightarrow J/\psi\gamma\rightarrow e^+e^-\gamma$, using 2309 χ_2 events and 360 χ_1 events. From the analysis of the angular distributions it is found that the helicity in the χ_2 formation process is predominantly ±1; the contribution of helicity zero is $B_0^2(\chi_2) = 0.01\pm^{0.11}_{0.12}$. The radiative decays $\chi_{1,2}\rightarrow J/\psi\gamma$ are found to be mainly dipole transitions. The normalized quadrupole amplitudes for χ_2 and χ_1 are $a_2(\chi_2) = -0.161\pm^{0.056}_{0.061}$ and $a_2(\chi_1) = -0.129 \pm 0.059$, and the normalized octupole amplitude in the χ_2 decay is $a_3(\chi_2) = -0.017\pm^{0.042}_{0.040}$. These results represent a significant improvement on the experimental knowledge on the angular distribution parameters [6, 7].

Our measurement of $B_0^2(\chi_2)$ is the first statistically significant evidence that contribution of helicity zero in the formation process $p\bar{p}\rightarrow\chi_2$ is small. The result is consistent with predictions of both massless QCD [4], and those taking into account non-zero proton mass [59, 60]. In order to measure deviations of B_0^2 from zero at the level of three standard deviations, we would have to increase the statistics by a factor of four.

The results for the multipole amplitudes in radiative decays of the χ_1 and χ_2 states are consistent with the theoretical predictions [5], assuming charmed quark mass $m_c \simeq 1.5$ GeV/c^2.

and anomalous magnetic moment $\kappa_c \simeq 0$. Our result for $a_2(\chi_2)$ is in strong disagreement with the R704 measurement [7], which implied a large negative value of κ_c. The uncertainty in the theoretical predictions, due to mass and magnetic moment of the charmed quark, cancels out in the ratio of the quadrupole amplitudes for χ_1 and χ_2 decays. Our result for the ratio is in agreement with the prediction, while the results form the previous experiments [6, 7] do not agree with it.

There is a possibility of a more accurate measurement of the angular distribution parameters during the next run of this experiment (under the name of E-835), which is scheduled to begin in 1995 [52]. It is planned that in the next run the total integrated luminosity will be improved by a factor of 5 compared to the 1991 run, as a result of increased $\bar{p}$ stacking rate, beam intensity and density of the target. Even though in the proposal [52] the highest priority is assigned to the measurements of the $^1P_1$, η_c, η_c' and χ_0 states, there is also a possibility of collecting data at χ_1 and χ_2 energies, which can be used both for beam energy calibration and for measurement of the angular distributions.

Appendix

Kinematics

A.1 Kinematics of the $p\bar{p}$ annihilation

This section contains several useful formulae for kinematical variables in the $p\bar{p}$ annihilation. It is assumed the p target is at rest in the laboratory frame, and c is set to 1.

$$E_{cm}^2 = 2m_p(m_p + E_b), \tag{A.1}$$

$$E_b = \frac{E_{cm}^2}{2m_p} - m_p, \tag{A.2}$$

$$p_b = E_{cm}\sqrt{\left(\frac{E_{cm}}{2m_p}\right)^2 - 1}, \tag{A.3}$$

$$\gamma = \frac{E_{cm}}{2m_p}, \tag{A.4}$$

$$\beta \equiv \sqrt{1 - \frac{1}{\gamma^2}}, \tag{A.5}$$

where E_b, p_b are total beam energy and momentum in the laboratory frame, m_p is the mass of the proton, E_{cm} is the center of mass energy, and γ is the Lorentz factor of the center-of-mass frame.

Table A.1 lists the values of kinematical variables, such as beam energy and momentum, corresponding to the charmonium states.

Table A.1: Beam energy, momentum, γ and β corresponding to the charmonium states.

	E_{cm} $[MeV]$	E_b $[MeV]$	p_b $[MeV/c]$	γ	β
Accumulator design energy	4283	8838	8788	2.282	0.8989
$D\bar{D}^*$ threshold	3872	7051	6988	2.063	0.8747
ψ''	3770	6636	6569	2.009	0.8673
$D\bar{D}$ threshold	3729	6472	6403	1.987	0.8642
ψ'	3686	6302	6232	1.964	0.8607
η_c'	3594	5945	5871	1.915	0.8529
χ_2	3556	5800	5724	1.895	0.8494
$^1P_1$	3526	5687	5609	1.879	0.8466
χ_1	3511	5631	5552	1.871	0.8452
χ_0	3415	5276	5192	1.820	0.8355
J/ψ	3097	4173	4066	1.650	0.7955
η_c	2979	3791	3673	1.588	0.7767

A.2 Kinematics in the reactions $p\bar{p} \rightarrow \chi_{1,2} \rightarrow J/\psi\,\gamma \rightarrow e^+e^-\,\gamma$

This section includes some kinematical plots and formulae for the reactions $p\bar{p}\rightarrow\chi_{1,2}\rightarrow J/\psi\,\gamma\rightarrow e^+e^-\,\gamma$. Fig. A.1 shows the laboratory energy of the photon as a function of the laboratory polar angle θ_{lab}. Fig. A.2 shows analogous plot for the electrons; in this case the θ_{lab} is restricted to the range between 0.2 and 1.2 radians, which corresponds to the acceptance of the CCAL.

There is a simple relation between the angular distribution variable θ (defined in section 2.1.1), and θ_{lab} of the photon

$$\tan\theta = \frac{-\tan\theta_{lab}}{\gamma(1-\beta/\cos\theta_{lab})}. \qquad \text{(A.6)}$$

The dependence of $\cos\theta$ on θ_{lab}, following from this equation, is shown in Fig. A.3.

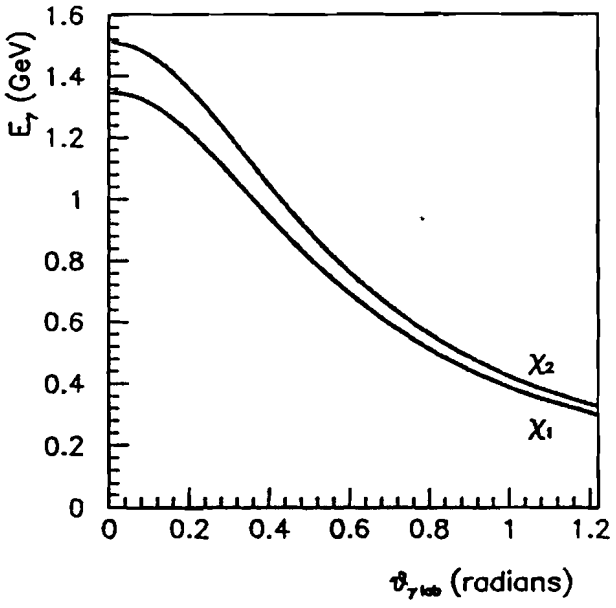

Figure A.1: Laboratory energy of the photon as a function of its polar angle, for χ_2 and χ_1.

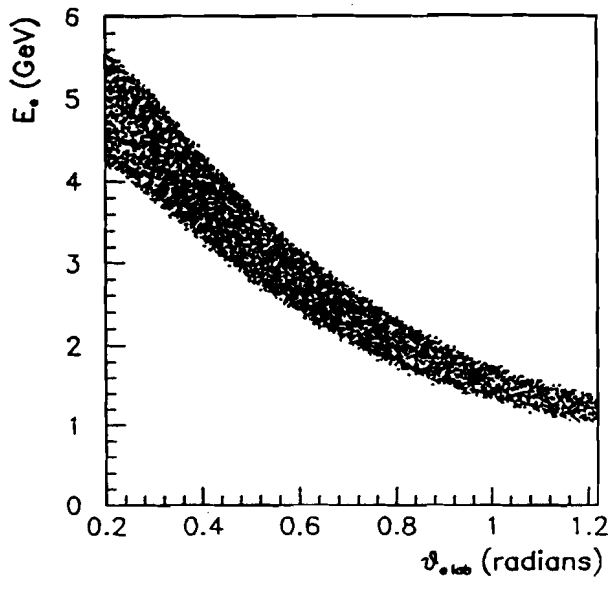

Figure A.2: Laboratory energy of electrons as a function of the polar angle; plots for χ_2 and χ_1 are the same.

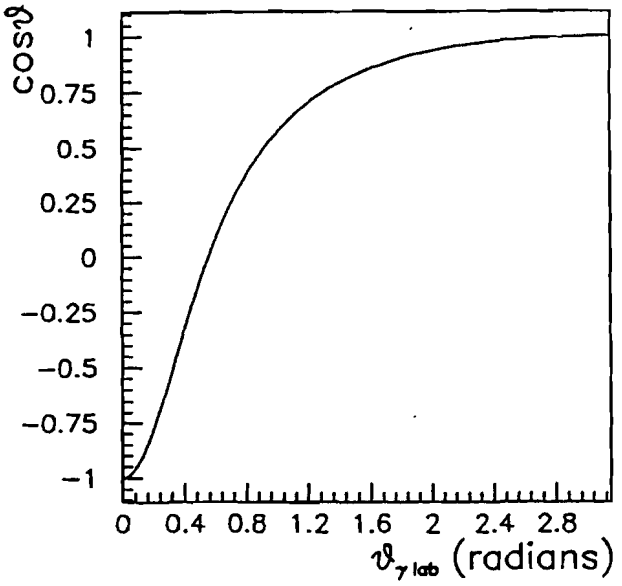

Figure A.3: $cos\theta$ as a function of θ_{lab} of the photon; plots for χ_2 and χ_1 are the same.

Bibliography

[1] W. Kwong, J. L. Rosner and C. Quigg, Ann. Rev. Nucl. Part. Sci. 37, 325 (1987).

[2] *Quarkonia*, edited by W. Buchmüller, North-Holland Publishing Co. (1992).

[3] F. L. Ridener, Jr., K. J. Sebastian and H. Grotch, Phys. Rev. D 45, 3173 (1992).

[4] A. Andrikopoulou, Z. Phys. C 22, 63 (1984).

[5] K. J. Sebastian, H. Grotch and F. L. Ridener, Jr., Phys. Rev. D 45, 3163 (1992).

[6] M. Oreglia *et al.*, Phys. Rev. D 25, 2259 (1982).

[7] C. Baglin *et al.*, Phys. Lett. B 195, 85 (1987).

[8] L. Bugge, University of Oslo Report No. 86-20 (1986), unpublished.

[9] V. A. Novikov *et al.*, Phys. Reports 41 C, 1 (1978).

[10] T. Appelquist, R. M. Barnett and K. Lane, Ann. Rev. Nucl. Part. Sci. 28, 387 (1978).

[11] J. Lee-Franzini, Nucl. Phys. B (Proc. Suppl.) 3, 139 (1988).

[12] L. Köpke and N. Wermes, Phys. Reports 174 C, 67 (1989).

[13] B. J. Bjorken and S. L. Glashow, Phys. Lett. 11, 255 (1964).

[14] S. L. Glashow, J. Iliopoulos, and L. Maiani, Phys. Rev. D 2, 1285 (1970).

[15] L. Litke *et al.*, Phys. Rev. Lett. 30, 1189 (1973).

[16] J. E. Augustin *et al.*, Phys. Rev. Lett. 33, 1406 (1974).

[17] J. J. Aubert *et al.*, Phys. Rev. Lett. 33, 1404 (1974).

[18] G. S. Abrams *et al.*, Phys. Rev. Lett. 33, 1453 (1974).

[19] T. Appelquist *et al.*, Phys. Rev. Lett. 34, 365 (1975).

[20] T. Appelquist and H. D. Politzer, Phys. Rev. D 12, 1404 (1975).

[21] E. Eichten *et al.*, Phys. Rev. Lett. 34, 369 (1975).

[22] Review of Particle Properties, Particle Data Group, Phys. Rev. D 45, (1992).

[23] S. Okubo, Phys. Lett 5, 165 (1963);
G. Zweig, CERN Reports No. TH-401 (1964) and TH-412 (1964);
J. Izuka et al., Prog. Theo. Phys. 35, 1061 (1966).

[24] G. J. Feldman *et al.*, Phys. Rev. Lett. 35, 821 (1975);
W. Braunschweig *et al.*, Phys. Lett. 57 B, 407 (1975).

[25] R. Partridge *et al.*, Phys. Rev. Lett. 45, 1150 (1980);
T. Himel *et al.*, Phys. Rev. Lett. 45, 1146 (1980).

[26] C. Edwards *et al.*, Phys. Rev. Lett. 48, 70 (1982).

[27] G. Goldhaber *et al.*, Phys. Rev. Lett. 37, 255 (1976).

[28] S. W. Herb *et al.*, Phys. Rev. Lett. 39, 252 (1977);
W. R. Innes *et al.*, Phys. Rev. Lett. 39, 1240 (1977).

[29] E. Eichten *et al.*, Phys. Rev. D 17, 3090 (1978).

[30] E. Eichten *et al.*, Phys. Rev. D 21, 203 (1980).

[31] C. Quigg and J. L. Rosner, Phys. Lett. B 71, 153 (1977).

[32] A. Martin, Phys. Lett. B 93, 338 (1980).

[33] J. L. Richardson, Phys. Lett. 82 B, 272 (1979).

[34] E. E. Salpeter and H. A. Bethe, Phys. Rev. 84, 1232 (1951).

[35] E. Altshuler and D. Silverman, UC Irvine Technical Report No. 92-35 (1992), submitted to Phys. Lett.

[36] C. N. Yang, Phys. Rev. 77, 242 (1950).

[37] R. McClary and N. Byers, Phys. Rev. D 28, 1692 (1983).

[38] H. Grotch, D. A. Owen and K. J. Sebastian, Phys. Rev. D 30, 1924 (1984).

[39] S. N. Gupta, W. W. Repko and C. J. Suchyta III, Phys. Rev. D 39, 974 (1989).

[40] X. Zhang *et al.*, Phys. Rev. D 44, 2293 (1990).

[41] A. A. Zholentz *et al.*, Phys. Lett. 96 B, 214 (1980).

[42] J. E. Gaiser *et al.*, Phys. Rev. D 34, 711 (1986).

[43] Review of Particle Properties, Particle Data Group, Phys. Lett. B 239, (1990).

[44] C. Baglin *et al.*, Nucl. Phys. B 286, 592 (1987).

[45] V. Bharadwaj *et al.*, Fermilab Proposal No. 760, (1985).

[46] T. A. Armstrong *et al.*, Phys. Rev. Lett. 69, 2337 (1992).

[47] T. Armstrong *et al.*, Nucl. Phys. B 373, 35 (1992).

[48] T. A. Armstrong *et al.*, Report No. FERMILAB-Pub-92/245-E 1992, submitted to Phys. Rev. D.

[49] T. A. Armstrong *et al.*, Phys. Rev. Lett. 68, 1468 (1992).

[50] T. A. Armstrong *et al.*, *Measurement of the $\gamma\gamma$ Partial Width of the χ_2 Resonance*, submitted to Phys. Rev. Lett.

[51] T. A. Armstrong *et al.*, *Two Photon Decays of the* $^1S_0$ *Charmonium Resonances Formed in* $p\bar{p}$ *Annihilations*, in preparation.

[52] T. A. Armstrong *et al.*, Fermilab Proposal No. 835, (1992).

[53] M. Jacob and G. C. Wick, Annals of Physics 7, 404 (1959);
A. D. Martin and T. D. Spearman, *Elementary Particle Theory*, North-Holland Publishing Co., Amsterdam (1970);
C. Bourrely, E. Leader and J. Soffer, Phys. Reports 59, 95 (1980);
J. D. Richman, California Institute of Technology Report No. CALT-68-1148 (1984).

[54] M. E. Rose *Elementary Theory of Angular Momentum*, John Wiley and Sons, Inc., New York (1957);
D. M. Brink and G. R. Satchler, *Angular Momentum*, Oxford University Press (1968).

[55] A. D. Martin, M. G. Olsson and W. J. Stirling, Phys. Lett. 147 B, 203 (1984).

[56] M. G. Olsson and C. J. Suchyta III, Phys. Rev. D 34, 2043 (1986).

[57] S. J. Brodsky, G. P. Lepage, Phys. Rev. D 24, 2848 (1981).

[58] F. Halzen, A. D. Martin, *Quarks and leptons*, John Wiley and Sons, Inc. (1984).

[59] W. Buchmüller, CERN Report No. CERN-TH.4142/85 (1985); in *Proceedings of the Third LEAR Workshop*, Tignes, France, edited by U. Gastaldi (1985) p 327.

[60] M. Anselmino, F. Caruso and R. Mussa, Phys. Rev. D 45, 4340 (1992).

[61] M. Anselmino *et al.*, Phys. Rev. D 38, 3516 (1988).

[62] M. Anselmino, F. Caruso and S. Forte, Phys. Rev. D 44, 1438 (1991).

[63] G. Karl, S. Meshkov and J. L. Rosner, Phys. Rev. Lett. 45, 215 (1980).

[64] M. A. Doncheski, H. Grotch and K. J. Sebastian, Phys. Rev. D 42, 2293 (1990).

[65] M. G. Olsson *et al.*, Phys. Rev. D 31, 1759 (1985).

[66] C. Quigg, in *Gauge Theories in High Energy Physics, Les Houches 1981*, edited by M. K. Gaillard and R. Stora, North-Holland (1983) p. 693.

[67] D. A. Geffen and W. Wilson, Phys. Rev. Lett. 44, 370 (1980);
A. N. Kamal, Phys. Rev. D 18, 3512 (1978).

[68] V. Zambetakis and N. Byers, Phys. Rev. D 28, 2908 (1983).

[69] Design Report: Tevatron I Project, Fermilab, Batavia, IL (unpublished), September 1984.

[70] J. Peoples, Jr., IEEE Trans. on Nucl. Sci. 30, 1970 (1983).

[71] J. Peoples, Jr., in *Proceedings of the Workshop on the Design of a Low Energy Antimatter Facility*, edited by D. Cline, (World Scientific Publishing Co, Singapore, 1989), p. 964.

[72] For a review, see D. Möhl *et al.*, Phys. Rep. 58, 73 (1980).

[73] M. Macri, in *Proceedings of Antiprotons for colliding beam facilities*, CERN, edited by P. Bryant and S. Newman (CERN 84-15, 1984), p 469.

[74] C. Biino *et al.*, Nucl. Instr. & Methods A 317, 135 (1992).

[75] C. Biino and S. Palestini, E-760 Internal Memo No. 289 (1992).

[76] C. Biino *et al.*, IEEE Trans. on Nucl. Sci. 36, 98 (1989);
C. Biino *et al.*, Nucl. Instr. & Methods A 271, 417 (1988).

[77] R. Calabrese *et al.*, Nucl. Instr. & Methods A 277, 116 (1989);
R. Calabrese *et al.*, IEEE Trans. on Nucl. Sci. 36, 54 (1989).

[78] G. Barisone *et al.*, Report No. Genova INFN/AE-89/6, 1989 (unpublished).

[79] L. Bartoszek *et al.*, Nucl. Instr. & Methods A 301, 47 (1991).

[80] R. Ray *et al.*, Nucl. Instr. & Methods A 307, 254 (1991).

[81] K. Gollwitzer, E-760 Internal Memo No. 262 (1991).

[82] M.A. Hasan *et al.*, Nucl. Instr. & Methods A 295, 73 (1990).

[83] W.R. Nelson *et al.*, Report No. SLAC-265 (1985), unpublished.

[84] M. Sarmiento *et al.*, *A Luminosity Monitor for FNAL experiment E-760*, to be submitted to Nucl. Instr. & Methods.

[85] S. Hansen *et al.*, IEEE Trans. on Nucl. Sci. 34, 1003 (1987).

[86] I. Gaines *et al.*, Computer Physics Communications 45, 323 (1987).
C. Gay *et al.*, IEEE Trans. on Nucl. Sci. 34, 870 (1987).

[87] E. Fett, *Kinematic Identification of Bubble Chamber Events*, University of Bergen, Norway (1965).

[88] A. G. Frodesen, O. Skjeggestad and H. Tøfte, *Probability and Statistics in Particle Physics*, Universitetsforlaget, Bergen-Olso-Tromsø (1979).

[89] O. I. Dahl, T. B. Day and F. T. Solmitz, *SQUAW: Kinematic Fitting Program*, University of California Lawrence Radiation Laboratory Report No. P-126 (1965), unpublished.

[90] F. James and M. Roos, *MINUIT: Function Minimization and Error Analysis*, Writeup D506, CERN Program Library (1981).
F. James, *Interpretation of the errors on parameters as given by MINUIT*, supplement to writeup D506, CERN Program Library.

[91] R. Mussa, E-760 Internal Memo No. 288 (1992).

[92] W. Tanenbaum *et al.*, Phys. Rev. D 17, 1731 (1978).

[93] B. Stugu, Ph.D. Thesis, University of Oslo (1987), unpublished.